(111)-ORIENTED GALLIUM ARSENIDE TENSILE-STRAINED QUANTUM DOTS TAILORED FOR ENTANGLED PHOTON EMISSION

by

Christopher Schuck

A dissertation

submitted in partial fulfillment

of the requirements for the degree of

Doctor of Philosophy in Materials Science and Engineering

Boise State University

May 2019

Christopher Schuck
SOME RIGHTS RESERVED

This work is licensed under a Creative Commons Attribution 4.0 International License.

BOISE STATE UNIVERSITY GRADUATE COLLEGE

DEFENSE COMMITTEE AND FINAL READING APPROVALS

of the dissertation submitted by

Christopher Schuck

Dissertation Title: (111)-Oriented Gallium Arsenide Tensile-Strained Quantum Dots Tailored for Entangled Photon Emission

Date of Final Oral Examination: 22 April 2019

The following individuals read and discussed the dissertation submitted by student Christopher Schuck, and they evaluated his presentation and response to questions during the final oral examination. They found that the student passed the final oral examination.

Paul J. Simmonds, Ph.D.	Chair, Supervisory Committee
Dave Estrada, Ph.D.	Member, Supervisory Committee
William B. Knowlton, Ph.D.	Member, Supervisory Committee
Olga Goulko, Ph.D.	Member, Supervisory Committee

The final reading approval of the dissertation was granted by Paul J. Simmonds, Ph.D., Chair of the Supervisory Committee. The dissertation was approved by the Graduate College.

DEDICATION

To my most loving and beautiful wife, Bethany, and my inspiring and darling daughters, Avalon and Everly.

ACKNOWLEDGEMENTS

Many mentors, colleagues, and friends supported the completion of this dissertation.

My primary advisor, Paul Simmonds has been a mentor, guide, inspiration, and friend throughout this process. He introduced me to the world of solid-state semiconductor research, and more specifically molecular beam epitaxy (MBE). We joined Boise State around the same time, and I got to be his first graduate student. During our first meeting he showed me a completely empty room; I was sold. Over the next two years – after many trips to hardware stores to rebuild broken components, refurbishing or replacing around half the MBE equipment, bloody knuckles from turning wrenches, flooding the lab a couple times, etc., etc. – we turned that room into a fully functioning MBE lab. Then, we began the research presented here. Paul's intelligence, experience, and kindness will forever be a pillar in my mind of what a good advisor should be.

In the course of building our MBE facility and the ensuing research I have also been blessed to work with many talented, intelligent, and fun students.

Kenton Burns and Joe Spinuzzi were the first two undergraduates in our lab. They helped build the infrastructure for Boise State's MBE research. Their capabilities to build entire auxiliary systems for future research was instrumental. Notably, I remember designing and assembling the cooling water distribution system with Kenton, and developing a Hall measurement system with Joe. I'll never forget installing the LN_2 system via standing on a wood crate with Kenton (if Boise State EHS somehow happens

to read this, please assume that was a metaphor for a safe installation method…). Thank you also, Joe, for your forever memorable musical entertainment and movie trivia.

The first graduate student to join our lab was Robin McCown. Her inquisitive nature and tireless effort were central to the development of the Boise State MBE laboratory. She helped design our MBE system layout and electronic rack arrangement, and partook in several adventures to acquire basic lab necessities such as desks, shelves, computers, and other electronic components. When we finally got our MBE operating, she helped with our first growth calibrations and has her name on some of the growth sheets of the first ever MBE samples grown at Boise State.

Simon Roy was the third undergraduate researcher to join our lab. His capabilities and insights were, to say the least, graduate student level from the beginning. He was a pillar of photoluminescence analysis and assisted with many projects to improve the MBE. In a given day, he could take a physics test, weld a metal rack to hold our turbomolecular pump, and write *LabVIEW* code for a characterization process. A true renaissance man, he also shared with us his abilities at glass blowing and river tour guiding.

Next came undergraduates Ashlie Hush and Austin Mellow who were instrumental in our first atomic force microscopy research, and both contributed to the happy environment of our research lab.

Ariel Weltner is another undergraduate that basically operated as a graduate student. She took over the Hall measurement system when Joe left, and cemented our material doping capabilities. In the process, she learned to grow samples on the MBE (a

rare capability among undergraduates). Also, her sense of humor and appreciation for good beer are greatly appreciated.

Trent Garrett was one of the most recent undergraduates to join our lab. He was highly inquisitive and very motivated from day one. His assistance with atomic force microscopy and data analysis were important contributions to my work. His tireless pursuit to understand the underlying physics of, well, everything, forced me to dig deeper than I would have on some research topics. Also, if you're ever bored, ask him to tell you a joke.

Carlos Cabrera was a visiting researcher whose computational abilities were indispensable. He developed the first computational models for the band gap and photon emission wavelengths of my TSQDs. His kind nature (and gift of a Cuban cigar) will always hold a place in my heart.

Kevin Vallejo and Katie Sautter were the next graduate students to join the lab. Kevin advanced our research into materials systems beyond QDs, including quantum dot molecules and surface acoustic wave structures. I will always hold dear the discussions with Kevin about the physics and philosophy of our research. Katie pioneered the adaptation of (111)A growth to Ge QDs. To my joy, they both successfully adopted the work-hard play-hard atmosphere of our lab. As I leave, they will take the reigns as the senior graduate students – it will be in good hands.

Among my collaborators, Baolai Liang and Kevin Grossklaus stand out. Baolai provided all the photoluminescence results presented in this dissertation, along with many insightful conversations about their meaning. Kevin diligently provided transmission

electron microscopy for my samples when other collaborators fell though; he also contributed intuitive analysis of his structural results.

ABSTRACT

The use of molecular beam epitaxy (MBE) to create quantum dots (QDs) embedded in solid-state semiconductor media has been at the forefront of novel and record-breaking optoelectronic device development for many years. However, the wide range of semiconductor fabrication capabilities and the non-equilibrium growth parameters inherent to MBE mean that there are still many QD research frontiers that are yet to be explored.

This work focuses on a recently discovered method that permits, for the first time, the growth of QDs under tensile strain on non-(100) surfaces. My research explores the first (and currently only) optically active materials system for tensile-strained QD (TSQD) growth on (111) surfaces: GaAs/InAlAs(111)A TSQDs. The use of MBE for the self-assembly of (111)-oriented GaAs TSQDs is of particular interest for quantum information science due to several properties inherently favorable for quantum light emission and quantum device integration.

In Chapter 1, I provide the background necessary to understand the self-assembly and properties of TSQDs. This background includes the basics of MBE operation and material growth, structural properties of III-V semiconductors (comparing the (100), Ga-terminated (111)A, and As-terminated (111)B planar surfaces), the nucleation and growth of the well-established gallium arsenide (GaAs) (100) III-V system and of indium arsenide QDs grown on that surface, the essential factors for entangled photon emission, and the research on TSQDs that preceded this work.

In Chapter 2, I follow this with a comprehensive analysis of the growth-parameter phase-space of GaAs(111)A TSQDs. Growth parameters include deposition amount, substrate temperature, growth rate, and V/III flux ratio. I discuss the boundaries of these parameters and the effects they have on QD height, diameter, volume, areal density, and photon emission wavelength and intensity. This study provides the first ever guide for customizing TSQD properties for future research and device applications. Using this guide, I outline the best route for optimization of GaAs(111)A TSQD entangled photon emission. In the course of this analysis I discuss several interesting and unique properties of TSQD nucleation and growth, including evidence for an equilibrium TSQD size and a TSQD nucleation rate sensitivity to arsenic concentration.

In Chapter 3, I present on an unusual and impactful discovery: a deviation from the conventional Stranski-Krastanov (SK) growth (in which a 2D wetting layer precedes QD formation and then remains fixed at given thickness). In contrast, I show that GaAs(111)A TSQD self-assembly occurs via an anomalous SK growth mode in which the WL continues to grow after QD formation. I use experimental and computational analyses of the GaAs(111)A WL and TSQDs to confirm this anomalous SK growth. No previous reports of this growth mode exist. This novel growth mode could prove to be valuable to future device designers, since research indicates that varying WL thickness can have significant impact on QD optical properties. This provides a unique and useful addition to growth-parameter tuning of TSQD properties.

In Chapter 4, I explore the use of dimeric arsenic (As_2) versus the tetrameric As_4 traditionally used for (111)-oriented growth. I discovered several differences between As_2 and As_4 grown TSQDs, which provides a greater ability to tailor TSQDs and reveals

different nucleation and growth kinetics. I also uncovered that GaAs(111)A has three distinct morphologies that depend on the substrate temperature and arsenic species used, these include high symmetry hexagon TSQDs and two orientations of triangular TSQDs. For the hexagonal and both types of triangular TSQDs, growth with As_2 exhibits higher photon emission intensity compared to As_4 grown TSQDs, an indication of improved crystal quality (essential for reliable optoelectronic devices).

Finally, in Chapter 5 I present a complete roadmap for tuning TSQD structural and optical properties, and reveal the growth-parameter conditions for optimized TSQD emission and entangled photon emission. I also provide a discussion of the future work that will be required to complete the quantum optical analysis and device integration of GaAs(111)A TSQDs.

This comprehensive analysis of GaAs(111)A TSQD growth provides an essential foundation for future (111)-surface and TSQD research and applications. My exploration of the many unique and interesting properties of GaAs(111)A TSQD growth provides new insights into the physics of the nucleation and growth of tensile-strained (111)-surface. The additional investigation to the science behind TSQD formation and optical properties provides an essential foundation for understanding (111)-oriented TSQD capabilities, with an eye toward the many yet unexplored TSQD materials systems. The use of this guide to optimize TSQDs for entangled photon emission cements the utility of this roadmap. The many promising device applications of (111)-oriented TSQDs, including robust and easily integrated entangled photon LED materials made in a single processing step, are now a real possibility.

TABLE OF CONTENTS

LIST OF TABLES

LIST OF FIGURES

LIST OF ABBREVIATIONS

a_c	Conduction band hydrostatic deformation potential
ADF	Annular dark-field
AFM	Atomic force microscopy
Al	Aluminum
As	Arsenic
a_v	Valence band hydrostatic deformation potential
b	Shear deformation potential
Be	Beryllium
BEP	Beam equivalent pressure
D	diffusion constant
DFT	Density functional theory
E	Activation energy
EELS	Electron energy loss spectroscopy
f	scaling function
F	deposition flux
FCC	Face centered cubic
FIB	Focused ion beam
FM	Frank-van der Merwe (layer-by-layer growth)
FSS	Fine structure splitting
Ga	Gallium

GaSb	Gallium antimonide
GaAs	Gallium arsenide
GaTe	Gallium telluride
Ge	Germanium
h_{AFM}	QD height measured with AFM
hh	Heavy hole
H(r)	Hamiltonian operator
HRTEM	High resolution transmission electron microscopy
h_{QD}	QD height
h_{WL}	WL height
i	Critical cluster size: one atom less than the number needed for nucleation of a stable island
I_0	Integrated intensity
In	Indium
InAlAs	Indium aluminum arsenide
InAs	Indium arsenide
InGaAs	Indium gallium arsenide
InP	Indium phosphide
IR	Infrared
K	Kelvin
k_B	Boltzmann constant
kMC	Kinetic Monte Carlo
LED	Light emitting diode

lh	Light hole
LN_2	Liquid nitrogen
$L_xL_yL_z$	Cuboidal QD dimensions
m	Schmid factor
$m^*(r)$	Effective mass
MBE	Molecular beam epitaxy
meV	Millielectron volt
ML	Monolayer
$M_{lmnl'm'n'}$	Wave function matrix elements
nm	Nanometer (1×10^{-9} m)
n_s	Areal density
n_x	Areal density (of average islands cluster size x)
PBN	Pyrolytic boron nitride
PID	Proportional-integral-derivative
PL	Photoluminescence
PN	P-type/n-type junction
PV-TEM	Plan-view transmission electron microscopy
RGA	Residual gas analyzer
RHEED	Reflection high-energy electron diffraction
RMS	Root mean squared
RIO	RHEED intensity oscillation
s	Number of atoms in an island cluster
s_{av}	Average number of atoms per cluster across an array of islands

Sb	Antimony
SK	Stranski-Krastanov (islands-on-layer growth)
Si	Silicon
sp^2	Hybrid orbital of one s-orbital and two p-orbitals
sp^3	Processing-structure-properties-performance
STEM	Scanning transmission electron microscopy
STM	Scanning tunneling microscopy
T	Temperature
t_c	Wetting layer thickness
TC	Thermocouple
TEM	Transmission electron microscopy
T_{SUB}	Substrate temperature
TSQD	Tensile-strained quantum dot
QD	Quantum dot
QIS	Quantum information science
QW	Quantum well
VSCEL	Vertical-cavity surface-emitting laser
VW	Volmer-Weber (island growth)
W	Watts
WL	Wetting layer
XRD	X-ray diffraction
XTEM	Cross-sectional transmission electron microscopy
0D, 1D, 2D, 3D	Zero, one, two, three dimensional

$\hbar$	Reduced Planck constant
ºC	Degrees Celsius
µeV	Microelectron volt
Å	Angstrom (1×10^{-10} m)
µm	Micrometer (1×10^{-6} m)
γ_e	Epilayer free energy
γ_i	Interface (surface-epilayer) free energy
γ_s	Surface free energy
$\varepsilon_{\parallel}$	In-plane strain
$\varepsilon_{\perp}$	Perpendicular strain
θ	ML coverage
λ	Angle between applied force direction and slip direction
λ_{Ga}	Ga adatom diffusion length
σ	Applied stress
τ_R	Resolved shear stress
$\tau_R(b_{30})$	Resolved shear stress of a 30º partial dislocation
$\tau_R(b_{90})$	Resolved shear stress of a 90º partial dislocation
ϕ	Angle between applied force direction and slip plane normal
$\{\varphi\}$	Basis sets
$\psi(r)$	Envelope function

CHAPTER ONE: MOTIVATION AND BACKGROUND OF TENSILE-STRAINED QUANTUM DOTS

1.1 Motivation

Quantum information science (QIS) promises exponentially faster computing and unbreakable communication security. Quantum computing devices utilize non-deterministic processing, with 2^n states for n qubits (quantum bits) versus 2n states for n classical bits [1]–[3]. Quantum encryption devices utilize the superposition of entangled quantum states as a purely random encryption key that self-reports tampering. Significant research efforts into these technologies are hence already underway [1], [3]–[11].

Researchers are pursuing many methods for producing superposition, including atomic spin, non-linear optics, and superconducting currents [12]–[19]. Although these approaches have their advantages, each also suffers from specific drawbacks, including being non-tunable, having poor bandwidth, requiring extreme environments, and/or being bulky and expensive [4], [5], [12], [20], [21].

Entangled photons provide an attractive alternative basis for QIS devices because they can be generated in simple, tunable nanostructures called semiconductor quantum dots (QDs) [1], [22]–[24]. QDs represent an optimal system for reliable photon entanglement devices (Section 1.2.6) [5], [22], [25]–[27]. Additionally, QDs are compatible with existing solid-state optoelectronic chip architectures, they can be placed into optical cavities for high extraction efficiency (***Figure 1.1***), and coupling between

pairs of patterned or stacked QDs can exhibit tunneling entanglement [6], [12], [27]–[31]. Advanced device fabrication has led to electrically and optically triggered QD qubit gates [1], [7], [29], [30]. These advantages have led to renewed research into the epitaxial growth of semiconductor QDs for QIS applications.

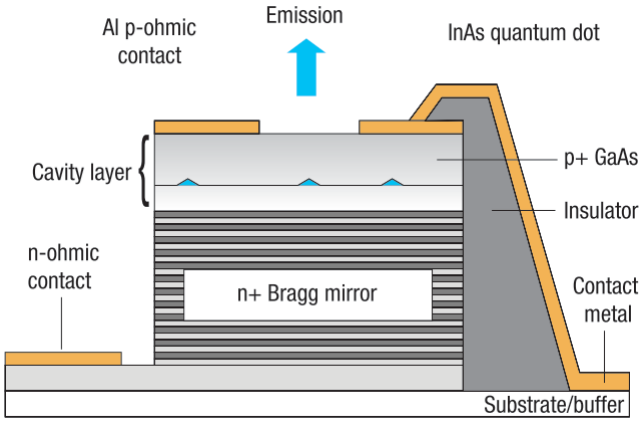

Figure 1.1: Schematic of a QD light emitting diode (LED) device for electrically triggered single-photon and entangled photon emission (reproduced from [22]). QDs are integrated into a p-i-n doped structure in an optical cavity with a high-reflectivity Bragg mirror and an emission aperture. The eventual TSQD LED device we aim to produce (see Chapter 5) will have a similar structure.

Despite the promise of epitaxially grown QDs, the asymmetry (elliptical structure and piezoelectric field) of conventional (100)-oriented QDs means that they are inherently inefficient sources of entangled photons (Section 1.2.6) [32]–[34]. Many creative, though complicated, time-consuming, and expensive, approaches have been developed to improve entangled photon emission from QDs. These approaches include pre-patterning, post-selection, annealing, and electromagnetic tuning [4], [5], [26], [34], [35]. However, even with these complex solutions, significant challenges remain, such as maintaining coherence in devices, reliably detecting photon entanglement, and eventual fabrication requirements of high through-put and easy device integration [1], [3]–[5], [22], [35].

In contrast to the (100) surface, (111) surfaces have the highest structural and piezoelectric field symmetry among the low-index crystal planes (Section 1.2.6). QDs grown on (111) surfaces are hence expected to exhibit enhanced entangled photon emission compared to (100) QDs (Section 1.2.6). However, the accepted truth was that the self-assembled growth of QDs on (111) surfaces is impossible. Previous attempts to use compressive strain, the driving force behind traditional (100) QD self-assembly, to produce (111)-oriented QDs failed. Instead of QD self-assembly, compressive strain is relieved on the (111) surface by the formation of dislocations (Section 1.2.7) [53].

To address this problem, Simmonds and Lee developed a method that used *tensile,* instead of compressive, strain to produce the self-assembly of (111)-oriented QDs [36]. Due to the peculiar tensile strain relaxation properties of the (111) surface, this method produces dislocation-free QDs with the high symmetry necessary for robust photon entanglement (Section 1.2.7) [37], [38]. Unlike other methods of synthesizing QDs for entangled photon emission, this strategy requires only a single processing step. Using molecular beam epitaxy (MBE) to grow the samples, we can embed tensile-strained QDs (TSQDs) in high-purity, high-mobility semiconductor media, with planar structures for simple device integration.

In addition to driving the (111) TSQD self-assembly process, the presence of tensile strain allows us to tunably reduce the electronic band gap (***Figure 1.20***). This is a powerful tool that could help us push TSQD entangled photon emission into the infrared (IR) and hence to couple QIS devices with existing fiber optic networks. Tensile strain effects on the semiconductor band structure also open research avenues into IR sensing, semiconductor-to-semimetal conversion, transforming Ge into a direct band gap

semiconductor, and thermophotovoltaics [39], [40]. Finally, TSQDs represent an inversion of conventional compressively strained buffer-QD material combinations. This inversion effectively doubles the number of materials systems available for creating QD-based heterostructures, and hence opens unexplored opportunities for identifying new physics and materials properties.

Preliminary TSQD growths on the (111) surface have verified these promising capabilities [38]. (111)-oriented TSQDs exhibit structural and optoelectronic tunability, as well as the low fine structure splitting (FSS) between biexciton states that is necessary for detecting entangled photon emission (Section 1.2.7) [38]. However, the fact that (111) TSQDs were discovered so recently means that prior to my research, only proof-of-concept growths had been carried out. The growth parameter phase-space of this promising new materials system was hence almost completely unexplored.

This work explores the MBE growth parameters that give rise to the self-assembly of (111)-oriented TSQDs and develops a guide for future research and device fabrication based on these novel nanostructures. To obtain a comprehensive understanding of this new materials system, I have completed a detailed investigation of TSQD structural and optical properties as a function of MBE growth parameters. I have focused specifically on GaAs/InAlAs(111)A TSQDs, which are likely to have similar processing-structure-properties-performance (sp^3) to other (111)A TSQD materials systems that will be the subject of future research.

1.2 Background

To grow and understand the (111)A TSQD family requires foundational knowledge of the technique used to grow them, as well as an understanding of the mechanisms involved in the growth of traditional QDs (e.g. InAs QDs in bulk GaAs(100) (InAs/GaAs)). To this end, this background section reviews MBE growth and characterization, zinc blende crystal structure and properties, (100) surface nucleation and growth, and previous (111) surface TSQD results (***Figure 1.2***).

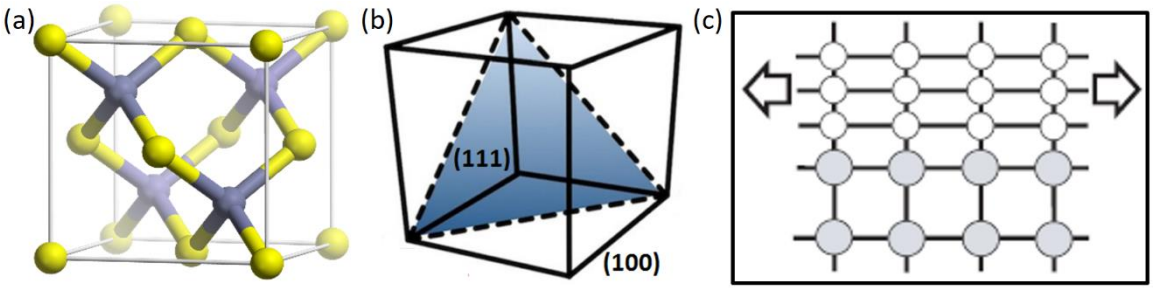

Figure 1.2 Basic structural features of (111) TSQDs. (a) Schematic of the zinc blende crystal structure unit cell, with interpenetrating FCC structure of two different elements (blue and yellow). (b) The (111) plane (blue, dashed outline) in reference to the (100) plane which bounds the typical unit cell. (c) A lattice of tensile-strained atoms, due to their crystal registry with a larger underlying lattice.

1.2.1 Molecular Beam Epitaxy

MBE provides selective thermal evaporation/sublimation of ultrahigh-purity (≥99.999% pure) elements onto a substrate, with atomically precise control of material composition and interface abruptness. These ultrahigh purity source materials are stored in chemically-inert pyrolytic boron nitride (PBN) crucibles within effusion cells. The effusion cells are heated until they emit beams of atoms or molecules. These atomic/molecular beams are then incident on a heated crystalline substrate where material growth occurs (***Figure 1.3***).

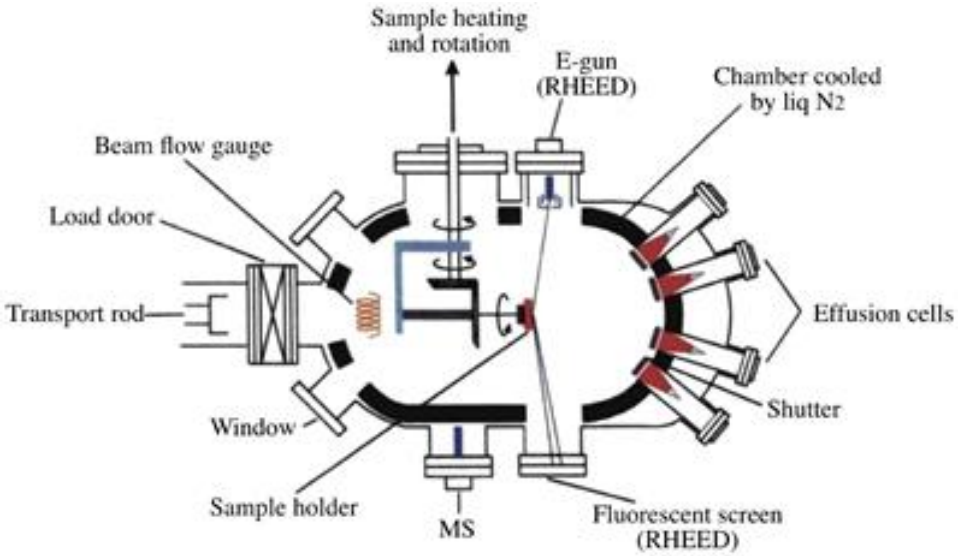

Figure 1.3: Schematic of a generic MBE growth chamber. Source material is housed in effusion cells, where it is evaporated/sublimated onto a growth substrate (mounted on a heated and rotating sample holder). Pneumatic shutters effectively provide on/off switches for material incorporation. Pumps and liquid nitrogen (N_2) cooling ensure high purity growth. Various detectors (RHEED, MS, beam flow gauge, windows) allow for in-situ monitoring. Image reprinted from A. R. Barron, "Chemistry of Electronic Materials," Rice Univ. course CHEM-496 Chem. Electron. Mater., chapter 6.1: Molecular Beam Epitaxy, 2009, under Creative Commons License [41].

The cells are idled below their typical growth temperatures to preserve material, and not increased above the degas temperature to prevent excessive evaporation or damage to the cell (***Table 1.1***). Special considerations are necessary for many elements. During the growth of III-V semiconductors we typically use excess overpressures of the Group V elements to maintain surface stoichiometry, due to their sticking coefficient of < 1. We therefore load large quantities of these elements (often over 1 kilogram), which are housed in large reservoirs. Given their large thermal mass, the temperature of these reservoirs is slow to change, and so instead, we constantly maintain the Group V cells at their growth temperature, and use a precisely controllable valve to adjust the flux of molecules leaving the cell. Group V elements also sublimate as tetramers, so a high-temperature cracker (900 °C) is often used to pyrolyze them into dimers, which can

chemisorb better on the substrate. Aluminum is unusual in that it wets the PBN crucible, and so when it is frozen, the difference in contraction rates between the metal and ceramic can crack the crucible. Therefore, once it is melted, the aluminum cannot be frozen again without severe risk of damaging the effusion cell with molten metal. It is hence typically idled at 800 °C (i.e. above its melting point of 660 °C) and only cooled below its freezing point with great care. Also, Al tends to creep up the sides of the crucible with the possibility of reaching the filament and shorting it, so Al cells are cold-lipped and equipped with double-walled crucibles to prevent this. Ga can condense on the lip of the crucible, causing droplets that can fall back into the melt, explode, and eject Ga microdroplets into a growing substrate. Ga cells are thus hot-lipped with a secondary heating element to prevent condensation. Sb, Ga, and Si all expand upon freezing, however they are typically idled and grown in the same phase, so this is typically not an issue.

Table 1.1: Semiconductor source materials used with the Boise State MBE, along with the melting/freezing temperatures of the respective elements, and the cell temperatures for idling, growth (typically), and degas. The group V elements (As and Sb) have a reservoir and cracker, temperatures for both are listed respectively.

Source material	Melting temp. (ºC)	Idle temp. (ºC)	Growth temp. (ºC)	Degas temp. (ºC)
Gallium (Ga)	30	500	800-1000	1050
Indium (In)	152	400	700-850	900
Aluminum (Al)	660	800	1000-1150	1200
Arsenic (As)	613	385 / 900	375-395 / 600-900	400 / 900
Antimony (Sb)	630	515 / 900	500-530 / 650-900	570 / 950
Germanium (Ge)	938	600	1100-1200	1250
Silicon (Si)	1414	600	950-1200	1200
Beryllium (Be)	1279	400	600-800	800
Gallium telluride (GaTe)	937	150	400-600	650

When heated the material either sublimates from the solid (Group V elements and dopants) or evaporates from the melt (Group III elements and Ge), travels through a narrow passage surrounded by water cooled shrouds (for a nearly collimated atomic/molecular beam), and then deposits on a heated rotating substrate, for controlled and uniform growth (***Figure 1.3***). We control beam fluxes (i.e. number of atoms per unit area per unit time) for the different elements by controlling their respective effusion cell temperatures. Effusion cell temperature is in turn controlled with heating elements under proportional-integral-derivative (PID) programming using effusion cell thermocouple (TC) feedback. Beam fluxes are typically low enough that growth rates are measured in monolayers per second (ML/s) or μm/hour.

We tune the effusion cell temperatures prior to growth based on the desired growth rates and material compositions. Growth rates are set based on a beam equivalent pressures (BEP) detected by a retractable ionization gauge (background flux monitor,

a.k.a. beam flow gauge) placed directly in front of the substrate (***Figure 1.3***). We compare BEP against calibration curves that relate cell temperature, material flux, and growth rate. For example, a Ga cell temperature range of 860–1000 ºC relates to a BEP of 1.2–21 × 10^{-8} Torr and growth rates of 0.048–0.74 ML/s. These correlations will vary with different cells, growth chamber layouts, and as material is depleted. We can selectively block individual atomic/molecular beams with pneumatic shutters to quickly control deposition layer content and create abrupt interfaces (***Figure 1.3***). We can achieve precise creative control over individual atomic layers (MLs) using this system.

Single-crystal substrates are the foundation upon which our samples are grown. We select our substrate material based on the desired lattice parameter of the overlying sample growth. Substrate wafers are mounted using either a retaining clip holder or molten indium to a molybdenum block, which is then loaded onto the growth chamber substrate heater and rotation component (***Figure 1.3***). Substrate temperature is a major factor in materials' kinetic and thermodynamic, and therefore nucleation and growth, properties. We therefore also regulate substrate temperature using a PID-controller with TC feedback. We continuously monitor substrate temperature with both the TC and an optical pyrometer. While neither TC nor pyrometer are completely precise, we calibrate their readings against known deoxidation and surface morphology transition temperatures detectable by reflection high-energy electron diffraction (RHEED) (***Figure 1.3***). The RHEED pattern transitions from a haze to evenly spaced streaks with desorption of the native oxide, which for GaAs(100) occurs at about 580 ºC [42], GaSb(100) at about 530 ºC [43], and InP(111)A under As_4 flux at about 520 ºC [44]. The RHEED pattern for surface reconstructions are visualized in reciprocal space due to diffraction, such that a 2

× represents a narrower repeating surface structure with wider spaced RHEED streaks than a 4 ×. GaAs(100) during typical growth conditions has a streaky (2 × 4) pattern (when oriented to see the 2 ×, a 90º rotation of the substrate presents a 4 ×), which with an As_4 BEP of 10^{-5} Torr transitions to a $c(4 \times 4)\beta$ below 525 ºC and to a (2 × 1) above 625 ºC [45]. The GaSb(100) surface transitions from a (5 × 1) to a (3 × 1) below around 400 ºC [43]. Group V overpressure is required while heating the substrate due to the volatility of group V elements compared to group III. For example, if GaAs(100) does not have As:Ga of at least 1.6:1 above around 400 ºC than As sublimation will result in the formation of Ga droplets on the surface, ruining the sample [45].

Sample purity is achieved using ultra-high purity elements (≥99.999% pure) and sputter-ionization (ion) and cryogenic (cryo) vacuum pumps that keep the central growth chamber under ultra-high vacuum ($<10^{-9}$ Torr). The ion pump is an entrapment pump with an electrode system of closely spaced anodes between cathode plates that generates electrons and ions (a cold-cathode Penning system) [46]. The electrons travel a spiral track under the influence of large permanent magnets and ionize gases [46]. Both the electrode system ions and ionized gases impinge on the titanium cathode material, simultaneously embedding in it and sputtering titanium that acts as a getter for reactive gases [46]. The cryo pump is an entrapment pump that uses recirculating compressed helium to cool fins on a cold head to < 15 K, onto which gases condense [46]. Cryo pumps must be periodically regenerated (brought to room temperature to desorb gases) to maintain the pumping capabilities of the condensing surfaces. Chamber pressure is monitored using hot-cathode ion gauges and a residual gas analyzer (RGA). Ion gauges have cathode filaments that generate electrons which pass through an anode grid to

collide with and ionize gas molecules [46]. The ionized gases are then attracted to a negatively charged central collector and generate a current that is amplified and converted to a pressure readout [46]. The RGA operates as a mass spectrometer (MS) (***Figure 1.3***), a filament wire is used to ionize gases which pass through an anode wire cage and selectively pass through a quadrupole based on their mass/charge (some fraction of gases will be doubly ionized and appear as peaks at 1/2 their actual mass) [46]. A liquid nitrogen (LN_2) cryopanel surrounding the substrate cools it to 77 K to condense atoms not directly deposited on the substrate from the effusion cells to locally lower the pressure, and also reduce the thermal load from the substrate heater on the surrounding chamber (***Figure 1.3***). Atmospheric impurities introduced during sample loading are reduced using a load-lock intro-chamber where we first reduce the pressure to $< 10^{-5}$ Torr with a turbomolecular pump (a kinetic pump with rapidly spinning rotors which generate unidirectional airflow). The turbo pump is backed with a dry roughing fore-pump, such as a scroll pump, which does not use oil that could travel upstream and contaminate the system. The intro-chamber is then thermally degassed to over 100 ºC and switched from the turbo pump to an ion pump. The intro-chamber is isolated from the growth chamber by an ion pumped transition chamber to further minimize introducing impurities into the growth chamber. These controls help to minimize defects and maximize charge carrier mobility in the epitaxial samples ensuring excellent material quality.

Semiconductor materials are selected for their relative lattice constants, electronic band gaps (***Figure 1.4***), and valence (donor type). As shown in ***Table 1.1***, the Boise State MBE system includes the following elements: group III (Al, Ga, In), group V (As, Sb),

group IV (Ge), and dopants (Be, p-type; Si, amphoteric but generally n-type; GaTe, n-type).

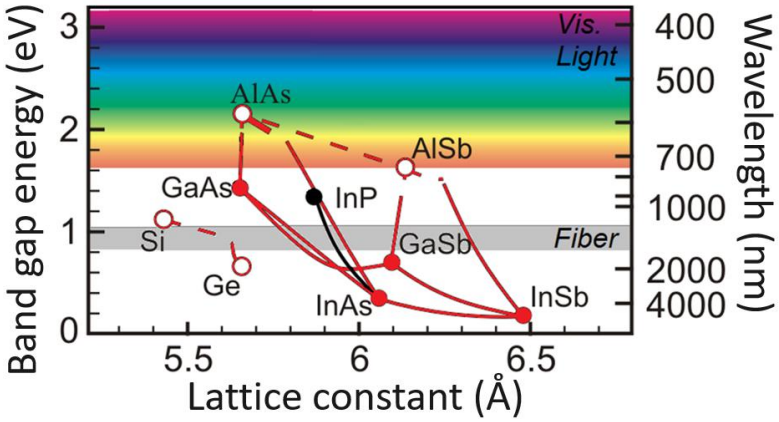

Figure 1.4: Band gap energy versus lattice constant. These relationships are well established for III-V materials and allow lattice-matching of buffers to substrates, strain tuning of epilayer materials, and band gaps engineering and quantum confinement. Red lines/ dots represent materials system used with the Boise State MBE, black lines/ dots represent materials only used as substrates, solid lines/circles represent direct band gap materials while dashed lines/ open circles represent indirect band gap materials. Image reprinted and adapted with permission from Simone Montanari, Fabrication and characterization of planar Gunn diodes for monolithic microwave integrated circuits (2005), PhD thesis, University of Aachen RWTHI [47].

We select and tune structural and optoelectronic properties based on device specification. MBE can make bulk (3D), quantum well (QW) (2D), nanowire (1D), and QDs (0D) semiconductor structures, with or without doping. Depending on lattice mismatch and ML thickness, MBE is often used to create dislocation-free heterostructures of repeatedly alternating QW materials, or self-assembled QD nanoclusters. For example, GaAs at 300 K has a lattice constant of 5.653 Å, while InP at 300 K has a lattice constant of 5.868 Å. When GaAs is grown on material lattice-matched to InP with a (111)A orientation, the GaAs experiences a 3.8% tensile strain and spontaneously self-assembles into QDs. QD carrier confinement, homogeneous distribution, and tunable wavelength capabilities are particularly well suited to photon-

electron exchange in devices such as LEDs (***Figure 1.1***) and photodetectors, as well as entangled and single photon sources.

1.2.2 MBE Characterization

In-situ characterization of samples during growth is done using RHEED (***Figure 1.5***). Ex-situ sample characterization techniques used in this research include X-ray diffraction (XRD) (***Figure 1.6***), photoluminescence (PL) (***Figure 1.7***), atomic force microscopy (AFM) (***Figure 1.8***), and transmission electron microscopy (TEM) (***Figure 1.9***).

RHEED uses a high-energy electron beam which is diffracted off the growing substrate at a low-angle (***Figure 1.5(a)***). The resulting diffraction pattern appears on a phosphorescent screen and is captured by a high-resolution camera (***Figure 1.5(b)***). We use *EZRHEED* analysis software to study the diffraction patterns and their time evolution. RHEED patterns provide real-time information about the sample surface morphology (rough or smooth) and surface reconstruction. These RHEED patterns tell us, for example, if we are growing smooth GaAs with an As-dimer (2 × 4) surface, or if we have formed 3D InAs/GaAs(100) QDs [48], [49]. We can also use RHEED to measure the growth rate. We first pause growth and use a quick anneal to smooth the surface. Then, upon resuming growth we observe oscillations in the intensity of the RHEED pattern (***Figure 1.5***). Each period of the RHEED intensity oscillation (RIO) corresponds to the growth of a complete ML [48], [49]. We can convert the resulting growth rates in ML/s to nm/s so long as we know the lattice constant of the material we are growing.

(a)

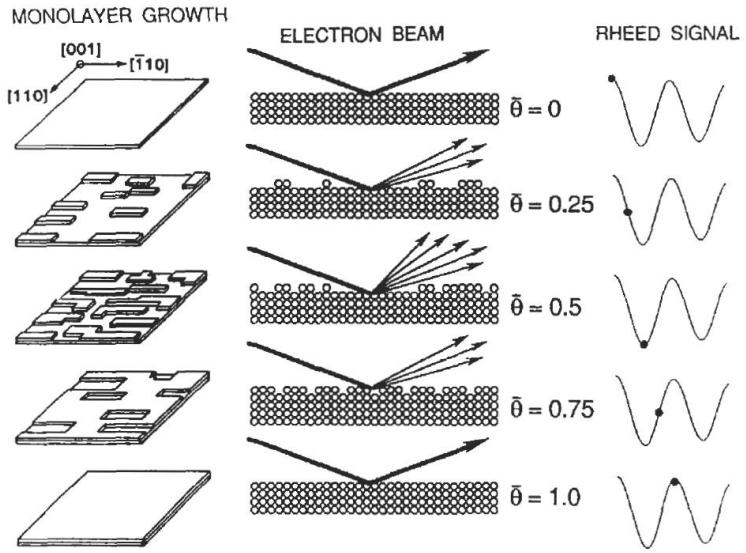

(b)

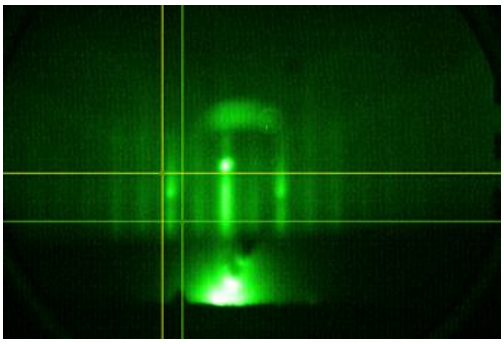

Figure 1.5: RHEED imaging. (a) Beginning with a smooth surface (θ=0) achieved by annealing, the reflected electrons experience the same diffraction conditions and provide the highest intensity streaks (seen in (b)). With further growth the surface roughens (θ between 0 and 0.5) then fills in (θ between 0.5 and 1.0), causing the RHEED intensity to oscillate dimmer then brighter. When a full ML fills in (θ=1.0), the RHEED intensity completed one full intensity oscillation, indicating the growth of a single ML. Image (a) reproduced from [54].

XRD, like RHEED, provides basic information about structural composition. Lattice parameters are calculated from the incident angle of diffracting monochromatic photons using Bragg's law. For material alloys, the measured lattice constant can be compared to Vegard's law which predicts that the composition of a ternary alloy is a

linear interpolation between the lattice constants of its binary constituents. Determining the lattice parameter of barrier alloys (e.g. $In_{0.52}Al_{0.48}As$ used for GaAs(111)A QDs) verifies (or provides information for any necessary adjustments to) the composition ratios expected from our calibrated beam fluxes in MBE. Lattice parameter verification allows us to ensure barrier alloys are lattice-matched to a given substrate (***Figure 1.6***), as well as to provide the desired amount of strain for QD formation in a lattice-mismatched material.

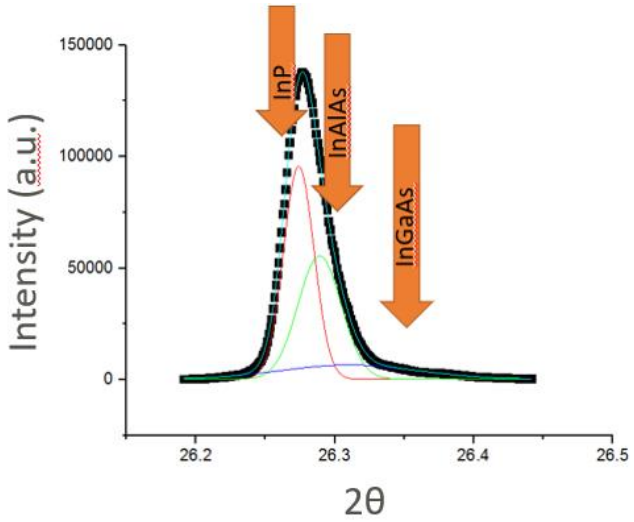

Figure 1.6: XRD spectra (black squares). Monochromatic x-rays of a known wavelength (λ) diffract from a crystal lattice at angles (θ) dependent on the lattice atomic spacing (d), per Bragg's Law ($2d\sin\theta=n\lambda$) where n is an integer value. Here, the Gaussian fits corresponding to the InP substrate (red), the InGaAs smoothing layer (green), and the InAlAs buffer layer (blue) are seen to be reasonably lattice matched.

PL spectroscopy provides band gap information about a material. A laser whose photon energy exceeds a material's band gap excites electrons from the valence to conduction band. These electrons then thermalize down to the conduction band edge, and then recombine with holes, re-emitting photons at energies characteristic of the material's band gap (or ground state, in the case of quantum confinement), which are detected with

a spectrometer. Generically, the 3D quantum confinement in QDs (Schrödinger equation solution with quantum well boundary conditions) results in a ground state energy $E = \hbar^2\pi^2n^2/(2ma^2)$, where $\hbar$ is the reduced Plank constant, n is an integer value with ground state n=1, m is particle mass, and a is the quantum well (QD) size. Therefore, QD emission energy is highly tunable with respect to QD size, with an observed red-shift in PL with increasing QD volume (Section 2.3.1) (granted, while actual QDs obey this inverse energy-QD size trend, the actual solution is more complicated (Section 3.3)). In a high-quality material, distinctive peaks represent various epitaxial layers and other electron-hole recombination centers, such as QDs (***Figure 1.7***). In contrast, crystal defects often create mid-gap states that suppress PL emission by encouraging non-radiative carrier recombination. We can also study a PL signal as a function of time (time-resolved PL) to obtain information about electron-hole recombination rates and pathways, temperature (temperature-dependent PL) to uncover carrier confinement details (***Figure 3.4***), or explore the excitation laser power-dependence of the PL spectrum (***Figure 3.S2***) to gain detailed information about band gap edges and charge carrier excited states.

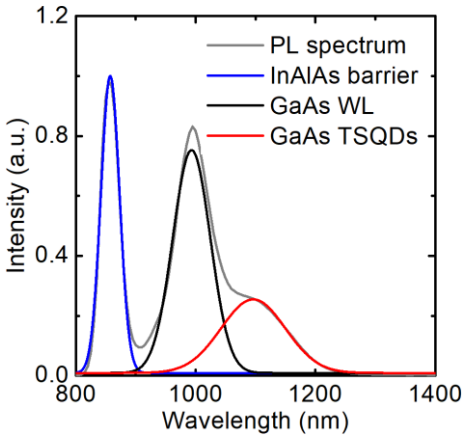

Figure 1.7: PL spectra of a 4.5 ML GaAs sample (T_{SUB}: 485 °C, GaAs growth rate: 0.075 ML/s, and As_4/Ga BEP ratio: 75). Gaussian fits to the PL trace (gray)

correspond to the InAlAs barrier (blue), GaAs WL (black), and GaAs TSQD (red) emission spectra. PL peak wavelengths are characteristic of the bulk alloy stoichiometry, average WL thickness, and average QD volume. PL peak full-width half-maxima increase with higher WL thickness variation and ensemble QD volume distribution. Peak intensity is a function of the amount of emitting material.

AFM provides information about sample surface quality and QD morphology, which we can compare to our MBE growth conditions. For example, using a higher substrate temperature may create a smoother surface and larger QDs. We use tapping mode AFM, in which the cantilever is oscillated at its resonant frequency (~100-400 kHz) and raster scanned across a sample surface (***Figure 1.8(a)***). The tip-sample separation is piezoelectrically adjusted based on surface-interaction force-displacement oscillation damping (***Figure 1.8(a)***). This provides sub-nm height detail about a materials surface. For uncapped QDs this provides information about QD size and shape, areal density, and growth uniformity (***Figure 1.8(b,c)***). Tapping mode is preferred because the minimized surface contact reduces damage to the sample and cantilever tip.

(a)

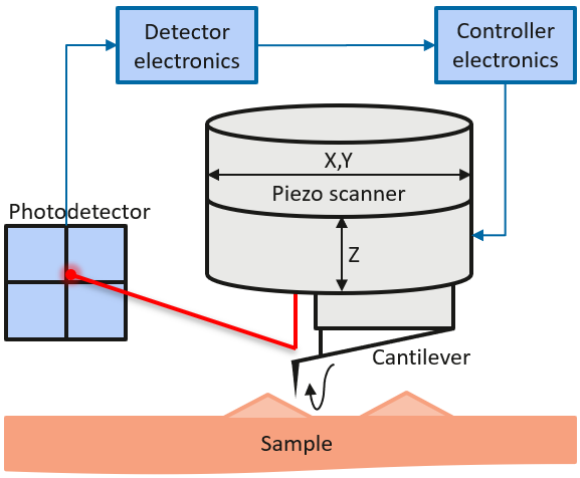

(b) (c)

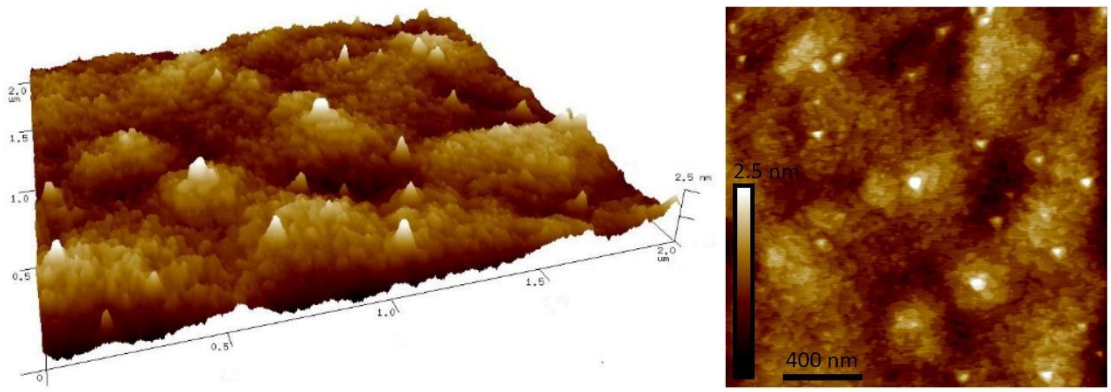

Figure 1.8: Tapping mode AFM scans. (a) Piezoelectric controls raster scan the sample surface while a cantilever with a nm-radium tip oscillates (taps) to map surface features. (b) A 3D rendering of a 3.5 ML GaAs sample (T_{SUB}: 485 °C, GaAs growth rate: 0.075 ML/s, and As_4/Ga BEP ratio: 75) revealing hills and valleys in the WL and prominent QD peaks (4 um^2, 2 nm height). (c) A 2D image of the same sample scan as (b).

In TEM we transmit a beam of electrons through a thinned sample specimen. Clusters of distinct atoms (e.g. QDs), dislocations, and strain fields alter the conditions for electron diffraction, giving rise to contrast variations (***Figure 1.9***). Plan-view TEM (PV-TEM) and cross-sectional TEM (X-TEM) allow us to visualize an individual QD's lateral and horizontal morphology, crystalline quality, and strain field.

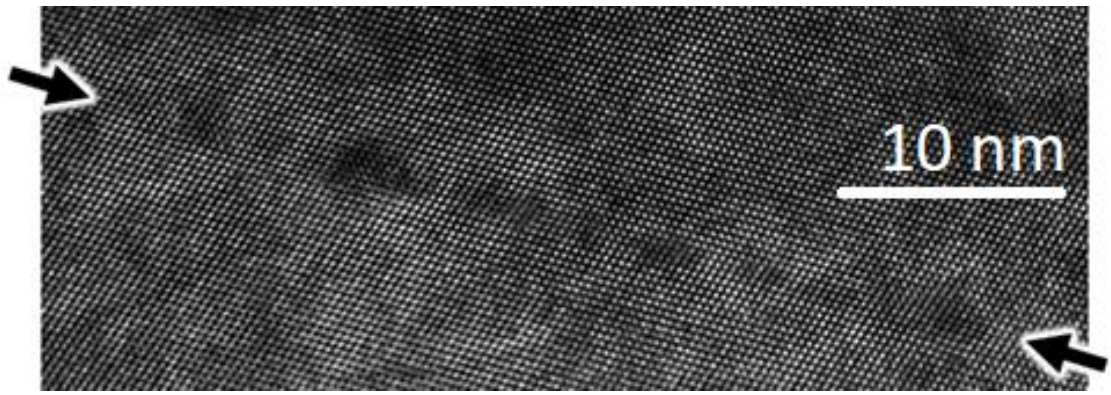

Figure 1.9: A high resolution X-TEM image of a GaAs/InAlAs TSQD sample. Diffraction from individual rows of atoms are visible. The GaAs WL/TSQDs layer is darker (demarcated by the arrows), while the InAlAs bulk is lighter due to the lower atomic mass of aluminum (therefore lower mass-thickness contrast). The perfect atomic alignment confirms that there are no dislocations in this scan area.

1.2.3 Zinc Blende Structure

III-V semiconductors adopt either a zinc-blende (ZB) or wurtzite crystal structure. Excluding the III-N family of materials, III-V semiconductors most commonly have the ZB structure, which consists of two interpenetrating face-centered cubic (FCC) sublattices. One sublattice contains the Group III elements, and the other the Group V elements, such as Ga and As, respectively (***Figure 1.10***). Group III and V atoms have similar electronegativity, causing highly covalent $4s^1 4p^3$ hybridized tetrahedral bonding. A small ionicity from electron donation results in a slightly negative Group III and slightly positive Group V charge, causing structural polarity [50]. Similarly, a small difference in atomic radii results in a strain field, causing an inherent piezoelectricity [38], [50].

Cubic crystals are highly symmetric, with equivalent lattice parameters and angles. Characteristics of the (100) surface are well researched and understood, while characteristics of the (111)A surface that is the focus of this dissertation remain comparatively unexplored. These two low index planes have distinct features due to differences in atomic arrangement and packing.

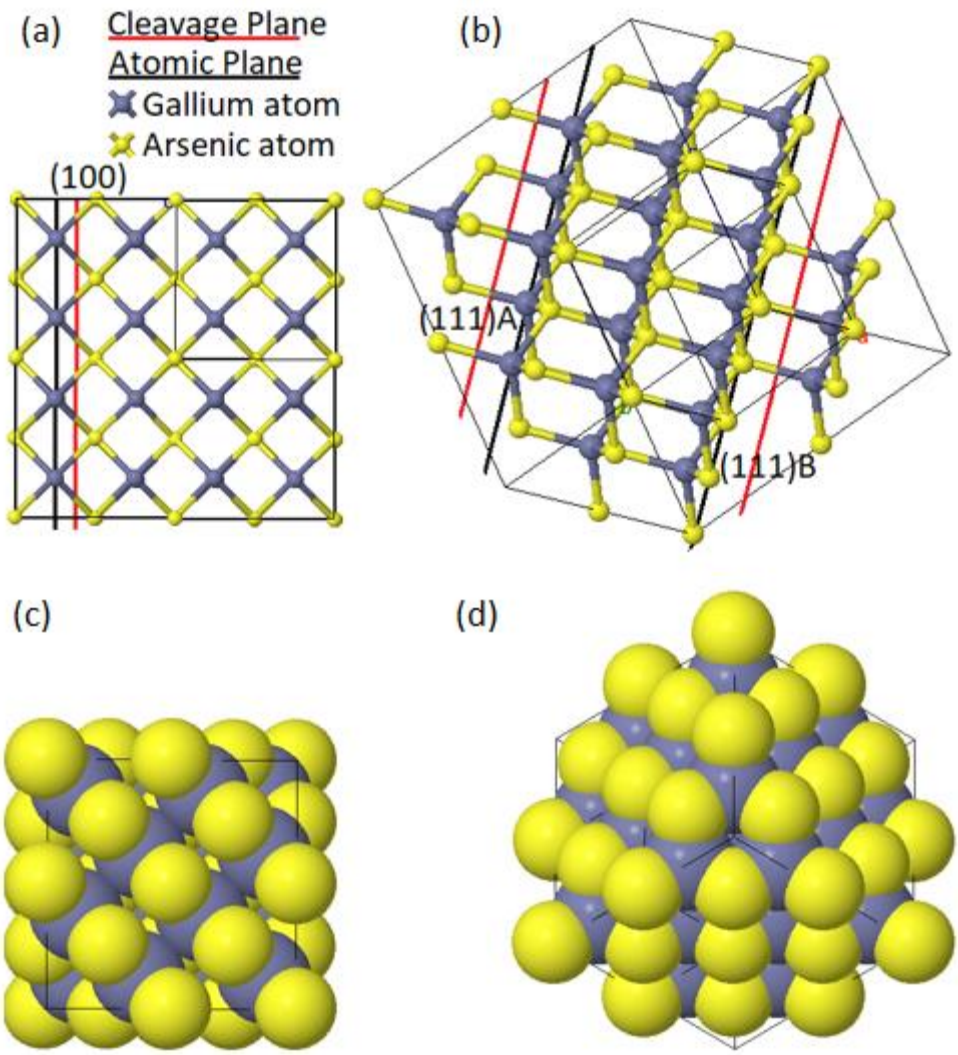

Figure 1.10: Zinc blende structural models with Ga (blue) and As (yellow) atoms, inset cubes represent the zinc blende unit cell. The ball-and-stick model of the (100) surface (a) has evenly spaced atomic (black line) and cleavage (red line) planes; the (111)A surface (b) has a wide cleavage plane above a Ga-terminated atomic plane (whereas the (111)B surface is As-terminated). The space fill model of the (100) surface illustrates the tetrahedral site GaAs bonding with two-fold symmetry (c). In contrast, the (111) surface has closer packing and three-folding bonding symmetry (d). Images rendered using Jmol molecular viewer software [51].

(100) planes have the lowest atomic density and are doubly-bonded to adjacent planes (***Figure 1.10(a), (c)***). (100) planes have a net electrostatic attraction because alternating layers are composed of entirely group III or group V atoms (***Figure 1.10(a), (c)***). These factors cause a large surface (and therefore cleavage) energy [50]. Tetragonal

bonding imposes four-fold out-of-plane electrostatic and piezoelectric fields [34].

(111) planes are close-packed, so have the highest planar atomic density (***Figure 1.10(d)***) of the low index surfaces. Like (100) they have alternating layers of group III and V atoms that are electrostatically attracted (***Figure 1.10(b), (d)***). Although (111) is the primary cleavage plane in FCC structures, this electrostatic attraction between layers increases the surface energy [50]. The atomic arrangement of the (111) planes preserves a three-fold symmetry in electrostatic and piezoelectric fields (***Figure 1.10(b), (d)***) [34].

(111) planes are distinct in that each atom is triply-bonded in one direction and singly-bonded in the other (***Figure 1.10(b)***). This polarity distinguishes Ga-terminated (111)A and As-terminated (111)B surfaces. (111)B surface atoms have two remaining valence electrons, making them more chemically active [50]. In contrast, (111)A surface atoms lack two electrons, causing a preferential sp^2 electron orbital hybridization [52]. This hybridization is physically restrained by the bulk structure, resulting in a compressive force on (111)A surfaces [52]. This mechanism causes spontaneous bending in III-V thin films, and is likely therefore to impact the stability of tensile-strained QD formation on (111)A surface [52]. Crystal structure, orientation, and bond polarity, along with Group III and V electron affinity differences, are defining properties in growth kinetics and surface reconstructions on this surface [50].

1.2.4 (100) Surface Nucleation and Growth

MBE growth modeling typically relies on density functional theory (DFT) calculations of surface energy, and kinetic Monte Carlo (kMC) simulations of atomic interactions. These models are based on and consistent with in-situ RHEED patterns and annealed-surface scanning tunneling microscopy (STM) imaging [53]. However, these

modeling efforts are complicated by the non-equilibrium nature of atomic interactions during MBE growth due to continuous atomic fluxes and high substrate temperature. Varying flux and growth temperature alter the degree of kinetic versus thermodynamic control. Although experimentally, this is very useful, theoretically, this constrains good models to narrow sets of growth conditions. The most researched model is for GaAs(100) within a typical MBE growth regime (500-600ºC, < 2 ML/sec)[53].

GaAs(100) homoepitaxy occurs via nucleation and growth of GaAs islands on a surface with alternating rows of As dimers and trenches along the [1$\underline{1}$0] direction. This surface is named $\beta 2(2\ 4)$ based on its surface unit cell reconstruction (***Figure 1.11***) [53]. From the $\beta 2(2\ 4)$ surface reconstruction, the GaAs island nucleation process involves three general steps: (1) As dimer breakage, (2) Ga pair insertion, (3) As_2 insertion. The first step requires a large population of weakly-bound As_2 precursors. The second step requires Ga binding in pairs resulting in the Ga flux (the arrival rate of Ga atoms) being a rate-limiting step. Comparison of the first and third steps implies fast As adsorption and slow dissociation. Experimentally, because respective vapor pressures of Group III and V species affect their sticking coefficients, we need a high Group V flux to prevent surface deterioration, while the group III flux dictates the growth rate.

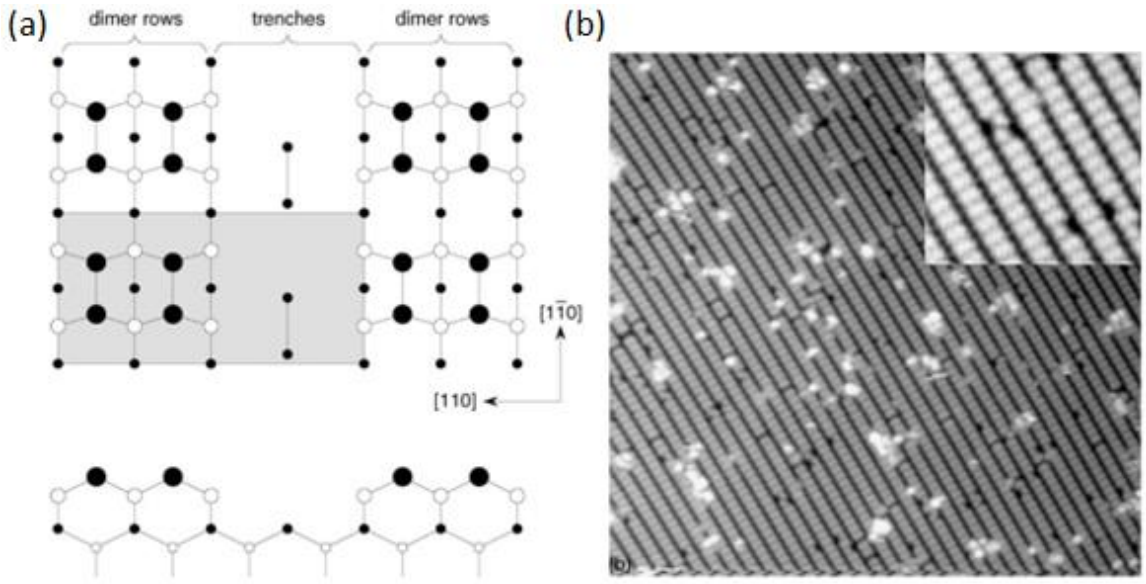

Figure 1.11: (a) (100) plan-views (top) and side-view (bottom) of the GaAs(100) surface reconstruction. Black and white circles represent As and Ga atoms, respectively; smaller size indicates closer proximity to the surface. The shaded region indicates the surface unit cell. (b) STM image after annealing and quenching (500 Å^2). The inset shows a higher resolution image (100 Å^2). The As dimers rows and trenches appear as light and dark stripes, respectively. Images reprinted from Mater. Sci. Eng. R, vol. 46, B. A. Joyce and D. D. Vvedensky, "Self-organized growth on GaAs surfaces,"pp. 127–176, 2004, with permission from Elsevier [53].

Island growth is distinct from island nucleation due to the additional contribution from adatom interactions at island edges. Computation is difficult because incorporation energy minima and adatom diffusion vary dynamically with surface morphology, chemical potential energy, and thermal energy. kMC models show that growth on (100) requires concurrent binding of pairs of Ga adatoms, confirming Ga flux as the rate-limiting step, which favors a high density of small islands [53]. Thermodynamic calculations predict a low Gibb's free energy of formation and small critical island size [54].

Qualitatively, GaAs (100) growth follows elementary reaction steps: first physisorption and surface diffusion, then either chemisorption (island nucleation or incorporation) or desorption. Low flux rates and elevated growth temperature provide

arriving adatoms sufficient time and thermal energy to diffuse until they find an ideal (low energy) binding location. In this way, islands nucleate, grow, and coalesce, and any remaining channels or voids fill in. For homoepitaxial or closely lattice-matched heteroepitaxial growth, the result is the growth of nearly perfect crystal structures in ML increments.

Heterostructures are successive layers of two or more materials systems. Different atomic constituents, doping, and physical dimensions are used for band gap engineering (e.g. QWs, QDs, and p-type/n-type (PN) junctions) or to alter phonon and photon interactions within the media (e.g. Bragg gratings). An example of a heteroepitaxial device is a vertical-cavity surface-emitting laser (VCSEL), consisting of QWs between p-type and n-type Bragg gratings; the eventual device GaAs(111)A TSQDs will be incorporated in will likely be an LED structure (***Figure 1.1***) similar to a VCSEL.

Heteroepitaxy occurs by one of three growth modes: Frank-van der Merwe (FM) or layer-by-layer, Volmer-Weber (VW) or islanding, and Stranski-Krastanov (SK) or islands-on-layers (***Figure 1.12(a)***) [53]. Growth modes are a function of relative substrate free energy (γ_s), epilayer free energy (γ_e), and substrate/epilayer interface free energy (γ_i) (***Figure 1.12(b)***). Young's equation utilizes the capillarity model to quantify this: $\gamma_s > \gamma_i + \gamma_e$ leads to FM and $\gamma_s < \gamma_i + \gamma_e$ leads to VW [54], [55]. SK occurs as a transition from FM whereby a strain field in the epilayer causes an increase in potential energy that is dependent on deposition amount [55], [56]. Conceptually, an epilayer with higher surface and interface energies than the substrate will cluster into islands (VW), while an epilayer with lower surface and interface energies than the substrate will completely cover (or wet) the surface leading to layer-by-layer growth (FM). A lattice

mismatch between the substrate and epilayer produces strain, which increases with film thickness. With continuing deposition, this strain will eventually relax either plastically by dislocation nucleation and glide, or elastically by island clustering atop the FM wetting layers (WLs) (i.e. SK growth) [53], [55]. Under the right growth conditions, SK growth results in formation of self-assembled QDs without dislocations.

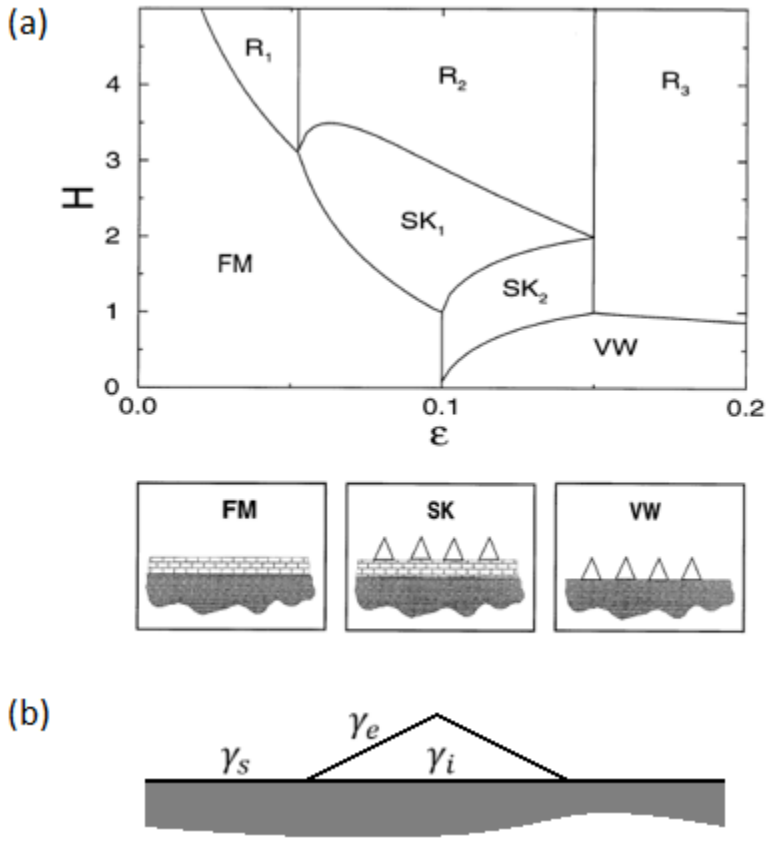

Figure 1.12: (a) InAs/GaAs (100) growth modes as a function of ML coverage (H) and compressive strain (ε) due to lattice mismatch. FM occurs at low *H* and ε, VW at low *H* and high ε, and island Ostwald ripening (R) at high *H*. SK_1 is QD formation on top of a FM WL. SK_2 is QD formation from a WL around a VW island. (c) Growth modes (FM, VW, or SK) are dependent on the related free energies of the surface (γ_s), interface (γ_i), and epilayer (γ_e). Image (a) reprinted and adapted from Mater. Sci. Eng. B, vol. B67, A.-L. Barabási, "Thermodynamic and kinetic mechanisms in self-assembled quantum dot formation," pp. 23–30, 1999, with permission from Elsevier [57].

With increasing deposition, both SK and VW QDs increase in size and areal density, which will eventually lead to Ostwald ripening (R) where the QDs begin merging to reduce total QD surface area (***Figure 1.12(a)***).

1.2.5 Self-assembled Quantum Dots

QDs are nanoscale clusters of atoms. The relative band gaps of the QD and buffer materials determine carrier behavior. For example, a type-I QD offers quantum confinement of charge carriers in both the conduction and valence bands. 3D quantum confinement creates a nominally delta-function-like density of states (with ground states pushed above the bulk band edges) so that QDs act as artificial atoms. These confined states can be identified using micro-PL of individual QDs, with characteristic peaks for each state. We can tune the position of the confined states by controlling the size of the QD. The energy transitions of a QD band gap are a function of material selection (i.e. bulk band gap) (***Figure 1.4***), QD size, and strain field. Arrays of uniform QDs are useful for wavelength specific optoelectronic devices, as well as entangled photon emitters [58]. The Coulombic attraction between an electron and hole can couple them into an exciton. A pair of excitons can form a biexciton. The electron (and hole) pairs in a biexciton will have opposite spin as required by the Pauli exclusion principle. The relaxation of these biexcitons, given the right conditions (Section 1.2.6), may generate entangled photons.

For entangled photon sources, the need for high symmetry (Section 1.2.6) means that controlling shape is perhaps even more important than areal density and size.

For the traditional InAs/GaAs (100) system (***Figure 1.13(a)***), modeling predicts QDs with a truncated pyramidal shape, AFM reveals a spherical shape, and RHEED indicates a curved elliptical shape (***Figure 1.13(b)***) [53], [59], [60]. STM analysis

supports the elliptical shape; however, detailed STM analyses of QD capping and surface energy calculations versus island size reveals a spectrum of possible shapes [53], [61]. Island size and areal density are linked by both material conservation and the strain field around larger QDs [53], [59]. Growth conditions often determine size versus areal density (e.g. a faster growth rate leads to a high density of small QDs, whereas a higher substrate temperature leads to a low density of large QDs) [53], [62], [63].

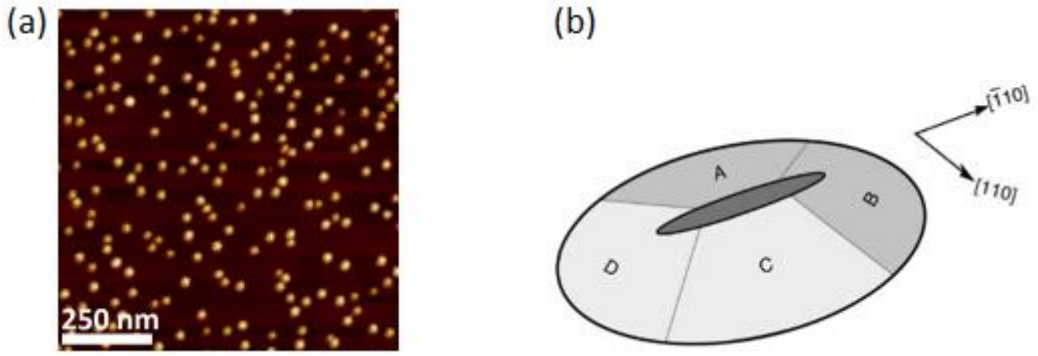

Figure 1.13: (a) A 4 ⌈m^2 AFM image of (100) InAs/GaAs QDs (average height 7.76 nm, average diameter 30.5 nm, average volume 3080 nm^3, aspect ratio (height/diameter) 0.25, areal density 181 µm^{-2}). (b) RHEED predicted lenticular shape of InAs QD shape. Image (b) reprinted from Mater. Sci. Eng. R, vol. 46, B. A. Joyce and D. D. Vvedensky, "Self-organized growth on GaAs surfaces,"pp. 127–176, 2004, with permission from Elsevier [53].

The self-assembly of InAs QDs on GaAs(100) has been studied extensively [49], [53], [61], [64]. In summary:

- The 2D WL (initial FM growth) occurs as an alloyed phase of InGaAs that decreases In migration barriers and allows a large population of In adatoms before 2D to 3D transition (QD formation) [49], [53]. This is largely a kinetic process and does not occur at low flux [53].
- The transition from 2D to 3D is rapid, occurring in less than 0.1 ML. This likely occurs due to the large In adatom population agglomerating into

discrete nanostructures to provide stress relief for upward diffusing WL atoms [53]. This process is activated (temperature dependent) and occurs when strain energy overcomes surface energy barriers (ML coverage dependent) [53].

- Increased strain associated with increased island size presents a barrier to additional adatom approach and incorporation, promoting a narrow QD size distribution [53].
- QD areal density has an Arrhenius temperature dependence, strongly increasing at low ML coverage before flattening out (***Figure 1.14(a)***), and strongly decreases with In flux [53]. QD volume increases more rapidly at higher temperature (***Figure 1.14(b)***) [53]. These relations provide a sample of a growth parameter phase-space and give insight into the general kinetics and thermodynamics of growth.
- (100) QDs have a lenticular shape, elongated along the [$\underline{1}$10] direction due to surface reconstruction trenches in this direction [53], [61], [65]. This asymmetry contributes to inefficient photon entanglement from (100) QDs (Section 1.2.6).
- Island scaling theory relates areal density (n_s) of s-atom sized islands (s) with average size (s_{av}) and ML coverage (θ) to a scaling function (f). For materials systems obeying scaling, f is sensitive only to θ, adatom diffusion constant (D), and deposition flux (F). Plotting $n_s s_{av}^2/\theta$ versus s/s_{av}^2, creates a scaling plot of f that contains information about nucleation and the growth mechanism (***Figure 1.14(c)***) [53].

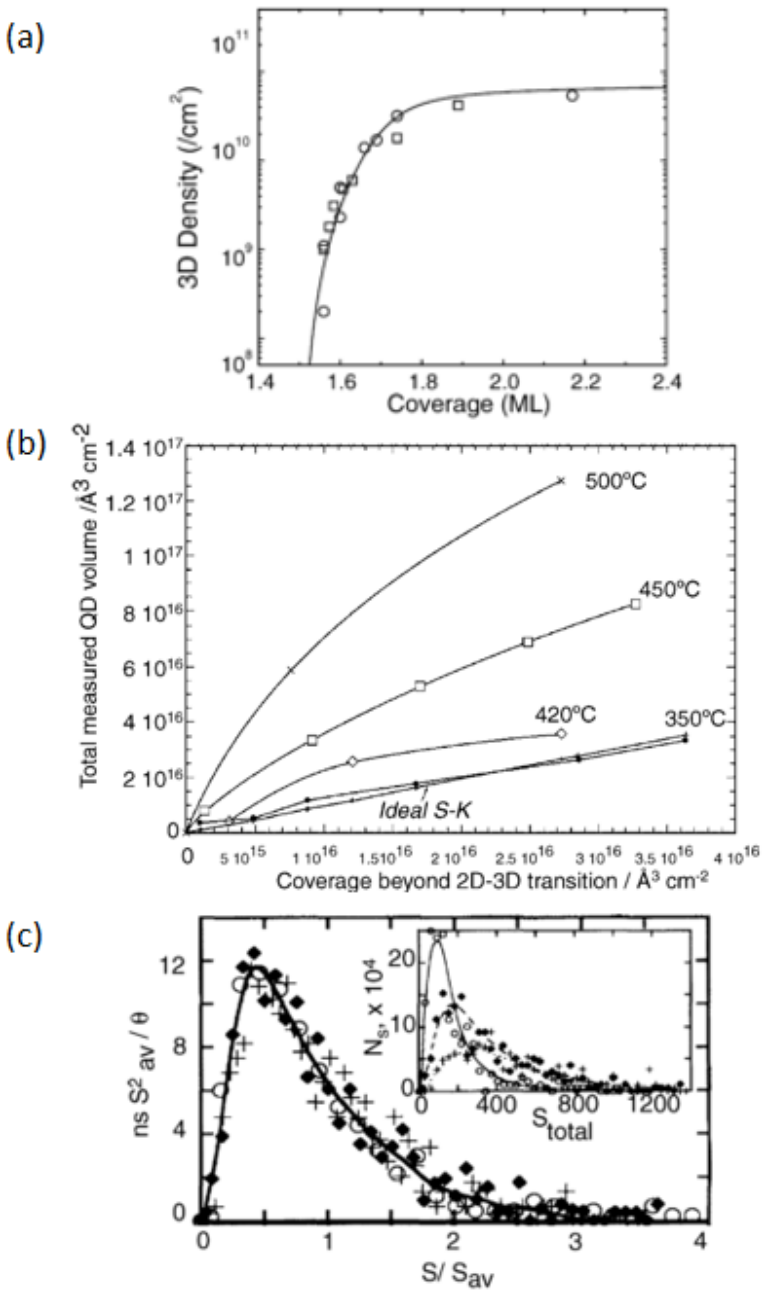

Figure 1.14: (a) QD density increases steeply then flattens out with increasing InAs coverage on GaAs(100). Squares and circles represent experimental data taken at 530 ºC and 0.01 ML/s and 500 ºC and 0.22 ML/s, respectively. The solid line is a rate equation calculation exemplifying the tunable and predictable nature of areal density. (b) InAs(100) volume increases with deposition amount and temperature. (c) Island scaling plot of InAs(100) islands with deposition amount from 0.15 to 0.35. Inset shows the unscaled island-size distributions. Taller curves indicate lower critical cluster size for stable island nucleation and higher adatom detachment rates. Images reprinted from Mater. Sci. Eng. R, vol. 46, B. A. Joyce and D. D. Vvedensky, "Self-organized growth on GaAs surfaces,"pp. 127–176, 2004, with permission from Elsevier [53].

By taking advantage of the deep body of knowledge that exists for (100) QDs, we hope to apply some of the same tools to understand the processes involved in TSQD self-assembly on (111) surfaces.

1.2.6 Entangled Photon Emission Detection

The emission of entangled photons from a QD generally relies on one of two possible radiative decay paths of a biexciton (***Figure 1.15(a)***). A small energy difference between the two intermediate exciton states of these decay paths is called the fine structure splitting (FSS) (***Figure 1.15***). Causes of FSS include asymmetric QD shape which alters carrier confinement in the orthogonal directions, as well as asymmetric piezoelectric and pyroelectric fields [26], [32], [65], [66]. FSS causes excess variation in the time-evolution phases of decay path spectral linewidths, which leads to statistical noise across the many measurements required for actual determination of entanglement [26], [67]. Therefore, detecting entanglement of photons emitted by a QD is only possible if FSS in that QD is low (< 10 μeV).

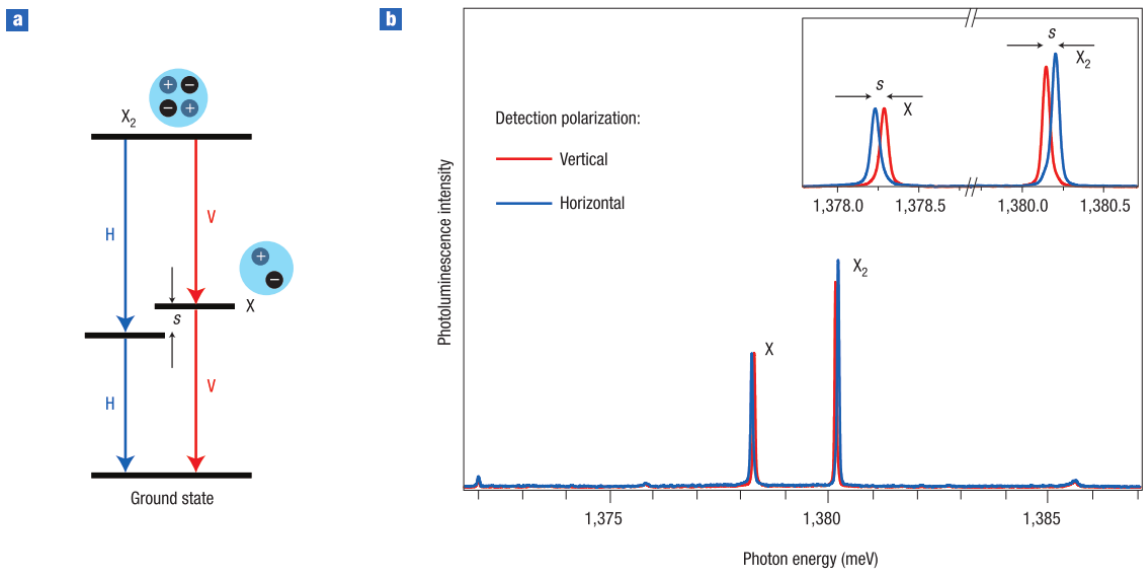

Figure 1.15: (a) QD biexciton cascade. Blue and red paths represent horizontal (H) and vertical (V) polarization specific paths. FSS is the difference in their transition energy (s). (b) PL of a QD with distinct biexciton (X_2) and exciton (X) peaks.

The piezoelectric asymmetry of the (100) surface (***Figure 1.16***) is often the largest contributor to FSS [34]. Researchers have hence tried various methods to reduce FSS such as careful pre-selection of QDs [4], [26], high magnetic- and electric-field tuning [4], [26], [35], [68]–[70], externally inducing strain [66], [71], spectral filtering [5], [25], [39], [71], and post-growth annealing [34], [72], [73]. However, these methods add complicated, expensive, and time-consuming extra steps. A single-step synthesis process for producing QD with low-FSS is preferable for scalable device fabrication.

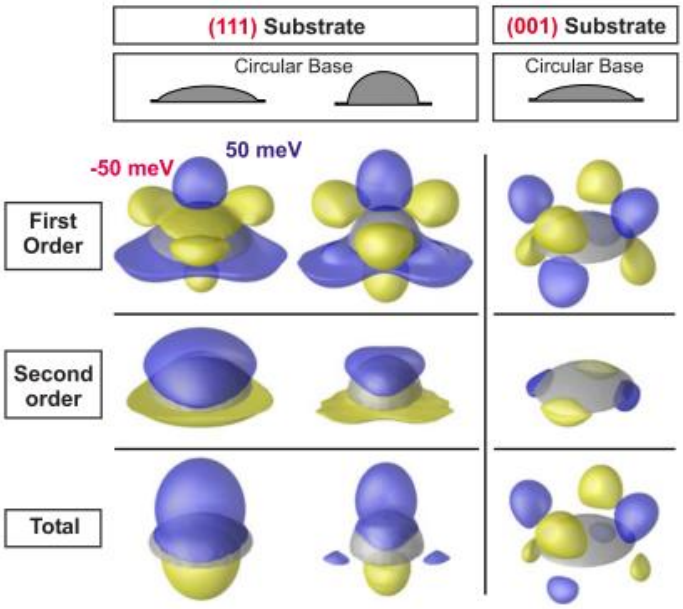

Figure 1.16: Piezoelectric fields on (111) and (100) surfaces. 1st-order, 2nd-order, and combined fields for (111) and (100) grown QDs. The total piezoelectric field has two-fold symmetry for (100) QDs, while low aspect ratio (111) QDs have a completely symmetric piezoelectric field. Image reproduced from [34].

Theory predicts that the three-fold symmetry of the (111) surface should translate to piezoelectric symmetry, leading to QDs with low FSS (***Figure 1.16***) [34]. Further, strain from QD formation elevates non-linear second-order piezoelectric effects which on the (111) surface reduce the total piezoelectric field (***Figure 1.16***) [34], [66], [74]. The magnitude and sign of these second-order terms is tunable as a function of QD composition and strain [34], [74]. This results in a symmetric, nearly absent lateral piezoelectric field and a strong vertical piezoelectric field [34]. This vertical piezoelectric field mirrors strain and material concentration gradients along this axis, but due to its low profile it does not contribute to the photon emission energy [34]. Computational mapping of electron and hole wave functions also reflects a symmetric piezoelectric component on (111) surfaces [34]. (111) QD size, aspect ratio, and composition selectively tune vertical piezoelectric field and exciton/biexciton recombination energies [34]. The latter is key for

distinguishing exciton and biexciton photons for single recombination events. Vertical piezoelectric field trends suggest that the wider, flatter, and more strained we can make a (111) QD, the lower will be its FSS. For (111) QDs, the only anticipated source of FSS is random alloying of QD ternary materials [34]. Therefore, a materials system with binary QDs (e.g. GaAs) should result in vanishingly small FSS.

Low FSS is essential to detect entanglement, but is only correlated indirectly to the quality of entanglement. Whereas FSS is a function of electric field variations, entanglement is a function of the loss of phase information due to decoherence [67], [75]. However, QDs are also ideally suited to maintain quantum coherence [75]. Most notably, QD confinement suppresses interactions with decohering phonon vibrations [75]. Further, for photonic quantum information processing, QDs simply need to maintain spin coherence long enough to generate entangled photons (which themselves have negligible decoherence) [1].

Additionally, QDs in general have highly tunable structural and optoelectronic properties, high crystalline quality, and easy semiconductor device integration [75]. A major drawback with traditional QDs is an inability to easily reach fiber-optic telecommunication wavelengths in the IR (typically 1300 or 1550 nm). [75] Due to the combined effects of quantum confinement and compressive strain which both act to increase the QD transition energy, photon emission is blue-shifted towards the UV. However, the tensile strain present in TSQDs has the opposite effect, reducing the band gap and pushing emission to longer wavelengths. TSQDs grown from materials with suitably low band gaps such as InGaAs could therefore offer access to the telecommunications bands of interest at wavelengths ~1300 nm and ~1550 nm.

Despite the promise of the (111) crystal orientation for producing QDs with low FSS, and of tensile strain for reducing QD band gaps, traditionally it has been impossible to grow QDs either on (111) surfaces or under tensile strain (***Figure 1.17***) [53]. As a result, more was known about (111) dislocations than growth kinetics on this surface.

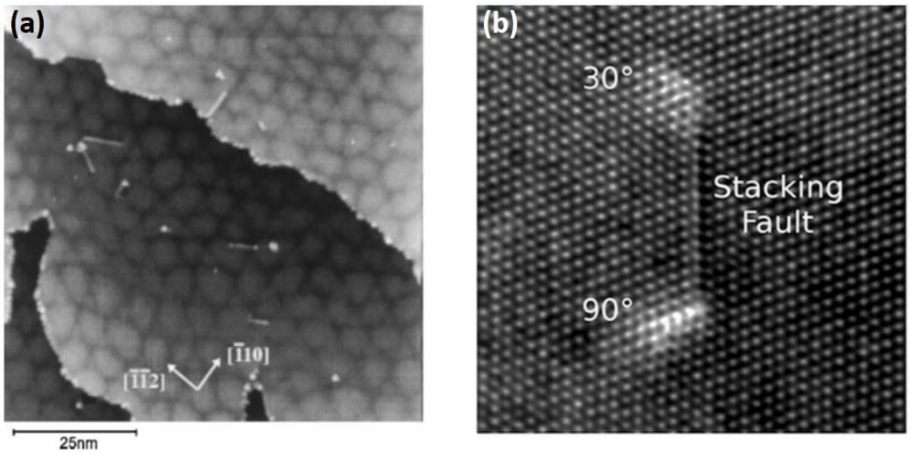

Figure 1.17: STM image of 5 ML of compressively strained InAs on GaAs (111)A with a misfit dislocation network. (b) X-TEM image of a stacking fault dislocation as occurs in zinc blende semiconductors under compressive strain on (111)-surfaces and tensile strain on (100) surfaces. Image (a) reprinted from Mater. Sci. Eng. R, vol. 46, B. A. Joyce and D. D. Vvedensky, "Self-organized growth on GaAs surfaces,"pp. 127–176, 2004, with permission from Elsevier [53]. Image (b) reprinted from [37].

Heteroepitaxial growth of InAs compressively strained on GaAs(111) begins with a (2 × 2) RHEED pattern indicating smooth 2D island nucleation and growth [53]. As the 2D InAs islands coalesce, the underlying strain field disperses in a hexagonal pattern (***Figure 1.17***) [53]. With compressive strain on the (111) surface there is hence no transition to the SK growth mode, meaning that in contrast with the GaAs(100) surface, no InAs QDs appear. With increasing ML coverage, strain relaxation occurs via interfacial misfit dislocations in the ⟨112⟩ directions, and associated threading dislocations along [110] (***Figure 1.17(a)***) [53]. Dislocation deviations from a perfect hexagonal structure indicated the presence of partial dislocation and stacking faults

(***Figure 1.17(b)***) [53]. Because of these major issues, few subsequent attempts were made to grow QDs on (111) surfaces until the predictions of low FSS were published.

1.2.7 (111) Surface Tensile-strained Quantum Dots

In the absence of a way to create self-assembled (111) QDs, researchers used droplet epitaxy (DE) [76], [77] and pre-patterned metalorganic chemical vapor deposition (MOCVD) [27], [67] to synthesize GaAs-based (111) QDs. While both methods introduce unwanted defects, researchers were able to confirm the predictions of low FSS (<10μeV) for QDs on the (111) surface [27], [67], [76], [77]. Inherent drawbacks to these methods were tolerated, because at the time they provided the only access to the promising (111) surface QD family.

Recently, Simmonds and Lee found a new way to create QDs on (111) surfaces. They discovered that dislocation-free QDs form spontaneously on (111) surfaces if you use *tensile* rather than compressive strain to drive the self-assembly process [36]. AFM and TEM revealed approximately triangular GaP/GaAs(111)A QDs with size and areal density controllable by substrate temperature and deposition thickness (***Figure 1.18***) [36].

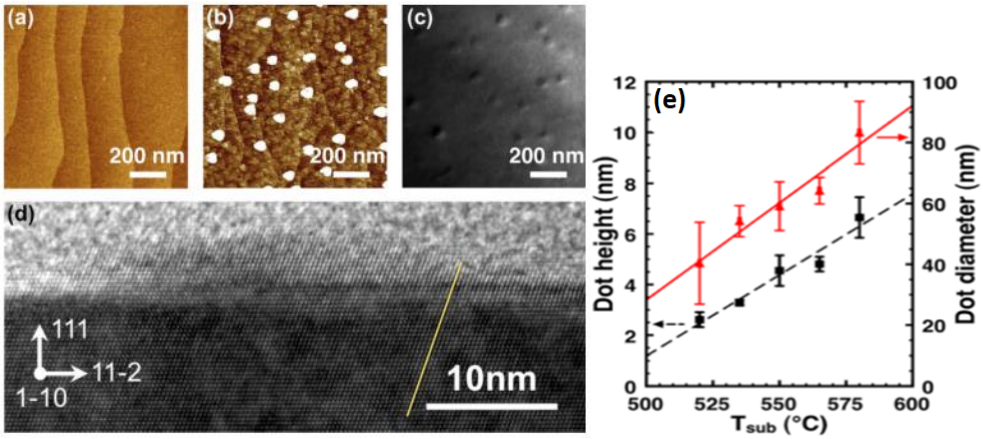

Figure 1.18: GaP/GaAs(111)A TSQDs. (a) AFM of the GaAs(111)A surface before GaP deposition. (b) AFM, (c) PV-TEM, and (d) X-TEM of TSQDs with 1.7 ML GaP. (e) Increasing temperature continuously increases QD height and diameter, indicating these as tunable GaP(111)A TSQD features. Images reprinted from [36].

Specifically, they found that increasing temperature from 460–580 ºC created larger dots with smaller areal density [36]. From 0.2–4.3 ML, increasing coverage created larger dots with an initial spike in areal density up to 0.4 ML that then gently decreased, consistent with VW growth [36]. This control over QD size and distribution is critical for meeting specific application specifications, for example, the ability to achieve a low areal density is necessary to detect FSS without using pre-patterning [34]. These first-ever (111)-oriented TSQD growths introduced a material system previously thought impossible. Going forwards, an understanding of how they form is therefore of fundamental importance.

Island scaling is obeyed during GaAs(111)A TSQD self-assembly, and shows increasing critical cluster size with increasing substrate temperature [36], [53]. Similarities between the tunability and island scaling of (111) TSQDs and (100) QDs suggest similar kinetic mechanisms are responsible for their formation. However, (111)-

and (100)-surfaces also have many differences. Thermodynamically, (111)-surfaces favor low areal density, consistent with having single Ga adatom island nucleation and the highest detachment/capture ratio among the low-index surfaces [53]. (111) TSQD spacing, size, and areal density vary from (100) QDs as expected based on their different Ga adatom diffusion lengths ($\lambda_{Ga}(111) > \lambda_{Ga}(100)$) [20], [36]. The VW growth for GaP(111)A TSQDs is consistent with the capillarity model, as GaP/GaAs has $\gamma_s < \gamma_i + \gamma_e$ [37], [52], [53]. However, using the same materials system, thus same surface free energy relationship, FM growth occurs on the (100) surface [37]. Either the sign of strain or island formation on the (111)A surface must modify the free energy relationship presented in the capillarity model [53]. The inherent strain due to surface polarities causing III-V thin film bending may be correlated [52]. There is an inherent tensile strain on the (100) surface and compressive strain on the (111) surface [52], [81]. Regardless, some additional mechanism that is dependent on surface-orientation likely exists that alters γ_e or γ_i in relation to γ_s. Tensile strain is predicted to have a higher barrier to dislocation nucleation, yet lower strain accumulation [81], [82], consistent with the early strain relaxation that occurs with VW growth.

The fact that GaP(111)A TSQDs grow by the VW mode (***Figure 1.12***) and require tensile rather than compressive strain for coherent QD growth indicates energy equilibria differences from established (100) growths. The lowest energy dislocation paths in each strain field and atomic arrangement explains the relationship between the sign of strain and the surface orientation. Zinc blende structures resolve biaxial shear stress into uniaxial shear stress along (111) planes (***Figure 1.19(a)***). Zinc blende structures also preferentially dislocate as 90º and 30º Shockley partials of a $\langle 110 \rangle$

oriented 60º total dislocation (***Figure 1.17(b)***) [37], [78]. The relation $\frac{1}{6}[\underline{11}2] + \frac{1}{6}[\underline{2}11] \rightarrow \frac{1}{2}[\underline{1}01]$ represents this dislocation [37], [78], [79]. This combination of partial dislocations has lower energy (is more likely) than the total dislocation [37], and has much lower energy than edge and screw dislocations in tetragonal systems [78]. Which Shockley partial leads is energetically constrained by the need to avoid high energy A|A stacking faults along the biaxial stress direction [37], [78]. However, the Schmid factor (m) of the resolved shear stress (τ_R) of the 30º partial is ½ that of the 90º partial, which significantly increases the dislocation nucleation energy if the 30º partial leads. The resolved shear stress relationship is given by $\tau_R(b_{30}) = \frac{1}{2}\tau_R(b_{90})$ and $\tau = m\sigma = cos\ cos\ (\phi)\ cos(\lambda)\sigma$, where σ is the applied stress, ϕ is the angle between the direction of the applied force and the normal to the slip plane, and λ is the angle between the direction of the applied force and the slip direction. The effect of these energy differences is pronounced (exponential with respect to activation energy), because the rate of dislocation nucleation is an Arrhenius function [37], [80]. For tensile strain on the (100) plane and compressive strain on the (111) plane, plastic strain relief via a 90º partial dislocation is favored, which nucleates quickly due its high τ_R (***Figure 1.19(b)***) [37], [78]. A stacking fault ribbon forms above the leading 90º partial, not closing until additional ML coverage provides sufficient stress for a 30º partial to complete a full dislocation (***Figure 1.17(b)***) [37], [78]. This surface-strain relationship is why partial dislocations are so common in these growths [37], [79]. In contrast, compressive strain on (100) and tensile strain on (111) lead with a 30º partial, (***Figure 1.19(c)***) energetically limiting dislocations in favor of elastic strain relief by QD formation [37], [55], [78].

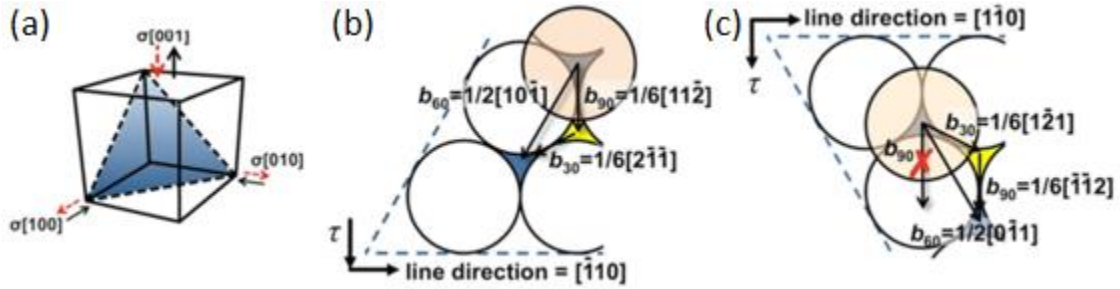

Figure 1.19: (a) Biaxial strain hydrostatically resolves as uniaxial stress, similar to the Poisson effect. (b), (c) Thompson tetrahedral rotation operations show interchanging surface orientation and force vectors are equivalent. A compressively strained (111) surface leads with a low energy 90º partial, causing stacking faults (b). A tensile-strained (111)-surface leads with a high energy 30º partial, favoring dislocation-free strain relaxation by QD self-assembly (c). Reproduced from P. J. Simmonds and M. L. Lee, "Tensile-strained growth on low-index GaAs," J. Appl. Phys., vol. 112, p. 054313, 2012., with the permission of AIP Publishing [37].

Dislocation formation often forms the boundaries to a growth parameter phase-space. Understanding dislocations provides a better fundamental understanding of TSQD growth and could reveal insights to extending these boundaries.

Tensile strain is not only essential for the growth of dislocation-free QDs on (111) surfaces, but opens several new possibilities for research:

1) Single-step QD growth on the (111)-surface is useful for novel optoelectronic devices due to its other distinct surface characteristics such as close-packing and three-fold symmetry.
2) The tensile strain effect of reducing semiconductor band gaps below bulk values provides the ability to tune emission/absorption to longer wavelengths of light. This is necessary to work in common fiber-optic ranges (1260-1675 nm, optimally in the conventional band of 1530-1565 nm) and opens possibilities for devices such as IR detectors. This contrasts with compressive strain, which

increases band gap, making it difficult to hit fiber-compatible emission unless you start from materials with extremely low band gaps.

3) Tensile strain occurs when the buffer-QD material combination of conventionally used compressive strain is inverted, which therefore doubles the number of materials systems available for MBE QD growth.

4) TSQDs form on the (111) surface for emission of low FSS entangled photons.

Having confirmed TSQDs could be grown by MBE on the (111) surface, the promise of low FSS remained to be explored. Confirming this required the synthesis of TSQDs with optically active, direct band gaps [38].

Using GaAs/InAlAs on an InP(111)A substrate, Simmonds then grew symmetric TSQDs with a direct, type-I band gap that emitted from 1.18-1.28 eV (970-1050 nm) (***Figure 1.20(a)***) [38]. Increasing GaAs ML thickness decreases emission energy due to quantum size effects, while the tensile strain significantly reduces these values from the bulk GaAs band gap of 1.42 eV (***Figure 1.20(b)***) [38].

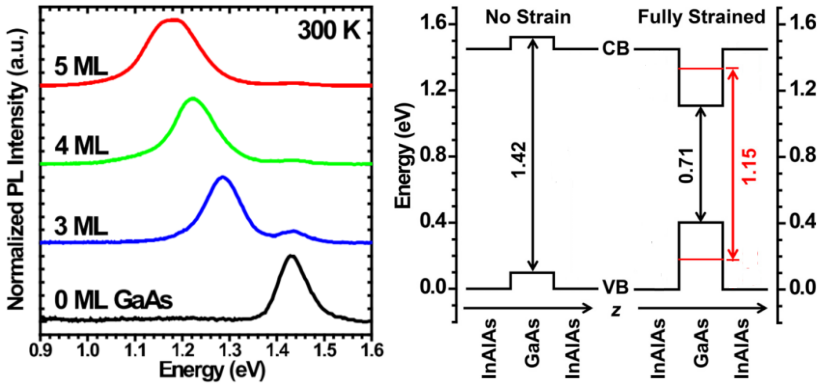

Figure 1.20: GaAs(111) TSQD emission. (a) Room-temperature PL at different GaAs(111)A ML coverages. PL peak wavelength increases with smaller deposition due to quantum confinement effects of smaller TSQDs. (b) Band-diagrams of unstrained and 3.8% tensile-strained GaAs, with the calculated ground state (red) for 4 ML GaAs(111)B coverage. Unstrained GaAs has a significantly higher band gap of 1.42 eV (a,b). Image (a) reprinted from [38], image (b) reprinted from [83].

As expected for the predicted piezoelectric field symmetry, a low median FSS of 7.3±1.2 μeV was measured for these TSQDs (***Figure 1.21***) [38]. For the first time, highly-symmetric, dislocation-free TSQDs with tunably reducible band gaps and low FSS were realized in a single high-purity growth step without pre-patterning.

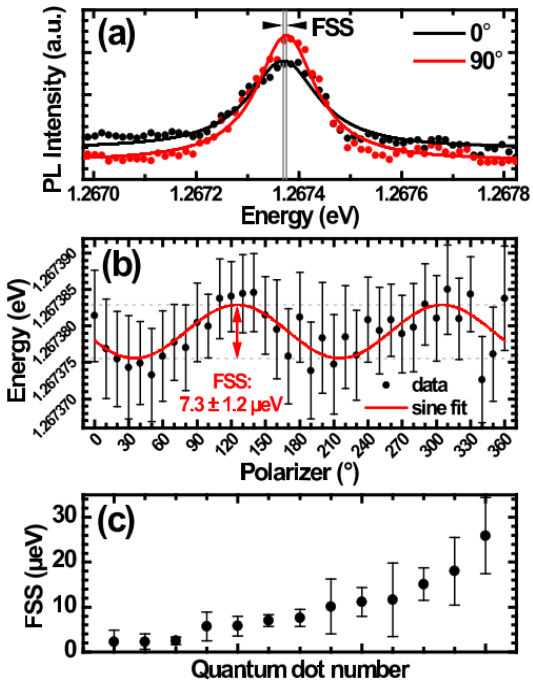

Figure 1.21: GaAs(111)A TSQDs with low FSS. (a) Polarization-resolved μPL fit to a Lorentzian profile. Spectral diffusion broadens the peak, but peak position still indicated the degree of FSS. (b) Peak position values as in (a) versus polarization angle provide the FSS energy range. A sinusoidal fit aids in determining FSS. (c) FSS splitting values as in (b) for 13 TSQDs. Images reprinted from [38].

1.2.8 (111) Surface Tensile-strained Quantum Dots (This Dissertation)

The work I present in the following chapters of this dissertation builds on those preliminary studies of GaAs(111)A TSQD growth. I explore a wide range of GaAs(111)A TSQD growth parameters, including deposition amount (ML), growth rate (ML/s), GaAs substrate temperature (°C), V/III ratio (As_4/Ga), and arsenic species (As_2 versus As_4) (***Figure 1.22***). All TSQD are grown in the same bulk structure (details available in Section 2.2).

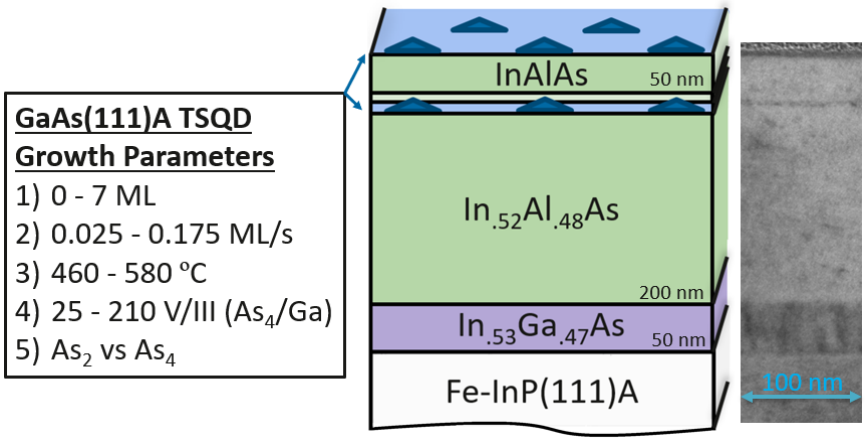

Figure 1.22: Schematic of the structure for all GaAs(111)A TSQD growths in this dissertation, confirmed by X-TEM to the right. For TSQD sample series, single growth parameters in the left box are varied while all others are held constant (occasionally for design-of-experiments more than one parameter is varied (Section 5.1)).

I explore the tuning and optimization of TSQD structural and optical properties across their wide growth parameter phase-space in Chapter 2, additional characterization and analysis of the GaAs(111)A WL and TSQDs in Chapter 3 and the effects different arsenic species in Chapter 4.

References

[1] P. Kok, K. Nemoto, T. C. Ralph, J. P. Dowling, and G. J. Milburn, "Linear optical quantum computing with photonic qubits," *Rev. Mod. Phys.*, vol. 79, pp. 135–174, 2007.

[2] T. D. Ladd, F. Jelezko, R. Laflamme, Y. Nakamura, C. Monroe, and J. L. O'Brien, "Quantum computers.," *Nature*, vol. 464, pp. 45–53, 2010.

[3] International Technology Roadmap for Semiconductors 2.0, "More Moore," 2015.

[4] R. M. Stevenson, R. J. Young, P. Atkinson, K. Cooper, D. A. Ritchie, and A. J. Shields, "A semiconductor source of triggered entangled photon pairs," *Nature*, vol. 439, no. 7073, pp. 179–182, Jan. 2006.

[5] N. Akopian *et al.*, “Correlated and entangled pairs of single photons from semiconductor quantum dots,” *J. Appl. Phys.*, vol. 101, 01712, 2007.

[6] M. Scheibner, S. E. Economou, A. S. Bracker, D. Gammon, and I. V. Ponomarev, “Entangled photon pair generation with quantum dot molecules,” *J. Opt. Soc. Am. B*, vol. 29, no. 2, pp. A82–A85, 2012.

[7] M. A. Pooley *et al.*, “Controlled-NOT gate operating with single photons,” *Appl. Phys. Lett.*, vol. 100, 211103, 2012.

[8] Y.-M. He *et al.*, “On-demand semiconductor single-photon source with near-unity indistinguishability,” *Nat. Nanotechnol.*, vol. 8, pp. 213–217, 2013.

[9] R. Rangarajan, L. E. Vicent, A. B. U’Ren, and P. G. Kwiat, “Engineering an ideal indistinguishable photon-pair source for optical quantum information processing,” *J. Mod. Opt.*, vol. 58, no. 3–4, pp. 318–327, 2011.

[10] N. Dickson *et al.*, “Thermally assisted quantum annealing of a 16-qubit problem.,” *Nat. Commun.*, vol. 4, no. 1903, pp. 1–6, 2013.

[11] T. Lanting *et al.*, “Entanglement in a quantum annealing processor,” *Phys. Rev. X*, vol. 4, 021041, 2014.

[12] J. K. Thompson, J. Simon, H. Loh, and V. Vuletić, “A high-brightness source of narrowband, identical-photon pairs,” *Science*, vol. 313, no. 5783, p. 74, 2006.

[13] D. Salart, A. Baas, C. Branciard, N. Gisin, and H. Zbinden, “Testing the speed of ‘spooky action at a distance’.,” *Nature*, vol. 454, no. 7206, pp. 861–864, 2008.

[14] C. Clausen *et al.*, “Quantum storage of photonic entanglement in a crystal.,” *Nature*, vol. 469, pp. 508–511, 2011.

[15] A. D. Córcoles *et al.*, “Demonstration of a quantum error detection code using a square lattice of four superconducting qubits.,” *Nat. Commun.*, vol. 6, no. 6979, 2015.

[16] M. H. Devoret and R. J. Schoelkopf, “Superconducting circuits for quantum information: an outlook.,” *Science*, vol. 339, no. 6124, pp. 1169–1174, 2013.

[17] B. E. Kane, “A silicon-based nuclear spin quantum computer,” *Nature*, vol. 393, no. 6681, pp. 133–137, 1998.

[18] H. Mooij, “Superconducting quantum bits,” *Phys. World*, vol. 17, no. 12, pp. 29–33, 2004.

[19] J. J. Pla *et al.*, “High-fidelity readout and control of a nuclear spin qubit in silicon,” *Nature*, vol. 496, pp. 334–338, 2013.

[20] T. Takebe, M. Fujii, T. Yamamoto, K. Fujita, and T. Watanabe, “Orientation-dependent Ga surface diffusion in molecular beam epitaxy of GaAs on GaAs patterned substrates,” *J. Appl. Phys.*, vol. 81, no. 11, pp. 7273–7281, 1997.

[21] L. Grossman, “The Quantum Quest for a Revolutionary Computer,” *Time*, vol. 183, no. 6, 2014.

[22] A. J. Shields, “Semiconductor quantum light sources,” *Nat. Photonics*, vol. 1, no. 4, pp. 215–223, Apr. 2007.

[23] D. Bouwmeester, J.-W. Pan, K. Mattle, M. Eibl, H. Weinfurter, and A. Zeilinger, “Experimental Quantum Teleportation,” *Nature*, vol. 390, pp. 575–579, 1997.

[24] A. Gilchrist, K. J. Resch, and A. G. White, “Quantum information: source of triggered entangled photon pairs?,” *Nature*, vol. 445, 05546, 2007.

[25] N. Akopian *et al.*, “Entangled photon pairs from semiconductor quantum dots,” *Phys. Rev. Lett.*, vol. 96, no. 13, pp. 7–10, 2006.

[26] R. Hafenbrak, S. M. Ulrich, P. Michler, L. Wang, A. Rastelli, and O. G. Schmidt, “Triggered polarization-entangled photon pairs from a single quantum dot up to 30 K,” *New J. Phys.*, vol. 9, no. 315, 2007.

[27] A. Dousse *et al.*, “Ultrabright source of entangled photon pairs,” *Nature*, vol. 466, no. 7303, pp. 217–220, 2010.

[28] L. Quiroga and N. F. Johnson, “Entangled Bell and Greenberger-Horne-Zeilinger States of Excitons in Coupled Quantum Dots,” *Phys. Rev. Lett.*, vol. 83, no. 11, pp. 2270–2273, 1999.

[29] J. R. Petta *et al.*, "Coherent Manipulation of Coupled Electron Spins in Semiconductor Quantum Dots," *Science*, vol. 309, pp. 2180–2184, 2005.

[30] D. Kim, S. G. Carter, A. Greilich, A. S. Bracker, and D. Gammon, "Ultrafast optical control of entanglement between two quantum-dot spins," *Nat. Phys.*, vol. 7, no. 3, pp. 223–229, 2011.

[31] A. Boyer De La Giroday, N. Sköld, I. Farrer, D. A. Ritchie, and A. J. Shields, "Excitonic couplings and Stark effect in individual quantum dot molecules," *J. Appl. Phys.*, vol. 110, 083511, 2011.

[32] D. Gammon, E. S. Snow, B. V. Shanabrook, D. S. Katzer, and D. Park, "Fine structure splitting in the optical spectra of single GaAs quantum dots.," *Phys. Rev. Lett.*, vol. 76, no. 16, pp. 3005–3008, 1996.

[33] C. Santori, D. Fattal, M. Pelton, G. S. Solomon, and Y. Yamamoto, "Polarization-Correlated Photon Pairs from a Single Quantum Dot," *Phys. Rev. B*, vol. 66, 045308, 2002.

[34] A. Schliwa, M. Winkelnkemper, A. Lochmann, E. Stock, and D. Bimberg, "In(Ga)As/GaAs quantum dots grown on a (111) surface as ideal sources of entangled photon pairs," *Phys. Rev. B*, vol. 80, no. 16, 161307, 2009.

[35] M. Scheibner *et al.*, "Optically mapping the electronic structure of coupled quantum dots," *Nat. Phys.*, vol. 4, pp. 291–295, 2008.

[36] P. J. Simmonds and M. L. Lee, "Self-assembly on (111)-oriented III-V surfaces," *Appl. Phys. Lett.*, vol. 99, 123111, 2011.

[37] P. J. Simmonds and M. L. Lee, "Tensile-strained growth on low-index GaAs," *J. Appl. Phys.*, vol. 112, 054313, 2012.

[38] C. D. Yerino *et al.*, "Strain-driven growth of GaAs(111) quantum dots with low fine structure splitting," *Appl. Phys. Lett.*, vol. 105, 251901, 2014.

[39] M. D. Eisaman, J. Fan, A. Migdall, and S. V. Polyakov, "Single-photon sources and detectors (review article)," *Rev. Sci. Instrum.*, vol. 82, 071101, 2011.

[40] M. El Kurdi, G. Fishman, Ś. Sauvage, and P. Boucaud, "Band structure and optical gain of tensile-strained germanium based on a 30 band kp formalism," *J. Appl. Phys.*, vol. 107, 013710, 2010.

[41] A. R. Barron, "Chemistry of Electronic Materials," *Rice Univ. course CHEM-496 Chem. Electron. Mater.*, Chapter 6.1: Molecular Beam Epitaxy, 2009.

[42] A. Y. Cho, "Growth of III-V semiconductors by molecular beam epitaxy and their properties," *Thin Solid Films*, vol. 100, no. 4, pp. 291–317, 1983.

[43] S. Niu *et al.*, "Brief Review of Epitaxy and Emission Properties of GaSb and Related Semiconductors," *Crystals*, vol. 7, no. 337, 110337, 2017.

[44] R. Averbeck, H. Riechert, H. Schlötterer, and G. Weimann, "Oxide desorption from InP under stabilizing pressures of P2 or As4," *Appl. Phys. Lett.*, vol. 59, no. 14, pp. 1732–1734, 1991.

[45] V. P. LaBella, D. W. Bullock, C. Emery, Z. Ding, and P. M. Thibado, "Enabling electron diffraction as a tool for determining substrate temperature and surface morphology," *Appl. Phys. Lett.*, vol. 79, no. 19, pp. 3065–3067, 2001.

[46] W. Umrath, Fundamentals of Vacuum Technology. 2007.

[47] S. Montanari, "Fabrication and characterization of planar Gunn diodes for monolithic microwave integrated circuits," PhD Thesis, Aachen RWTHI, 2005.

[48] C. T. Foxon, "Three decades of molecular beam epitaxy," *J. Cryst. Growth*, vol. 251, pp. 1–8, 2003.

[49] A. Madhukar, Q. Xie, P. Chen, and A. Konkar, "Nature of strained InAs three-dimensional island formation and distribution on GaAs(100)," *Appl. Phys. Lett.*, vol. 64, no. 20, pp. 2727–2729, 1994.

[50] D. R. Lide, "CRC Handbook of Chemistry and Physics, 84th Edition, 2003-2004," *Handb. Chem. Phys.*, vol. 53, p. 2616, 2003.

[51] "JSmol: an open-source HTML5 viewer for chemical structures in 3D. http://wiki.jmol.org/index.php/JSmol." .

[52] J. W. Cahn and R. E. Hanneman, “(111) Surface tensions of III–V compounds and their relationship to spontaneous bending of thin crystals,” *Surf. Sci.*, vol. 1, pp. 387–398, 1964.

[53] B. A. Joyce and D. D. Vvedensky, “Self-organized growth on GaAs surfaces,” *Mater. Sci. Eng. R*, vol. 46, pp. 127–176, 2004.

[54] M. Ohring, *The Materials Science of Thin Films*. Hoboken, New Jersey: Academic Press, 1992.

[55] D. J. Eaglesham and M. Cerullo, “Dislocation-free Stranski-Krastanow growth of Ge on Si (100),” *Physical Review Letters*, vol. 64, no. 16. pp. 1943–1946, 1990.

[56] X. L. Li, C. X. Wang, and G. W. Yang, “Thermodynamic theory of growth of nanostructures,” *Prog. Mater. Sci.*, vol. 64, pp. 121–199, 2014.

[57] A.-L. Barabási, “Thermodynamic and kinetic mechanisms in self-assembled quantum dot formation,” *Mater. Sci. Eng. B*, vol. B67, pp. 23–30, 1999.

[58] D. Leonard, M. Krishnamurthy, C. M. Reaves, S. P. Denbaars, and P. M. Petroff, “Direct formation of quantum-sized dots from uniform coherent islands of InGaAs on GaAs surfaces,” *Appl. Phys. Lett.*, vol. 63, no. 23, pp. 3203–3205, 1993.

[59] V. Shchukin, E. Scholl, and P. Kratzer, “Thermodynamics and kinetics of quantum dot growth,” in *Semiconductor Nanostructures*, D. Bimberg, Ed. Berlin Heidelberg New York: Springer, 2008, pp. 1–39.

[60] E. Selçuk, "Guided and Deterministic Self Organization of Quantum Dots," PhD Thesis, Technische Universiteit Eindhoven, 2009.

[61] K. Jacobi, “Atomic structure of InAs quantum dots on GaAs (review),” *Prog. Surf. Sci.*, vol. 71, pp. 185–215, 2003.

[62] P. B. Joyce *et al.*, “Effect of growth rate on the size, composition, and optical properties of InAs/GaAs quantum dots grown by molecular-beam epitaxy,” *Phys. Rev. B*, vol. 62, no. 16, pp. 10891–10895, 2000.

[63] H. Dobbs, D. D. Vvedensky, A. Zangwill, J. Johansson, N. Carlsson, and W. Seifert, “Mean-Field Theory of Quantum Dot Formation,” *Phys. Rev. Lett.*, vol. 79, no. 5, pp. 897–900, 1997.

[64] R. Seguin, A. Schliwa, S. Rodt, K. Pötschke, U. W. Pohl, and D. Bimberg, “Quantum-dot size dependence of exciton fine-structure splitting,” *Phys. E*, vol. 32, pp. 101–103, 2006.

[65] R. Seguin *et al.*, “Control of fine-structure splitting and excitonic binding energies in selected individual InAs/GaAs quantum dots,” *Appl. Phys. Lett.*, vol. 89, 263109, 2006.

[66] J. Wang, G.-C. Guo, and L. He, “Theory of strain tuning fine structure splitting in self-assembled InAs/GaAs quantum dots,” *J. Phys. Condens. Matter*, vol. 26, no. 47, 475301, 2014.

[67] G. Juska *et al.*, “Conditions for entangled photon emission from (111) B site-controlled pyramidal quantum dots,” *J. Appl. Phys.*, vol. 117, 134302, 2015.

[68] K. Kowalik *et al.*, “Influence of an in-plane electric field on exciton fine structure in InAs-GaAs self-assembled quantum dots,” *Appl. Phys. Lett.*, vol. 86, no. 4, pp. 4–7, 2005.

[69] M. A. Pooley, A. J. Bennett, I. Farrer, D. A. Ritchie, and A. J. Shields, “Engineering quantum dots for electrical control of the fine structure splitting,” *Appl. Phys. Lett.*, vol. 103, 031105, 2013.

[70] S. M. Thon *et al.*, “Independent electrical tuning of separated quantum dots in coupled photonic crystal cavities,” *Appl. Phys. Lett.*, vol. 99, 161102, 2011.

[71] E. Stock *et al.*, “Single-photon emission from InGaAs quantum dots grown on (111) GaAs,” *Appl. Phys. Lett.*, vol. 96, no. 9, pp. 96–99, 2010.

[72] R. Seguin *et al.*, “Ex-situ control of fine-structure splitting and excitonic binding energies in single InAs/GaAs quantum dots,” *AIP Conf. Proc.*, vol. 893, pp. 919–920, 2007.

[73] D. J. P. Ellis, R. M. Stevenson, R. J. Young, A. J. Shields, P. Atkinson, and D. A. Ritchie, "Control of fine-structure splitting of individual InAs quantum dots by rapid thermal annealing," *Appl. Phys. Lett.*, vol. 90, 011907, 2007.

[74] G. Bester, X. Wu, D. Vanderbilt, and A. Zunger, "Importance of second-order piezoelectric effects in zinc-blende semiconductors," *Phys. Rev. Lett.*, vol. 96, 187602, 2006.

[75] R. J. Warburton, "Single spins in self-assembled quantum dots," *Nat. Mater.*, vol. 12, no. 6, pp. 483–493, 2013.

[76] J. Treu, C. Schneider, A. Huggenberger, T. Braun, S. Reitzenstein, and S. Ho, "Substrate orientation dependent fine structure splitting of symmetric In(Ga)As/GaAs quantum dots," *Appl. Phys. Lett.*, vol. 101, pp. 1–5, 2012.

[77] K. Watanabe, S. Tsukamoto, Y. Gotoh, and N. Koguchi, "Photoluminescence studies of GaAs quantum dots grown by droplet epitaxy," *J. Cryst. Growth*, vol. 227–228, pp. 1073–1077, 2001.

[78] P. M. J. Maree, J. C. Barbour, J. F. van der Veen, K. L. Kavanagh, C. W. T. Bulle-Lieuwma, and M. P. . Viegers, "Generation of misfit dislocations in semiconductors," *J. Appl. Phys.*, vol. 62, no. 11, pp. 4413–4420, 1987.

[79] J. Petruzzello and M. R. Leys, "Effect of the sign of misfit strain on the dislocation structure at interfaces of heteroepitaxial GaAsP films," *Appl. Phys. Lett.*, vol. 53, no. 24, pp. 2414–2416, 1988.

[80] E. A. Fitzgerald, "Dislocations in strained-layer epitaxy: theory, experiment, and applications," *Mater. Sci. Reports*, vol. 7, pp. 87–142, 1991.

[81] L. Dong, J. Schnitker, R. W. Smith, and D. J. Srolovitz, "Stress relaxation and misfit dislocation nucleation in the growth of misfitting films: A molecular dynamics simulation study," *J. Appl. Phys.*, vol. 83, no. 1, p. 217, 1998.

[82] T. Tsuchiya, T. Taniwatari, M. Komori, R. Tsuneta, and H. Kakibayashi, "Comparison of relaxation process of compressive and tensile strains in ingaas lattice-mismatched layers on inp substrates," *Jpn. J. Appl. Phys.*, vol. 33, no. 1R, p. 230, 1994.

[83] C. D. Yerino *et al.*, “Tensile GaAs(111) quantum dashes with tunable luminescence below the bulk band gap,” *Appl. Phys. Lett.*, vol. 105, 071912, 2014.

CHAPTER TWO: SELF-ASSEMBLY OF (111)-ORIENTED TENSILE-STRAINED QUANTUM DOTS BY MOLECULAR BEAM EPITAXY

Christopher F. Schuck[1a)], Robin A. McCown[1], Ashlie Hush[1], Austin Mello[1], Simon Roy[2], Joseph W. Spinuzzi[2], Baolai Liang[3], Diana L. Huffaker[3], Paul J. Simmonds[1,2]

[1]Micron School of Materials Science & Engineering, Boise State University, 1910 University Drive, Boise, ID 83725

[2]Physics Department, Boise State University, 1910 University Drive, Boise, ID 83725

[3]California NanoSystems Institute, University of California, 570 Westwood Plaza, Los Angeles, CA 90095

[a)] Corresponding author: christopherschuck@boisestate.edu

Reproduced from C.F. Schuck, R.A. McCown, A. Hush, A. Mello, S. Roy, J.W. Spinuzzi, and P.J. Simmonds, J. Vac. Sci. Technol. B **36**, 031803 (2018), with the permission of AIP Publishing.

: https://doi.org/10.1116/1.5018002

Abstract

We report on a comprehensive study of the growth of coherently strained GaAs quantum dots (QDs) on (111) surfaces via the Stranski-Krastanov (SK) self-assembly mechanism. Recent reports indicate that the long-standing challenge, whereby the SK growth mechanism could not be used to synthesize QDs on (111) surfaces, or QDs under tensile strain, has been overcome. However, a systematic study of the SK growth of (111)-oriented, tensile-strained QDs (TSQDs) as a function of molecular beam epitaxy growth parameters is still needed. Here, we explore the effects of deposition amount, substrate temperature, growth rate, and V/III flux ratio on the SK-driven self-assembly of GaAs(111)A TSQDs. We highlight aspects of TSQD SK self-assembly on (111) surfaces that appear to differ from the SK growth of traditional compressively strained QDs on (100) surfaces. The unique properties of (111) QDs and tensile-strained QDs mean that they are of interest for various research areas. The results discussed here offer a practical guide for tailoring the size, shape, density, uniformity, and photon emission wavelength and intensity of (111) TSQDs for future applications.

2.1 Introduction

Quantum dots (QDs) are a well-established research area in solid-state optoelectronics [1], [2], their broad utility is limited mainly by the number of materials systems from which they can be synthesized. QDs grown on (111) surfaces, and QDs that form under tensile strain, are predicted to have interesting properties stemming from their fundamental physics [3]–[7]. However, the growth of (111)-oriented, or tensile-strained QDs via the well-established Stranski-Krastanov (SK) mechanism is known to be extremely challenging, due to the rapid relaxation of strain via dislocations [1], [8]–[12].

We recently reported a solution to this problem. SK self-assembly, the (111) orientation, and tensile strain form an interdependent triad. Together they permit the growth of tensile-strained QDs on (111) surfaces [3], [13], [14]. Here we consider these three components in turn.

SK self-assembly: SK self-assembly in solid-state semiconductor media by molecular beam epitaxy (MBE) produces high-purity, dislocation-free QDs with precise control of materials, interfaces, and optoelectronic properties [1], [2], [15], [16], for a wide range of applications [17]–[19]. QD self-assembly via the SK mechanism is often preferred because of its simplicity, single-step nature, scalability, and controllability via well-understood growth parameters.

(111) orientation: QDs grown on low-index planes other than the traditional (100) surface are expected to have unique properties [3], [5]–[7]. The three-fold rotational symmetry of zinc blende (111) surfaces are ideal for integration with materials with similar symmetry such as certain topological insulators and 2D materials [20], [21]. Furthermore, with inherently low fine structure splitting (FSS), QDs grown on a (111) surface are expected to be efficient emitters of polarization entangled photons for quantum optics applications [5], [6], [22]. Unfortunately, compressive strain relaxes rapidly on this surface, producing periodic networks of misfit dislocations [1], [8]–[10]. Without the presence of strain to drive self-assembly, SK growth of (111) QDs is not possible [1], [15], [16]. As a result, researchers have developed techniques to side-step SK self-assembly, such as droplet epitaxy and overgrowth on pre-patterned surfaces [23]–[26]. These techniques bring their own advantages, but can also introduce unwanted defects or require labor-intensive processing steps [23]–[26].

Tensile strain: In traditional QDs, a smaller lattice constant barrier material surrounds a larger lattice constant QD material, generating compressive strain. Tensile-strained self-assembly would allow us to interchange these lattice constant requirements, which in principle doubles the number of material combinations available for QD self-assembly. Tensile strain also reduces the electronic band gap, in contrast with the increase in band gap caused by both compressive strain and quantum confinement [3], [27], [28], providing exceptionally tunable photonic properties. Promising applications for tensile-strained QDs could therefore include infrared optoelectronics, semiconductor-to-semimetal conversion for high-conductivity tunnel junctions [29], transformation of Ge into a direct band gap semiconductor [4], [30], and strain-enhanced thermoelectrics [31]. Inducing tensile strain in QD materials can be challenging, with defects generated at low strains, and the need for complex post-growth processing [32], [33]. An attractive alternative would be to create highly localized nanoscale regions of tensile strain in a single step, just like the compressive strain fields surrounding traditional QDs [34].

Bringing these three components together, we recently demonstrated that the SK self-assembly of tensile-strained QDs is in fact possible, as long as we also change the surface orientation from (100) to (111), or (110) [3], [13], [14], [27], [34]. The resulting tensile strain-driven self-assembly process is entirely analogous to the mechanism by which QD form under compressive strain on (100) surfaces [13], [27]. In both compressively strained (100) QDs and tensile-strained (111) QDs, atomic arrangement and strain direction interact to favor the formation of dislocation-free QDs [11]–[14], [35]. Although these initial experiments served to confirm many of the expected benefits from the SK self-assembly of (111)-oriented TSQDs, to date there has been no

comprehensive study of their growth. To exploit their full potential, it is critical that we fully understand how to tailor their unique properties. To this end, this paper describes a systematic analysis of TSQD growth.

2.2 Experimental Setup and Methodology

We grew several series of samples using solid-source MBE. Each series represents a variation in the growth parameters for TSQD formation. We determine deposition thickness, in MLs, and growth rate, in MLs per second, using in-situ reflection high-energy electron diffraction (RHEED) intensity oscillations on the (100) surface, correcting for the differences in areal density and interplanar spacing of the (111) surface. We determine substrate growth temperature, T_{SUB}, using a pyrometer and a substrate-mounted thermocouple that we calibrate using RHEED to observe known phase transitions in sample surface reconstructions. We infer growth fluxes for V/III ratios from the beam equivalent pressure (BEP) measured with a beam flux monitor in front of the substrate heater. Our group V species is As_4 rather than As_2, for consistency with historical research on the (111) surface before As crackers were widely available. We use ex-situ single crystal x-ray diffraction (XRD) to calibrate $In_{0.52}Al_{0.48}As$ and $In_{0.53}Ga_{0.47}As$ compositions for lattice-matching to the nominally on-axis InP(111)A substrates.

We measure TSQD shape, size, and areal density with atomic force microscopy (AFM). To calculate TSQD volume, we model them as tetrahedra with an equilateral triangle base, using in-plane and height dimensions taken from our AFM measurements. We measure TSQD emission wavelength and intensity profiles using low-temperature (7 K) photoluminescence (PL). Since the thickness and composition of the InAlAs buffer is nominally identical in all samples, we normalize our PL spectra to the intensity of the

InAlAs emission peak. This allows us to compare TSQD peak PL intensity (the highest intensity emission at a single QD emission wavelength) across samples. Peak PL intensity is useful for determining the efficiency of QDs emitting at the most common wavelength. However, when PL intensity is lower, simply measuring peak intensity does not allow one to distinguish between broadening of the TSQD size distribution (i.e. fewer TSQDs emitting at the peak wavelength), or reduced TSQD crystal quality due to dislocations (i.e. fewer optically active TSQDs emitting at all wavelengths including at the peak). Plotting total PL emission (integrated area of TSQD spectral features) versus QD areal density allows us to make this distinction by providing an indication of PL emission efficiency (the relative percentage of QDs that emit light, normalized to the highest value obtained) and, therefore, QD crystal quality.

Our samples consist of GaAs TSQDs grown within $In_{0.52}Al_{0.48}As$ barriers, generating 3.8% tensile strain in the GaAs. The wider band gap of the InAlAs creates type-I confinement of charge carriers to create optically active GaAs TSQDs [3], [27]. Each sample contains both buried and surface TSQDs for optical and structural analysis, respectively. We mount the InP substrates on molybdenum blocks using indium solder. We grow 50 nm of lattice-matched InGaAs between the InP substrate and the bottom InAlAs barrier (T_{SUB}: 510 °C, growth rate: 169 nm/hr, and V/III ratio: 160) for a smoother InAlAs morphology [7]. The bottom InAlAs barrier in all samples is 200 nm thick (T_{SUB}: 510 °C, growth rate: 172 nm/hr, and V/III ratio: 160) to minimize surface roughness [7]. The 50 nm InAlAs top barrier is grown in two steps. First, we deposit 10 nm InAlAs at the TSQD growth temperature (growth rate: 172 nm/hr, and V/III ratio: 160), to prevent annealing or degradation of the TSQDs, followed by 40 nm InAlAs

grown at T_{SUB}: 510 °C (growth rate: 172 nm/hr, and V/III ratio: 160). Consistent with previous reports [27], during TSQD formation we see no change in the RHEED pattern from the streaky (2 × 2) surface reconstruction of the (111) surface. We attribute the lack of a "spotty" RHEED pattern to the very low areal densities and low height profiles of the GaAs/InAlAs(111)A TSQDs.

Our control for these experiments consists of a sample containing 3.5 ML GaAs TSQDs grown under the following conditions: T_{SUB}: 485 °C, GaAs growth rate: 0.075 ML/s, and As_4/Ga BEP ratio: 75. This control sample is based on previous GaAs(111)A TSQD growth parameters, and serves as a comparison as we vary these growth parameters. In each sample series, we adjust a single growth parameter: GaAs deposition thickness: 0 – 4.5 ML, T_{SUB}: 460 – 535 °C, GaAs growth rate: 0.025 – 0.125 ML/s, and As_4/Ga BEP ratio: 50 – 110.

2.3 Results and Discussion

We analyze AFM images taken at multiple positions on each sample to determine TSQD areal density (cm^{-2}), and average height (nm), diameter (nm), and volume (nm^3). The PL emission wavelengths and intensities we report below come from the highest intensity TSQD peak in each PL spectrum. To explore the effect of MBE growth conditions on TSQD crystal quality, we compare the width of each TSQD size distribution with its corresponding PL emission intensity profile.

2.3.1 Deposition Amount Series

Deposition of < 2.5 ML GaAs on InAlAs(111)A, creates a 2D wetting layer that consists of rounded "hills" with ML-high contours (root mean squared (RMS) surface roughness of 0.54 nm) (***Figure 2.1(a)***).

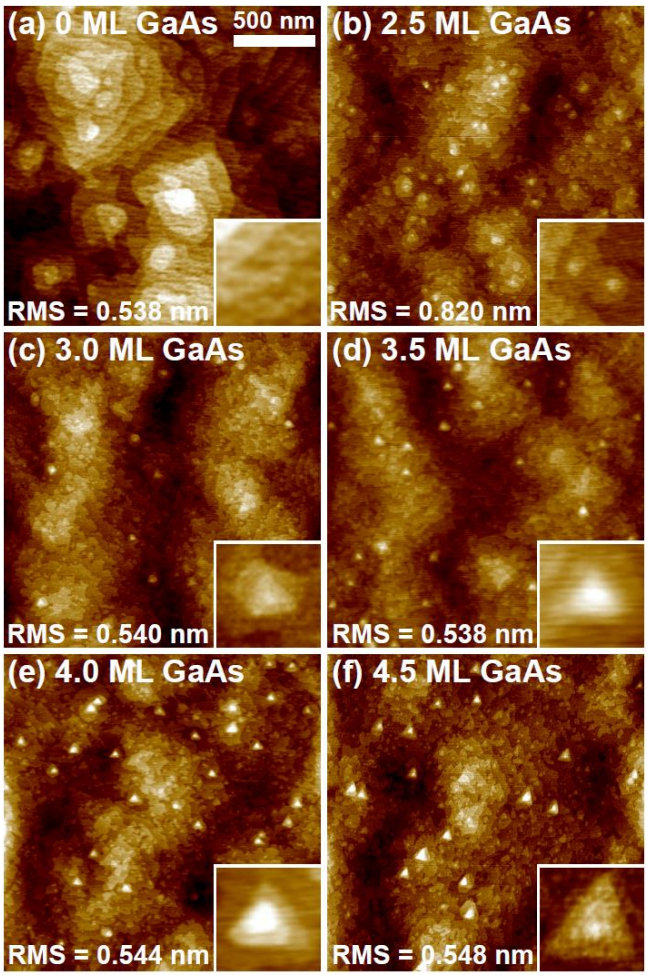

Figure 2.1: 2 x 2 μm^2 AFM images with increasing deposition amount: (a) 0 ML, (b) 2.5 ML, (c) 3.0 ML, (d) 3.5 ML, (e) 4.0 ML, (f) 4.5 ML. Insets are 200 nm^2 (a) and (b), and 100 nm^2 (c)-(f). Proto-TSQDs nucleate by 2.5 ML, then from 3–4 ML, both size and areal density of the triangular TSQDs increases. By 4.5 ML TSQD size continues to increase, while areal density begins to decrease.

At 2.5 ML, the wetting layer surface becomes rougher (RMS = 0.82 nm). Proto-TSQDs begin to appear that are 1 ML in height (0.33 nm) and 30 – 50 nm in diameter. These proto-TSQDs nucleate preferentially around the edges of the contoured hills where step-edge density is highest (***Figure 2.1(b)***). We have seen clustering of TSQDs at step edges in other low-index non-(100) growths [34], and attribute this effect to longer adatom diffusion lengths compared to the (100) surface [13], as well as the enhanced

accumulation of material at step edges due to the presence of a Schwoebel barrier (the potential energy diffusion barrier to adatom migration located at step-edges) [36], [37].

At 3.0 ML, triangular GaAs TSQDs appear, demarcating the completion of the SK transition from 2D to 3D growth ***Figure 2.1(c)***). As we increase GaAs deposition from 3.0–4.5 ML, the TSQDs grow monotonically in average height, diameter, and volume (***Figure 2.1(c-f)***) (***Table 2.1***). The only significant change in RMS roughness across this series occurs at 2.5 ML, corresponding to the onset of TSQD nucleation. TSQD volume increases linearly with deposition amount, consistent with the SK growth mode (***Table 2.1***).

Table 2.1: Deposition amount series characterization statistics (T_{SUB}, growth rate, and V/III ratio held constant (see Section 2.2)). TSQD height, diameter, and volume average (with standard deviations), and areal density, are determined from AFM images. Peak PL wavelength and intensity are taken as the highest TSQD emission peak, with the intensity of each spectrum normalized to the nominally consistent PL peak from the InAlAs barriers. Total PL emission is taken as the integrated area under the TSQD PL emission curve. Emission efficiency is the ratio of total PL emission and areal density, normalized to the highest emission efficiency obtained.

	3.0 ML	3.5 ML	4.0 ML	4.5 ML
Height (nm)	0.85 ± 0.18	0.96 ± 0.23	1.23 ± 0.24	1.21 ± 0.29
Diameter (nm)	44 ± 10	46 ± 11	46 ± 10	53 ± 11
Volume (nm^3)	347 ± 188	419 ± 224	531 ± 280	675 ± 307
Areal Density (cm^{-2})	2.8×10^8	5.9×10^8	9.3×10^8	5.6×10^8
Peak PL Wavelength (nm)	961	992	1015	1047
Peak PL Intensity (a.u.)	0.84	1.05	1.37	0.82
Total PL Emission (a.u.)	57.5	83.6	117.4	81.2
Emission Efficiency (a.u.)	23.9	16.6	14.4	16.7

TSQD height, diameter, volume, and peak PL wavelength all increase with higher deposition amount. TSQD areal density and total PL emission both increase until 4 ML, then decrease at 4.5 ML, resulting in little variation in emission efficiency. These PL

results are consistent with quantum confinement effects and sustained crystal quality with increasing deposition amount.

TSQD height and volume distributions broaden with increasing deposition amount (***Table 2.1***). We attribute this broadening to the appearance of a bimodal TSQD size distribution as the result of Ostwald ripening. A secondary population of TSQDs forms with volume > 850 nm^3 (***Figure 2.2***). For the 4.0 ML and 4.5 ML samples, this secondary population of larger TSQDs represents a significant proportion of the total TSQD population (2% at 3 ML, 4% at 3.5 ML, 13% at 4 ML, and 26% at 4.5 ML). TSQD areal densities are two orders of magnitude lower (~10^8 cm^{-2}) than typically seen in compressively strained (100)-QDs (~10^{10} cm^{-2}).[38], [39] TSQD areal density increases monotonically until 4.0 ML, then decreases at 4.5 ML, providing additional evidence for the onset of Ostwald ripening.

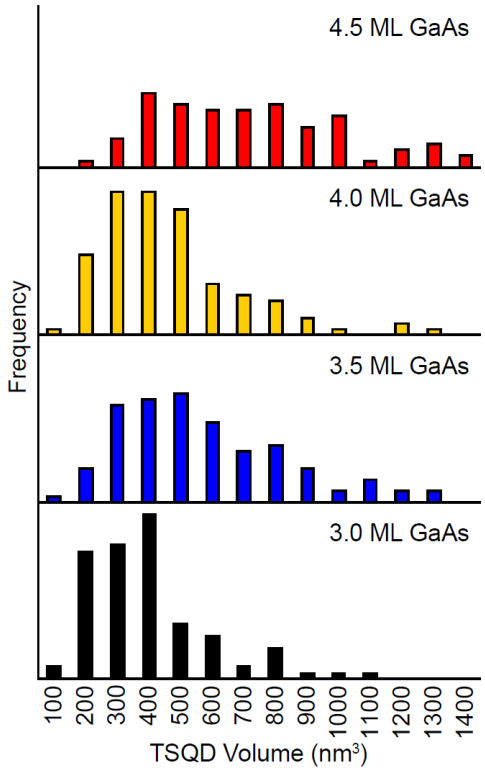

Figure 2.2: Average TSQD volume histogram with increasing deposition amount. Average TSQD volume from 3.0 to 4.5 ML deposition has a consistent peak from 300 - 500 nm^3. With increasing deposition amount, a secondary population of > 800 nm^3 volume TSQDs becomes more apparent. By 4.0 ML and 4.5 ML, this larger secondary population represents a significant portion of the TSQDs.

PL from the GaAs TSQDs is significantly red-shifted compared to the emission at 816 nm we measure for unstrained bulk GaAs at 7K (black dashed line in ***Figure 2.3(a)***), confirming that the tensile strain has reduced the TSQD band gap. The PL wavelength increases as the TSQDs get larger, due to the reduction of the confined ground state energy. Across this series, TSQD PL wavelength is linearly tunable from 961 nm to 1047 nm by increasing the GaAs deposition amount. This wavelength increase corresponds to a reduction in the TSQD ground state transition energy from 1.29 eV to 1.18 eV. This PL red-shift correlates with increasing TSQD volume, confirming that it arises from quantum size effects (***Figure 2.3(b)***).

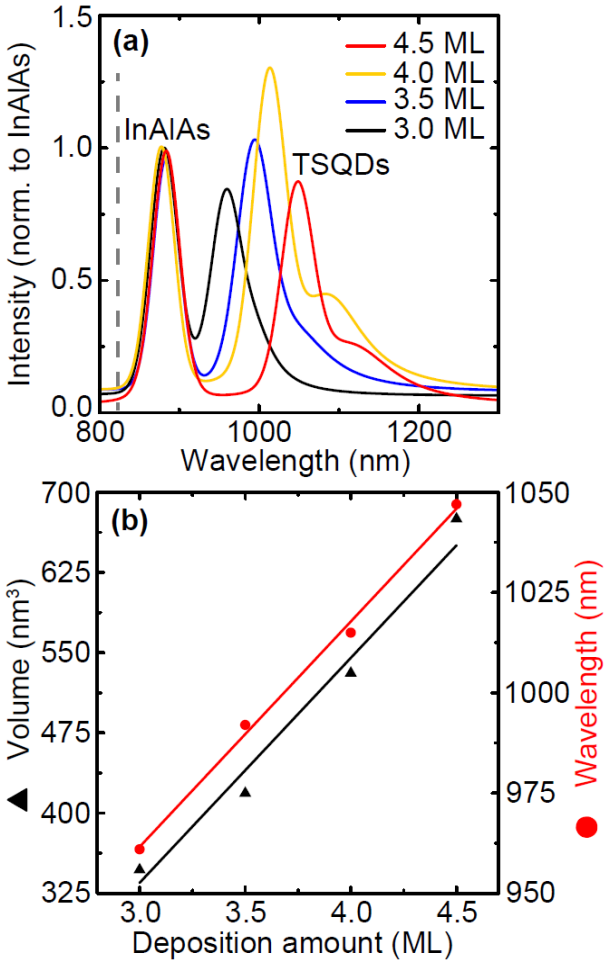

Figure 2.3: (a) PL emission spectra as a function of GaAs deposition amount in ML. Black dashed line shows 7K PL emission of unstrained bulk GaAs for comparison. Peak TSQD PL wavelength increases with higher deposition amount up to 4.0ML, then decreases at 4.5 ML. By 3.5 ML a background of longer wavelength emission is apparent, which resolves into a secondary peak for 4.0 ML and 4.5 ML deposition. Spectral intensities are normalized to the bulk InAlAs PL peak. (b) TSQD volume and peak PL wavelength as a function of GaAs deposition amount. TSQD volume and PL wavelength both increase linearly with increasing deposition amount.

PL emission intensity increases in this series for 3.0 – 4.0 ML TSQDs, then decreases at 4.5 ML. A longer-wavelength shoulder on the TSQD peak appears at 3.5 ML, which develops into a secondary, longer-wavelength peak in the 4.0 and 4.5 ML sample spectra. This additional spectral feature corresponds to emission from a population of larger TSQDs, confirming the bimodal evolution of TSQD size we observed with AFM analysis.

In the 3.0 – 4.0 ML range, peak PL intensity increases linearly with TSQD areal density. At 4.5 ML, both peak PL intensity and TSQD density decrease, although the decrease in peak PL intensity is disproportionately large. To rule out dislocation nucleation in large Ostwald-ripened QDs as the cause of this reduction in PL intensity, we performed plan-view transmission electron microscopy (TEM) (not shown here). We found no evidence of dislocations in the 4.5 ML TSQDs, a result that is consistent with previous analysis of TSQDs with TEM [3, 14]. This finding is supported by the relatively constant PL emission efficiency with increasing deposition amount (***Table 2.1***), again suggesting no deterioration in crystal quality for the 4.5 ML sample.

2.3.2 Substrate Temperature (T_{SUB}) Series

As we increase T_{SUB} for the growth of 3.5 ML GaAs TSQDs, we initially see a decrease in TSQD volume in the range 460 – 485 °C (***Table 2.2***). Kinetic Monte Carlo simulations of kinetic versus thermodynamic control of island nucleation and growth suggest that thermodynamic control could be the cause of this observed decrease in TSQD volume with increasing T_{SUB} [40]. However, at higher T_{SUB} in the range 485 – 535 °C, average TSQD volume is essentially constant (***Table 2.2***), varying less than one standard deviation about an average value (437 ± 213 nm^3). This volume saturation in the face of decreasing aspect ratio (see below), perhaps suggests that TSQD volume has reached thermodynamic equilibrium [40].

Table 2.2: Substrate temperature (T_{SUB}) series characterization statistics (deposition amount, growth rate, and V/III ratio held constant (see Section 2.2)). TSQD height, diameter, and volume average (with standard deviations), and areal density, are determined from AFM images. Peak PL wavelength and intensity are taken as the highest TSQD emission peak, with the intensity of each spectrum normalized to the nominally consistent PL peak from the InAlAs barriers. Total PL emission is taken as the integrated area under the TSQD PL emission curve. Emission efficiency is the ratio of total PL emission and areal density, normalized to the highest emission efficiency obtained. TSQD height and volume both decrease from 460 °C to 485 °C. Peak PL wavelength is statistically constant throughout, despite the initial volume decrease. Total PL emission increases monotonically with T_{SUB}, despite TSQD areal density decreasing above 510 °C. Both of these PL phenomena are consistent with improved crystal quality at higher T_{SUB}.

	460 °C	485 °C	510 °C	535 °C
Height (nm)	1.29 ± 0.31	0.96 ± 0.23	0.73 ± 0.20	0.74 ± 0.18
Diameter (nm)	50 ± 10	46 ± 11	54 ± 9	55 ± 8
Volume (nm^3)	633 ± 284	419 ± 224	436 ± 220	456 ± 193
Areal Density (cm^{-2})	5.3×10^8	5.9×10^8	9.6×10^8	4.9×10^8
Peak PL Wavelength (nm)	982	992	974	978
Peak PL Intensity (a.u.)	0.49	1.05	1.96	2.50
Total PL Emission (a.u.)	36.2	83.6	165.6	208.5
Emission Efficiency (a.u.)	7.8	16.3	19.7	48.8

We can change the shape of these 3.5 ML GaAs TSQDs by growing them at higher T_{SUB}. Raising T_{SUB} from 460 – 535 °C reduces the TSQD aspect ratio (height-to-base diameter ratio) from 0.026 to 0.013; their average height decreases while their diameter increases (***Table 2.2***). Similar temperature-dependent flattening has been previously observed during annealing of QDs grown by DE, where the authors attributed the decrease in aspect ratio to increased adatom diffusion lengths at higher T_{SUB} [41].

This behavior for TSQDs is quite different from the growth of traditional compressively strained QDs on (100) surfaces. As T_{SUB} increases, QDs typically increase in volume and decrease in areal density, with any morphological changes occurring along indexed facets [1], [39], [40]. Traditional InAs(100) QDs also tend to have smaller diameters (~25 nm), and larger heights (~5 nm) compared with the (111) TSQDs [1],

[39], [42]. InAs(100) QDs therefore have height-to-base aspect ratios (0.200 ± 0.05) that are an order of magnitude larger than those of the TSQDs in this study (0.020 ± 0.007). That the aspect ratio of TSQDs is so small is primarily the result of their very low heights, consisting as they do of monolayer-high steps that we can resolve in AFM (***Figure 2.1(e)-(f)***). These results suggest TSQDs may not in fact erupt in a rapid 2D-to-3D SK transition, but instead self-assemble via a more gradual coalescence that is more consistent with a simple adatom diffusion model. A smoother 3D transition is perhaps not surprising. Compared to the (100) surface, the (111)A surface has lower surface energy [43], and longer adatom diffusion length [44], [45]. Lower surface energy reduces the barrier between 2D and 3D growth, while higher adatom diffusion increases the accessibility of low energy sites such as step edges and islands.

The fact that we see TSQD areal density increase as we raise T_{SUB} from 460 °C to 510 °C, but then decrease by 535 °C (***Table 2.2***) suggests some dynamic shift in the kinetics or energetics of TSQD formation. This shift results in a sign change in the slope on an Arrhenius plot of the natural logarithm of areal density against $1000/T_{SUB}$, possibly indicating a change from kinetic to thermodynamic control [15], [40], or a crossing of the boundary between SK and Volmer-Weber 3D growth modes [46]. We plan additional experiments to distinguish between these mechanisms.

The PL emission wavelength from the TSQDs does not change systematically with T_{SUB}, suggesting little change in volume with increasing T_{SUB} among TSQDs emitting at the peak wavelength (i.e. TSQDs with the most common size) (***Table 2.2***) (***Figure 2.4(a)***). That being said, the sample grown at 460 °C emits at the same wavelength as the three other samples in this series despite having TSQDs with larger

average volume (***Table 2.2***). It is likely that at this low T_{SUB}, the larger TSQDs form dislocations that inhibit their optical activity. Increasing T_{SUB} to 485 °C more than doubles peak PL emission intensity, while TSQD areal density only increases by 11% (***Table 2.2***). Taken together, these results suggest a dramatic improvement in crystal quality as we raise T_{SUB}. Indeed, peak PL intensity linearly undergoes a five-fold increase as T_{SUB} is raised from 460°C to 535 °C (***Table 2.2***). Plotting areal density against peak PL intensity contrasts the linear increase in intensity with the non-linear variation in areal density (***Figure 2.4(b)***). However, as in the ML series, the TSQD size distribution also narrows as peak PL intensity increases (***Table 2.1***, ***Table 2.2***). Comparing areal density to the total PL emission results in the same non-linearity as for peak PL intensity. PL emission efficiency is essentially constant across the deposition amount series (Section 2.3.1) and growth rate series (Section 2.3.3). For this T_{SUB} series however, PL emission efficiency more than halves (53% reduction) when cooling from 485 °C to 460 °C, and triples (199% increase) when heating from 485 °C to 535 °C. This evidence favors a significant improvement in TSQD crystal quality with T_{SUB}, most likely from a reduction in point defects due to annealing effects at higher temperatures. An enhancement in crystal quality is supported by the fact that we see a slight decrease in surface roughness in AFM as we raise T_{SUB} from 460 °C (RMS = 0.56 nm), to 535 °C (RMS = 0.49 nm).

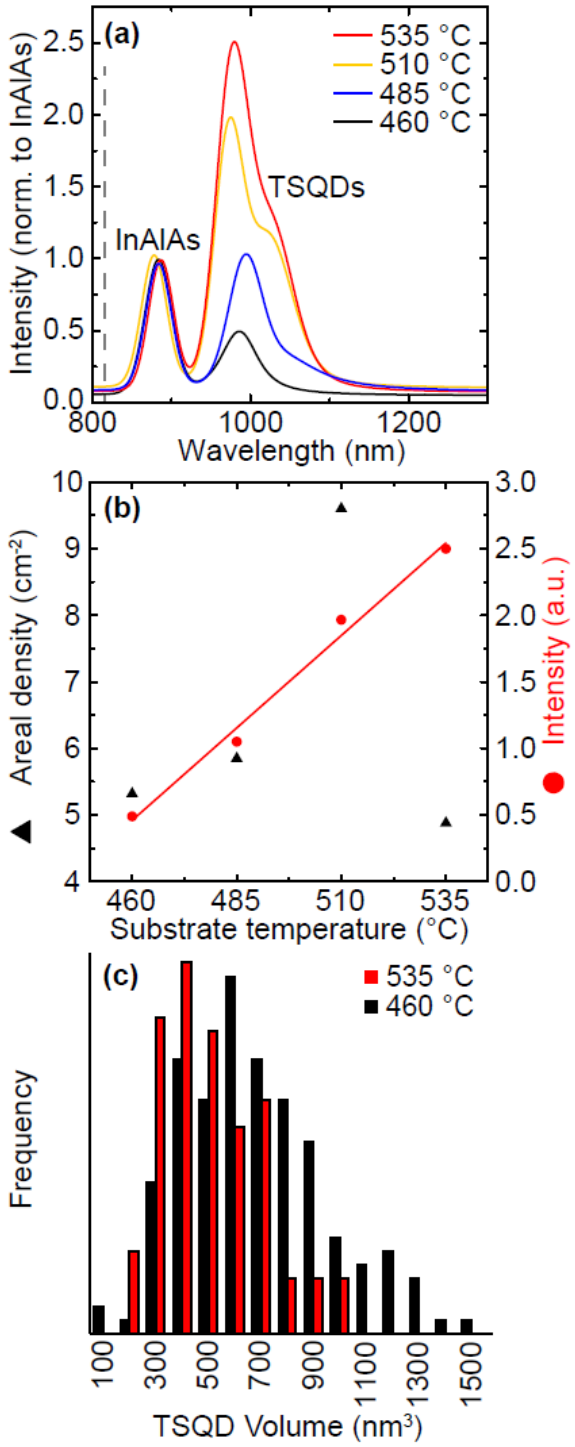

Figure 2.4: (a) TSQD PL emission as a function of T_{SUB}. As we raise T_{SUB}, peak TSQD PL wavelength remains constant, while peak PL intensity increases. (b) TSQD areal density and peak PL intensity as a function of T_{SUB}. Peak PL intensity increases linearly with T_{SUB}, while TSQD areal density increases up to 510 °C, then decreases at higher T_{SUB}. Increased peak PL intensity at 535 °C, despite a reduction in TSQD areal density, suggests an improvement in crystal quality. (c) histograms of TSQD volume for the samples grown at lowest (460 °C) and highest (535 °C) T_{SUB}.

As with the deposition amount series, average TSQD volume is essentially consistent across this series at 300– 600 nm^3 (***Figure 2.4(c)***). However, all samples also exhibit a population of larger TSQDs (800–1100 nm^3) that we believe is responsible for the longer wavelength shoulder peak at ~1050 nm seen in the PL spectra for samples grown at $T_{SUB} \geq 485$ °C (***Figure 2.4(b)***). The fact that this shoulder peak is not seen for the sample grown at 460 °C, indicates that these larger TSQDs are not optically active at low T_{SUB}. However, the appearance and subsequent increase in relative intensity of the shoulder peak as T_{SUB} is raised, suggests that optical quality of these larger QDs also improves at higher T_{SUB}, just as we have concluded for the majority TSQD population.

2.3.3 Growth Rate Series

As we increase the growth rate for 3.5 ML GaAs TSQDs from 0.025 ML/s to 0.075 ML/s, TSQD volume decreases while areal density increases (***Table 2.3***), consistent with trends seen in traditional QD growth [47], [48]. We attribute these trends to the higher population of adatoms on the epitaxial surface per unit time as the growth rate increases, increasing the likelihood that two adatoms meet and nucleate a new island, before they attach to an existing island. However, as we increase GaAs growth rate further, from 0.075 – 0.125 ML/s, average TSQD height, diameter, and volume remain statistically constant (***Table 2.3***). The higher average volume at 0.025 ML/s is due to a secondary population of larger TSQDs (volume ~ 700 nm^3) that exists in addition to the primary population with average volume ~400 nm^3 (***Figure 2.6***). As in the T_{SUB} series, this behavior contrasts with traditional QD formation where we would expect a continued reduction in TSQD size and an increase in areal density with increasing growth rate. At higher growth rates, more adatoms are present on the epitaxial surface at any given time;

as T_{SUB} is raised, adatom mobility is increased. In both cases, the rate of adatom collisions and interactions increases, but it the case of TSQD growth this does not appear to translate into a change in their average volume.

Table 2.3: Growth rate series characterization statistics (deposition amount, T_{SUB}, and V/III ratio held constant (see Section 2.2)). TSQD height, diameter, and volume average (with standard deviations), and areal density, are determined from AFM images. Peak PL wavelength and intensity are taken as the highest TSQD emission peak, with the intensity of each spectrum normalized to the nominally consistent PL peak from the InAlAs barriers. Total PL emission is taken as the integrated area under the TSQD PL emission curve. Emission efficiency is the ratio of total PL emission and areal density, normalized to the highest emission efficiency obtained.

	0.025 ML/s	0.075 ML/s	0.100 ML/s	0.125 ML/s
Height (nm)	0.88 ± 0.23	0.96 ± 0.23	0.71 ± 0.17	0.82 ± 0.20
Diameter (nm)	59 ± 10	46 ± 11	48 ± 9	49 ± 8
Volume (nm^3)	627 ± 301	419 ± 223	341 ± 179	400 ± 182
Areal Density (cm^{-2})	5.2×10^8	5.9×10^8	6.6×10^8	7.6×10^8
Peak PL Wavelength (nm)	990	992	998	1004
Peak PL Intensity (a.u.)	0.86	1.05	1.11	1.35
Total PL Emission (a.u.)	85.6	83.6	98.7	103
Emission Efficiency (a.u.)	18.7	16.3	17.2	15.6

TSQD diameter and volume both decrease from 0.025 ML/s to 0.075 ML/s. At higher growth rates, TSQD height, diameter, and volume are statistically constant. Peak PL wavelength remains constant throughout, despite the initial volume decrease. Despite a disproportionate increase in peak PL intensity compared to areal density, total PL emission increases linearly with TSQD areal density, resulting in little variation in emission efficiency. These AFM and PL results are consistent with broadening of the TSQD size distribution at lower growth rates.

The average TSQD volume (443 ± 248 nm^3) across all four growth rate samples is very close to the average volume (437 ± 213 nm^3) calculated across the three T_{SUB} samples grown at 485 – 535 °C (discussed in Section 2.3.2). In addition, the fact that PL

emission wavelength does not change as we tune growth rate (***Figure 2.5(a)***) or T_{SUB} (***Figure 2.4(a)***) provides further evidence for the TSQDs having reached a constant volume. These observations suggest that the GaAs(111)A TSQDs may be attaining an equilibrium size over the growth parameter ranges studied here. QDs are predicted to reach an equilibrium size as the result of competition between two mechanisms. Larger QDs reduce the total surface area compared to many small QDs, and so are energetically favorable (as in Ostwald ripening). However, larger QDs are surrounded by larger elastic strain fields that eventually promote adatom detachment and escape. The balance between these two mechanisms is predicted to lead to QDs with some equilibrium size [16], [39], [40], [46]. Although QDs with equilibrium size have been widely discussed [1], [40], [46], [49], they are rarely observed in traditional QD materials systems, perhaps as a result of lower adatom migration lengths on (100) surfaces compared to (111)A, and the lower T_{SUB} values required to prevent indium desorption when growing InAs QDs. The fact that we see suggestions of equilibrium island size during tensile-strained self-assembly could lead in the future to TSQDs with exceptionally high size uniformity.

To provide additional experimental support for this theory, we performed annealing experiments on our GaAs(111)A TSQDs. If the TSQDs have already reached equilibrium size during growth, we would not expect significant changes in TSQD volume after annealing. Using our standard MBE conditions, we grew a sample with 4.5 ML TSQDs at T_{SUB} = 522 °C, and then held the sample at the growth temperature for 5 minutes under an arsenic flux to anneal the TSQDs. The annealed TSQDs have the same average volume (1344 nm^3) as 4.5 ML TSQDs grown under the same conditions without annealing (1395 nm^3), which lends support to an equilibrium size explanation for our

observations. Interestingly, although total TSQD volume remains constant, we do see a reduction in TSQD aspect ratio. A change in aspect ratio is consistent with the trend for samples grown at higher T_{SUB} that we attributed to annealing, helping to confirm that conclusion.

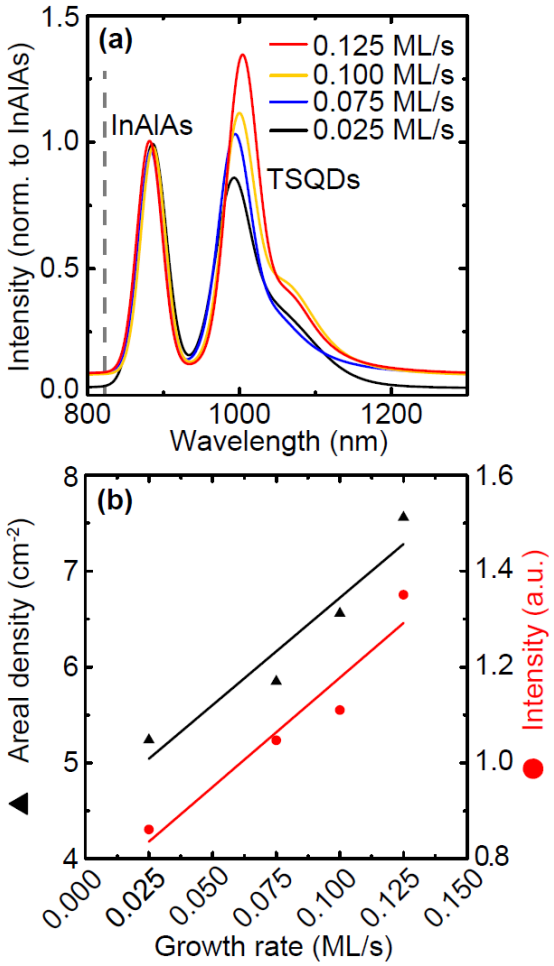

Figure 2.5: (a) PL emission wavelength and intensity with increasing growth rate. Peak TSQD PL wavelength remains constant with increasing growth rate. Peak PL intensity increases with growth rate. (b) TSQD areal density and peak PL intensity as a function of growth rate. Peak PL intensity and TSQD areal density increase monotonically with growth rate, suggesting that brighter PL emission with growth rate is due to the presence of more TSQD emitters.

TSQD areal density and PL peak intensity both increase monotonically with increasing growth rate (***Figure 2.5(b)***). The presence of a secondary TSQD population at

low growth rate therefore accounts for the disparity between TSQD volume and peak wavelength. Areal density versus total PL emission is also linear, resulting in little variation in emission efficiency at different growth rates. Therefore, the increase in the total number of TSQDs at higher growth rate fully accounts for the observed increase in peak PL intensity.

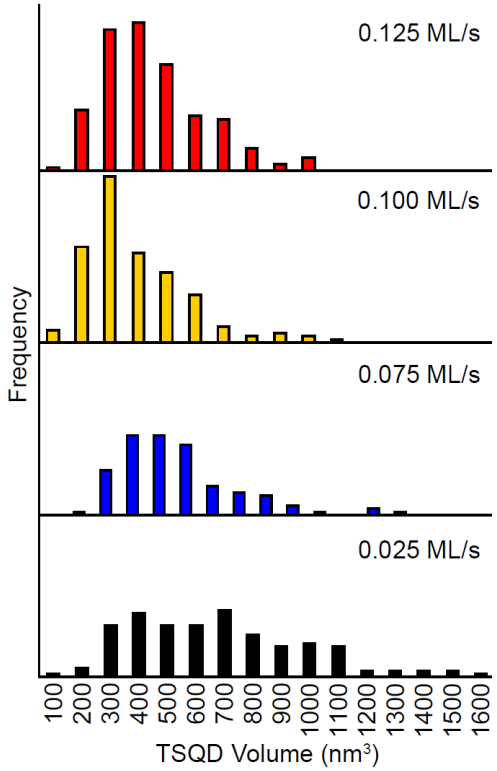

Figure 2.6: Histograms of average TSQD volume as a function of increasing growth rate. For all samples, we see a consistent peak corresponding to TSQDs with average volume 300 – 500 nm^3 (as also seen in the ML series (Figure 2.2)). However, for the 0.025 ML/s sample, a broad secondary population > 700 nm^3 is also present.

2.3.4 V/III Ratio Series

As we increase the As_4/Ga (V/III) BEP ratio from 50 – 110, the average height, diameter, and volume of the 3.5 ML TSQDs remain statistically constant (***Table 2.4***).

However, areal density increases exponentially across the same range of V/III ratios (***Table 2.4***).

Table 2.4: V/III ratio series characterization statistics (deposition amount, T_{SUB}, and growth rate held constant (see Section 2.2)). TSQD height, diameter, and volume average (with standard deviations), and areal density, are determined from AFM images. Peak PL wavelength and intensity are taken as the highest TSQD emission peak, with the intensity of each spectrum normalized to the nominally consistent PL peak from the InAlAs barriers. Total PL emission is taken as the integrated area under the TSQD PL emission curve. Emission efficiency is the ratio of total PL emission and areal density, normalized to the highest emission efficiency obtained. TSQD height, diameter, volume, and peak wavelength are statistically constant with increasing V/III ratio. With increasing V/III ratio, TSQD areal density increases exponentially, while peak PL intensity decreases exponentially. These data suggest a significant decrease in crystal quality, confirmed by a substantial reduction in emission efficiency at higher V/III ratio.

	V/III 50	V/III 75	V/III 110
Height (nm)	0.65 ± 0.12	0.96 ± 0.23	0.72 ± 0.22
Diameter (nm)	51 ± 9	46 ± 11	55 ± 11
Volume (nm^3)	337 ± 139	419 ± 223	471 ± 260
Areal Density (cm^{-2})	2.1×10^8	5.9×10^8	17.1×10^8
Peak PL Wavelength (nm)	982	992	987
Peak PL Intensity (a.u.)	3.45	1.05	0.52
Total PL Emission (a.u.)	184.2	83.6	110.8
Emission Efficiency (a.u.)	100	16.3	7.4

Such strong effects on QD areal density are more typically experienced when increasing growth rate [47], which given the group V rich growth regimes typically adopted for these materials, is determined by the group III flux. That growth rate (varying group III and V flux together) has only a small effect on areal density, while V/III ratio (varying only group V flux) has a large effect, could indicate a group V rate-limiting step [50]. Further, the fact that the observed change in areal density is exponential would mean that for the (111)A surface this rate step is second-order with respect to As_4 flux [51]. Such behavior would mean that TSQD properties are much more sensitive than expected to variations in group V flux. This sensitivity of TSQD formation to As_4 flux is

likely related to a kinetic step requiring the bimolecular reaction of As_4 molecules for incorporation, and the additional reaction pathways available due to As_4 dissociation into As_2 dimers [52]–[54]. This step could be related to a second-order reaction of As_4 with Ga, which is known to occur on the GaAs(100) surface [55], [56]. However, the shorter lifetimes of both As_2 and As_4 on (111) surfaces compared with (100) could also play a role [54], [57]. To distinguish between these factors, further experiments are planned in which we will explore how As_2 and As_4 impact TSQD formation on (111) surfaces. These experiments must be performed independently for the (111)A and (111)B surfaces due to the differences in surface reconstruction, surface diffusion, and surface energy that result from their termination with either a Group III or Group V atom [43], [44].

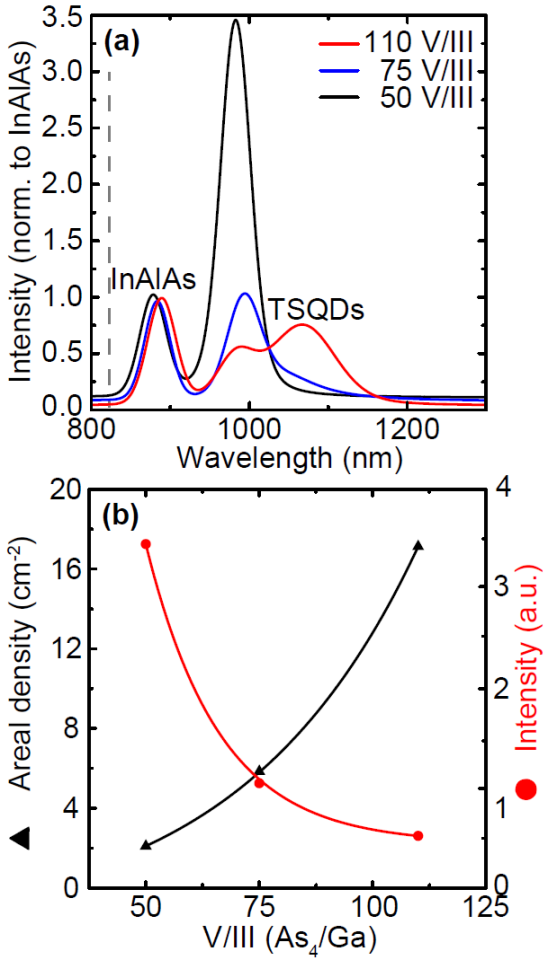

Figure 2.7: (a) PL emission wavelength and intensity with increasing V/III ratio. Peak TSQD PL wavelength remains constant with increasing growth rate. Peak PL intensity decreases significantly with V/III ratio. (b) TSQD areal density and peak PL intensity as a function of V/III ratio. With increasing V/III ratio, peak PL intensity decreases exponentially, while TSQD areal density increases exponentially, suggesting V/III ratio has a significant effect on crystal quality, possible due to increased As anti-site defects at higher As concentrations.

PL measurements for the V/III ratio series provide a striking contrast to the other three series (***Figure 2.7(a)***). Even as TSQD areal density increases exponentially with higher As_4, peak PL intensity decreases exponentially (***Figure 2.7(b)***). A plot of areal density versus total PL emission is non-monotonic with a dramatic decrease in PL emission efficiency as we increase V/III ratio from 50 to 110. Taken together, these results suggest that the decrease in peak PL intensity is due to defect formation, most

likely arsenic anti-site defects since these are the most common point defect in GaAs [58]. The fact that we see indications of a reaction rate that is highly sensitive to As flux means V/III ratio must be carefully optimized during the growth of GaAs (111)A TSQDs to maintain crystal quality.

A histogram of TSQD volume (not shown here) indicates that the origin of the longer wavelength PL peak (see particularly the V/III = 110 sample) is a secondary population of larger volume TSQDs. However, comparing the large reduction in TSQD emission efficiency nevertheless confirms significantly reduced crystal quality with increasing V/III ratio (as we saw previously with decreasing T_{SUB}). In the future, we hope to determine whether we can adjust other growth parameters to grow these larger TSQDs with improved crystal quality, since this could be another route by which to tune TSQD emission toward the IR.

2.4 Summary and Conclusions

We have shown that by manipulating MBE parameters we can reliably control TSQD structural and optical properties. TSQD volume, height, and aspect ratio can all be adjusted consistently. We can also tune TSQD areal density, which is typically low (on the order of 10^8 cm^{-2}). PL emission wavelength is tunable with TSQD size, and occurs below the bulk band gap due to the large residual tensile strain. The results of these experiments posit several interesting possibilities regarding the underlying physics of both (111)-oriented and tensile-strained QD growth.

These experiments reveal two routes by which we expect to obtain brighter TSQD PL emission:

i) using higher growth rates to narrow the QD size distribution; and

ii) growing at higher T_{SUB} or lower V/III ratio to improve QD crystal quality.

In future, a TSQD system with higher tensile strain, or a smaller band gap, could allow us to red-shift PL emission even further for IR applications. The results presented here explicate the use of MBE parameters to adjust the Stranski-Krastanov process, and hence to tailor the structural and optical properties of self-assembled GaAs TSQDs on (111) surfaces. This work provides a comprehensive foundation for research into the growth and applications of these promising nanostructures.

Acknowledgements

This material is based on work supported by the National Science Foundation under NSF CAREER Grant No. 1555270. We also thank Minjoo Larry Lee for useful discussions.

References

[1] B. A. Joyce and D. D. Vvedensky, "Self-organized growth on GaAs surfaces," *Mater. Sci. Eng. R*, vol. 46, pp. 127–176, 2004.

[2] F. Ratto and F. Rosei, "Order and disorder in the heteroepitaxy of semiconductor nanostructures," *Mater. Sci. Eng. R*, vol. 70, pp. 243–264, 2010.

[3] C. D. Yerino *et al.*, "Strain-driven growth of GaAs(111) quantum dots with low fine structure splitting," *Appl. Phys. Lett.*, vol. 105, 251901, 2014.

[4] G. Signorello *et al.*, "Inducing a direct-to-pseudodirect band gap transition in wurtzite GaAs nanowires with uniaxial stress.," *Nat. Commun.*, vol. 5, no. 7491, p. 3655, 2014.

[5] A. Schliwa, M. Winkelnkemper, A. Lochmann, E. Stock, and D. Bimberg, "In(Ga)As/GaAs quantum dots grown on a (111) surface as ideal sources of entangled photon pairs," *Phys. Rev. B*, vol. 80, no. 16, 161307, 2009.

[6] R. Singh and G. Bester, “Nanowire quantum dots as an ideal source of entangled photon pairs,” *Phys. Rev. Lett.*, vol. 103, no. 063601, pp. 1–4, 2009.

[7] C. D. Yerino, B. Liang, D. L. Huffaker, P. J. Simmonds, and M. L. Lee, “Review Article: Molecular beam epitaxy of lattice-matched InAlAs and InGaAs layers on InP(111)A, (111)B, and (110),” *J. Vac. Sci. Technol. B*, vol. 35, 010801, 2017.

[8] A. Ohtake, M. Ozeki, and J. Nakamura, “Strain Relaxation in InAs/GaAs(111)A Heteroepitaxy,” *Phys. Rev. Lett.*, vol. 84, no. 20, pp. 4665–4668, 2000.

[9] H. Yamaguchi *et al.*, “Atomic-scale imaging of strain relaxation via misfit dislocations in highly mismatched semiconductor heteroepitaxy: InAs/GaAs(111)A,” *Phys. Rev. B*, vol. 55, no. 3, pp. 1337–1340, 1997.

[10] H. Yamaguchi, M. R. Fahy, and B. A. Joyce, “Inhibitions of three dimensional island formation in InAs films grown on GaAs(111)A surface by molecular beam epitaxy,” *Appl. Phys. Lett.*, vol. 69, no. 6, pp. 776–778, 1996.

[11] D. Pachinger, H. Groiss, M. Teuchtmann, G. Hesser, and F. Schäffler, “Surfactant-mediated Si quantum dot formation on Ge(100),” *Appl. Phys. Lett.*, vol. 98, no. 22, pp. 28–31, 2011.

[12] J. Petruzzello and M. R. Leys, “Effect of the sign of misfit strain on the dislocation structure at interfaces of heteroepitaxial GaAsP films,” *Appl. Phys. Lett.*, vol. 53, no. 24, pp. 2414–2416, 1988.

[13] P. J. Simmonds and M. L. Lee, “Tensile-strained growth on low-index GaAs,” *J. Appl. Phys.*, vol. 112, 054313, 2012.

[14] P. J. Simmonds and M. L. Lee, “Self-assembly on (111)-oriented III-V surfaces,” *Appl. Phys. Lett.*, vol. 99, 123111, 2011.

[15] D. J. Eaglesham and M. Cerullo, “Dislocation-free Stranski-Krastanow growth of Ge on Si (100),” *Physical Review Letters*, vol. 64, no. 16. pp. 1943–1946, 1990.

[16] D. Leonard, M. Krishnamurthy, C. M. Reaves, S. P. Denbaars, and P. M. Petroff, “Direct formation of quantum-sized dots from uniform coherent islands of

InGaAs on GaAs surfaces," *Appl. Phys. Lett.*, vol. 63, no. 23, pp. 3203–3205, 1993.

[17] D. L. Huffaker, G. Park, Z. Zou, O. B. Shchekin, and D. G. Deppe, "1.3 μm room-temperature GaAs-based quantum-dot laser," *Appl. Phys. Lett.*, vol. 73, no. 18, p. 2564, 1998.

[18] H. W. Li *et al.*, "Quantum dot resonant tunneling diode for telecommunication wavelength single photon detection," *Appl. Phys. Lett.*, vol. 91, no. 7, 073516, 2007.

[19] P. J. Simmonds *et al.*, "Improved quantum dot stacking for intermediate band solar cells using strain compensation," *Nanotechnology*, vol. 25, 445402, 2014.

[20] K. Onomitsu, R. Neufeld, K. Kumakura, and H. Yamamoto, "Growth of MoSe2 Thin Films by Molecular Beam Epitaxy," in *18th International Conference on Molecular Beam Epitaxy*, 2014, pp. 453–454.

[21] Y. Takagaki and B. Jenichen, "Epitaxial growth of Bi2Se3 layers on InP substrates by hot wall epitaxy," *Semicond. Sci. Technol.*, vol. 27, no. 3, 035015, 2012.

[22] A. J. Shields, "Semiconductor quantum light sources," *Nat. Photonics*, vol. 1, no. 4, pp. 215–223, Apr. 2007.

[23] G. Juska *et al.*, "Conditions for entangled photon emission from (111) B site-controlled pyramidal quantum dots," *J. Appl. Phys.*, vol. 117, 134302, 2015.

[24] J. Treu, C. Schneider, A. Huggenberger, T. Braun, S. Reitzenstein, and S. Ho, "Substrate orientation dependent fine structure splitting of symmetric In(Ga)As/GaAs quantum dots," *Appl. Phys. Lett.*, vol. 101, 022102, 2012.

[25] E. Stock *et al.*, "Single-photon emission from InGaAs quantum dots grown on (111) GaAs," *Appl. Phys. Lett.*, vol. 96, no. 9, pp. 96–99, 2010.

[26] K. Mitsuishi *et al.*, "Self-Assembly of Symmetric GaAs Quantum Dots on (111)A Substrates: Suppression of Fine-Structure Splitting," *Appl. Phys. Express*, vol. 3, 065203, 2010.

[27] P. J. Simmonds *et al.*, “Tuning Quantum Dot Luminescence Below the Bulk Band Gap Using Tensile Strain,” *ACS Nano*, vol. 7, no. 6, pp. 5017–5023, 2013.

[28] C. D. Yerino *et al.*, “Tensile GaAs(111) quantum dashes with tunable luminescence below the bulk band gap,” *Appl. Phys. Lett.*, vol. 105, 071912, 2014.

[29] J. M. O. Zide *et al.*, “Increased efficiency in multijunction solar cells through the incorporation of semimetallic ErAs nanoparticles into the tunnel junction,” *Appl. Phys. Lett.*, vol. 88, no. 16, 162103, 2006.

[30] M. El Kurdi, G. Fishman, Ś. Sauvage, and P. Boucaud, “Band structure and optical gain of tensile-strained germanium based on a 30 band kp formalism,” *J. Appl. Phys.*, vol. 107, 013710, 2010.

[31] X. Li, K. Maute, M. L. Dunn, and R. Yang, “Strain effects on the thermal conductivity of nanostructures,” *Phys. Rev. B*, vol. 81, no. 24, 245318, 2010.

[32] A. Ghrib *et al.*, “Tensile-strained germanium microdisks,” *Appl. Phys. Lett.*, vol. 102, no. 22, 221112, 2013.

[33] J. Greil, a. Lugstein, C. Zeiner, G. Strasser, and E. Bertagnolli, “Tuning the electro-optical properties of germanium nanowires by tensile strain,” *Nano Lett.*, vol. 12, no. 12, pp. 6230–6234, 2012.

[34] P. J. Simmonds and M. L. Lee, “Tensile strained island growth at step-edges on GaAs(110),” *Appl. Phys. Lett.*, vol. 97, no. 15, 153101, 2010.

[35] E. P. Kvam and R. Hull, “Surface orientation and stacking fault generation in strained epitaxial growth,” *J. Appl. Phys.*, vol. 73, no. 11, pp. 7407–7411, 1993.

[36] H. Lee, R. R. Lowe-Webb, W. Yang, and P. C. Sercel, “Formation of InAs/GaAs quantum dots by molecular beam epitaxy: Reversibility of the islanding transition,” *Appl. Phys. Lett.*, vol. 71, no. 16, pp. 2325–2327, 1997.

[37] R. L. Schwoebel and E. J. Shipsey, “Step Motion on Crystal Surfaces,” *J. Appl. Phys.*, vol. 37, no. 10, pp. 3682–3686, 1966.

[38] P. B. Joyce *et al.*, “Growth rate effects on the size, composition and optical properties of InAs / GaAs quantum dots grown by molecular beam epitaxy,” *J. Cryst. Growth*, vol. 227–228, pp. 1000–1004, 2001.

[39] K. Jacobi, “Atomic structure of InAs quantum dots on GaAs (review),” *Prog. Surf. Sci.*, vol. 71, pp. 185–215, 2003.

[40] V. Shchukin, E. Scholl, and P. Kratzer, “Thermodynamics and kinetics of quantum dot growth,” in *Semiconductor Nanostructures*, D. Bimberg, Ed. Berlin Heidelberg New York: Springer, pp. 1–39, 2008.

[41] S. Bietti, L. Esposito, A. Fedorov, A. Ballabio, A. Martinelli, and S. Sanguinetti, “Characterization and Effect of Thermal Annealing on InAs Quantum Dots Grown by Droplet Epitaxy on GaAs(111)A Substrates,” *Nanoscale Res. Lett.*, vol. 10, no. 1, p. 247, 2015.

[42] M. C. Xu, Y. Temko, T. Suzuki, and K. Jacobi, “Shape transition of InAs quantum dots on GaAs(100),” *J. Appl. Phys.*, vol. 98, 083525, 2005.

[43] J. W. Cahn and R. E. Hanneman, “(111) Surface tensions of III–V compounds and their relationship to spontaneous bending of thin crystals,” *Surf. Sci.*, vol. 1, pp. 387–398, 1964.

[44] T. Takebe, M. Fujii, T. Yamamoto, K. Fujita, and T. Watanabe, “Orientation-dependent Ga surface diffusion in molecular beam epitaxy of GaAs on GaAs patterned substrates,” *J. Appl. Phys.*, vol. 81, no. 11, pp. 7273–7281, 1997.

[45] C. Lobo and R. Leon, “InGaAs island shapes and adatom migration behavior on (100), (110), (111), and (311) GaAs surfaces,” *J. Appl. Phys.*, vol. 83, no. 8, pp. 4168–4172, 1998.

[46] A.-L. Barabási, “Thermodynamic and kinetic mechanisms in self-assembled quantum dot formation,” *Mater. Sci. Eng. B*, vol. B67, pp. 23–30, 1999.

[47] P. B. Joyce *et al.*, “Effect of growth rate on the size, composition, and optical properties of InAs/GaAs quantum dots grown by molecular-beam epitaxy,” *Phys. Rev. B*, vol. 62, no. 16, pp. 10891–10895, 2000.

[48] H. Dobbs, D. D. Vvedensky, A. Zangwill, J. Johansson, N. Carlsson, and W. Seifert, “Mean-Field Theory of Quantum Dot Formation,” *Phys. Rev. Lett.*, vol. 79, no. 5, pp. 897–900, 1997.

[49] I. Daruka and A.-L. Barabási, “Equilibrium phase diagrams for dislocation free self-assembled quantum dots,” *Appl. Phys. Lett.*, vol. 72, no. 17, pp. 2102–2104, 1998.

[50] A. Madhukar, Q. Xie, P. Chen, and A. Konkar, “Nature of strained InAs three-dimensional island formation and distribution on GaAs(100),” *Appl. Phys. Lett.*, vol. 64, no. 20, pp. 2727–2729, 1994.

[51] J. H. Van’t Hoff, ́Etudes De Dynamique Chimique (“Studies in Chemical Dynamics”). Amsterdam: Frederick Muller, 1884.

[52] E. S. Tok, J. H. Neave, J. Zhang, B. A. Joyce, and T. S. Jones, “Arsenic incorporation kinetics in GaAs(100) homoepitaxy revisited,” *Surf. Sci.*, vol. 374, pp. 397–405, 1997.

[53] Y. G. Galitsyn, I. I. Marakhovka, S. P. Moshchenko, and V. G. Mansurov, “As4 incorporation kinetics in GaAs (100) molecular-beam epitaxy,” *Tech. Phys. Lett.*, vol. 24, no. 4, pp. 260–262, 1998.

[54] B. A. Joyce, D. D. Vvedensky, T. S. Jones, M. Itoh, G. R. Bell, and J. G. Belk, “In situ studies of III-V semiconductor film growth by molecular beam epitaxy,” *J. Cryst. Growth*, vol. 201/202, pp. 106–112, 1999.

[55] C. T. Foxon and B. A. Joyce, “Interaction kinetics of As2 and Ga on {100} GaAs surfaces,” *Surface Science*, vol. 64, no. 1. pp. 293–304, 1977.

[56] A. Avery, H. Dobbs, D. Holmes, B. Joyce, and D. Vvedensky, “Nucleation and Growth of Islands on GaAs Surfaces,” *Phys. Rev. Lett.*, vol. 79, no. 20, pp. 3938–3941, 1997.

[57] M. R. Fahy, K. Sato, and B. A. Joyce, “Reflection high-energy electron diffraction intensity oscillations during the growth by molecular beam epitaxy of GaAs (111)A,” *Appl. Phys. Lett.*, vol. 64, no. 2, pp. 190–192, 1993.

[58] H. P. Komsa and A. Pasquarello, “Comparison of vacancy and antisite defects in GaAs and InGaAs through hybrid functionals,” *Phys. B*, vol. 407, no. 15, pp. 2833–2837, 2012.

CHAPTER THREE: ANOMALOUS STRANSKI-KRASTANOV GROWTH OF (111)-ORIENTED QUANTUM DOTS WITH TUNABLE WETTING LAYER THICKNESS

Christopher F. Schuck,[1]* Simon K. Roy,[2] Trent Garrett,[2] Qing Yuan,[3] Ying Wang,[3] Carlos I. Cabrera,[4] Kevin A. Grossklaus,[5] Thomas E. Vandervelde,[5] Baolai Liang,[3] and Paul J. Simmonds[1,2]†

[1] *Micron School of Materials Science & Engineering, Boise State University, Boise, Idaho 83725, USA*

[2] *Department of Physics, Boise State University, Boise, Idaho 83725, USA*

[3] *College of Physics Science & Technology, Hebei University, Baoding 071002, P.R. China*

[4] *Center for Research in Sciences, Research Institute in Basic and Applied Sciences, Autonomous University of the State of Morelos, Av. Universidad 1001, 62209, Cuernavaca, Morelos, Mexico*

[5] *Department of Electrical and Computer Engineering, Tufts University, 161 College Avenue, Medford, Massachusetts 02155, USA*

* E-mail address: christopherschuck@boisestate.edu

† E-mail address: paulsimmonds@boisestate.edu

Pending submission for publication.

Abstract

GaAs tensile-strained quantum dots (TSQDs) self-assemble on InAlAs(111)A surfaces via an unusual modification to the conventional Stranski-Krastanov (SK) mechanism. The two-dimensional (2D) wetting layer (WL) beneath the TSQDs continues to increase in thickness, even after the SK transition to a 3D growth mode. We confirm this anomalous SK mechanism with microscopy, spectroscopy, and computational modeling. By tuning both TSQD size and WL thickness, we can modify the quantum dot-quantum well interactions in this hybrid quantum system. Future benefits include more accurate control over TSQD band structure for infrared optoelectronic applications and quantum optics.

3.1 Introduction

Historically, researchers have classified epitaxial growth into three modes: two dimensional (2D) layer-by-layer growth (Frank-van der Merwe), 3D island formation (Volmer-Weber), or layer-plus-island growth (Stranski-Krastanov (SK)) [1], [2]. We can take advantage of SK growth to achieve strain-driven self-assembly of dislocation-free semiconductor quantum dots (QDs) with tunable optoelectronic properties [2]–[6]. SK QD growth proceeds as follows: (i) a 2D wetting layer (WL) forms; (ii) at some critical thickness, t_c, 3D QDs nucleate and self-assemble on the WL; and (iii) the QDs grow while the WL thickness is pinned at t_c [2], [7].

The WL quantum well (QW) behaves essentially as a carrier reservoir, interconnecting all QDs in a layer. WL thickness can thus have significant influence on QD band structure; affecting emission wavelength [8]–[11], band edge profile [11], carrier confinement depth [8], [9], excited state and charged exciton energy levels [8],

[9], QD-WL interaction strength [8], and WL interface fluctuations[12]. Although these effects have important implications for QD devices [8]–[14], our ability to take advantage of them is hindered by the fact that the maximum WL thickness, t_c, is a fixed parameter in conventional SK self-assembly [2], [7]–[11], [14]. For example, for compressively strained InAs on GaAs, once the InAs WL thickness reaches $\underline{t}_c$ ~1.6 ML, all additional InAs deposited contributes to QD self-assembly [2], [15], [16].

To sidestep this constraint on WL thickness, researchers have developed some creative approaches to manipulate WL thickness, including high-temperature WL desorption [16], modified droplet epitaxy [9], and unstrained inverted QD structures [8]. However, the ability to simply tune WL thickness in a single SK growth step without additional processing, would provide a scalable route to optoelectronic devices with complete control over WL/QD interactions.

In this paper we demonstrate that an anomalous SK growth mode governs QD self-assembly, wherein the WL thickness is tunable. We grow GaAs tensile-strained QDs (TSQDs) on InAlAs(111)A by molecular beam epitaxy (MBE). The GaAs TSQDs exhibit unique properties that derive from the tensile strain, as well as their (111) orientation [17]–[19]. Growth proceeds via the initial formation of a 2D WL, followed by a transition to 3D TSQD self-assembly. However, in contrast with conventional SK growth, GaAs deposition beyond t_c increases both QD size *and* WL thickness.

3.2 Experimental Methods

Samples consist of an $In_{0.52}Al_{0.48}As$ (hereafter InAlAs) bottom barrier followed by 0.5–4.5 monolayers (ML) embedded GaAs TSQDs for optical analysis, then an InAlAs capping layer followed by another 0.5-4.5 ML surface GaAs TSQDs for structural

analysis. TSQD growth conditions are optimized for high intensity photon emission [17]–[20]. [See Supplemental Material at the end of this Chapter for sample structure details and MBE conditions] [21].

We measured the sizes of ≥ 100 tetrahedral surface TSQDs per sample with atomic force microscopy (AFM). Subtracting the total volume of the TSQDs from the total amount of GaAs deposited gives the WL volume per unit area. We use photoluminescence (PL) (excitation laser wavelength = 532 nm, excitation density = 0.3–3000 W/cm^2, temperature = 7–300 K) to explore the optical characteristics of the buried TSQDs. We compare PL from these coupled WL-QD systems, to a bulk InAlAs(111)A (0 ML GaAs) reference sample [17].

To image WL and TSQD structure we use high-resolution cross-sectional transmission electron microscopy (XTEM) in bright-field conditions (diffraction contrast), and scanning transmission electron microscopy (STEM) using bright-field and annular dark-field (ADF) imaging modes. To measure WL thickness, we use simultaneous STEM ADF imaging and high spatial resolution electron energy loss spectroscopy (EELS) composition mapping using the Ga L and In M edges.

3.3 Computational Modeling

Tensile strain and quantum confinement act in opposition, respectively reducing and increasing the effective TSQD band gap [18], [22], [23]. Given the “push-pull” nature of these contributions, TSQD band structure as a function of size is fairly complex. To compute the strain-induced modification of the GaAs band gap, we resolve the total strain into its hydrostatic and biaxial components. The hydrostatic component acts on the band edges, thereby changing the band gap. The biaxial component acts on the valence

bands. Decoupling the conduction and valence bands, the strain-induced changes to the band edges at the Γ point are given by [24],

$$\delta E_c = a_c(2\varepsilon_{\parallel} + \varepsilon_{\perp}), \qquad \text{(1a)}$$

$$\delta E_v = a_v(2\varepsilon_{\parallel} + \varepsilon_{\perp}) \pm b(\varepsilon_{\parallel} - \varepsilon_{\perp}), \qquad \text{(1b)}$$

where + (–) applies to the light hole, *lh* (heavy hole, *hh*) band. a_c and a_v are the conduction and valence band hydrostatic deformation potentials. b is the shear deformation potential. The in-plane, $\varepsilon_{\parallel}$, and perpendicular, $\varepsilon_{\perp}$, strains, are related by the Poisson ratio for the (111) orientation [25]. Tensile strain reduces the GaAs band gap and breaks the valence band degeneracy at the Γ point, raising the *lh* band above the *hh* band ***Figure 3.1(a)***].

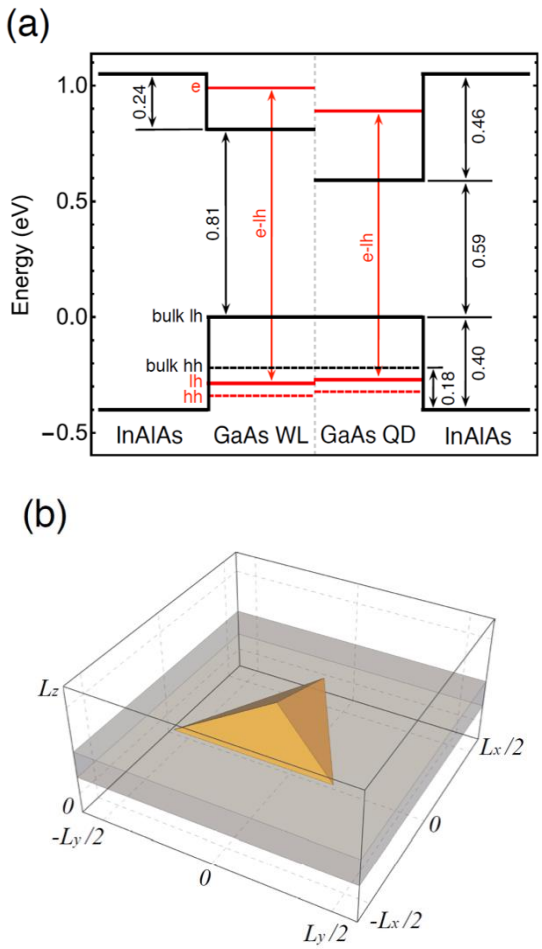

Figure 3.1: (a) Calculated band diagram for a 4 ML GaAs(111) TSQD under 3.7% biaxial tensile strain. The ground state emission is in red. (b) Illustration of the geometric TSQD configuration used in the model.

We deduce carrier confinement potentials, *U*, by adding the strain-induced changes in Eqs. (1a–b) to the GaAs/InAlAs heterostructure band offsets. We take the offset ratio for the unstrained bands from the difference in absolute energetic position of the average valence band [25].

We treat the WL as a QW and use the envelope function approximation to compute the conduction band energy levels. We describe electron behavior in the QW using the Schrödinger equation within the effective mass approximation. To determine the QW energy levels in the *lh* and *hh* bands under tensile strain, we use a 4×4 ***k·p*** Kohn-

Luttinger Hamiltonian [24].

To establish TSQD electronic structure, we adopt a single-band, constant-confining-potential model, using the Hamiltonian operator to calculate electron and hole energy levels:

$$H(r) = -\frac{\hbar^2}{2}\left(\nabla \frac{1}{m^*(r)}\nabla\right) + U(r). \quad (2)$$

For tetrahedral TSQDs with an equilateral triangle base, we expand the envelope function $\psi(r)$, as a linear combination of a basis set, $\{\varphi\}$, of the solutions of the cuboidal QD, $L_xL_yL_z$, with infinite barrier height, $\psi(r) = \sum_{lmn} \quad a_{lmn}\phi_{lmn}(r)$ [***Figure 3.1(b)***]. Following Van de Walle's approach,[25] we obtain the TSQD energy levels by solving the matrix equation

$$(M_{lmnl'm'n'} - E\delta_{ll'}\delta_{mm'}\delta_{nn'})a_{lmn} = 0,$$

where we have used wave function orthonormality. The matrix elements $M_{lmnl'm'n'}$ are given by [26]:

$$M_{lmnl'm'n'} = \int \quad \psi^*_{l'm'n'}H(r)\psi_{lmn}dr =$$

$$\left[\frac{\hbar^2\pi^2}{2m_b^*}\left(\frac{ll'}{L_x^2} + \frac{mm'}{L_y^2} + \frac{nn'}{L_z^2}\right) + U\right]\delta_{ll'}\delta_{mm'}\delta_{nn'} + \frac{\hbar^2}{2}\left(\frac{1}{m_d^*} - \frac{1}{m_b^*}\right)\int_D \quad \nabla\phi^*_{l'm'n'}\nabla\phi_{lmn}dr - U\int_D \quad \phi^*_{l'm'n'}\phi_{lmn}dr,$$

where integration is over the TSQD region (*D)*. m_d^* and m_b^* are the carrier effective masses in the GaAs TSQDs and InAlAs barriers respectively. To ensure energy eigenvalues are independent of the outer box size, we use values $L_x = L_y = 150\ nm$ and $L_z = L_x/2$. To ensure convergence within 1 meV for all TSQD sizes, we use a basis set of 19^3 wavefunctions [27]. We then solve the matrix $M_{lmnl'm'n'}$ numerically using the

Monte Carlo method.

3.4 Results and Discussion

3.4.1 AFM: WL Growth Beyond t_c

For deposition < 2.5 ML, GaAs forms a 2D WL with ML-high terraces and no TSQDs [***Figure 3.2(a)***]. At t_c = 2.5 ML GaAs, a low density of small 3D tetrahedral TSQDs appear [***Figure 3.2(b)***]. This 2D-to-3D transition is consistent with SK growth. By 4.5 ML GaAs, TSQD volume and areal density increase, but remain low compared to traditional QD materials systems [***Figure 3.2(c)***] [2], [28]. In all samples, the volume of GaAs in the TSQDs is ≤ 1% of the total deposited [see Supplemental Material at the end of this Chapter] [21]. Most GaAs must therefore join the WL, even for deposition exceeding t_c = 2.5 ML.

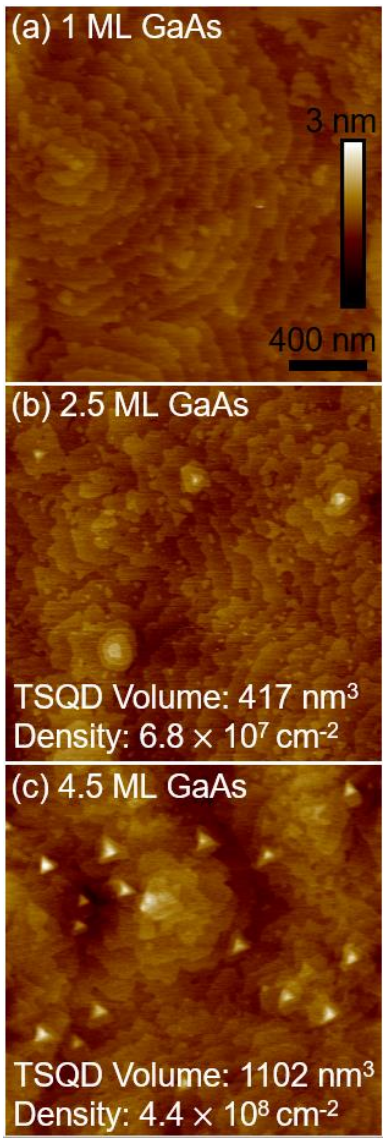

Figure 3.2: 2·2 ⌈m² AFM images showing TSQD evolution with increasing GaAs deposition amount: (a) 1 ML, (b) 2.5 ML, (c) 4.5 ML.

3.4.2 PL Spectroscopy: Evidence for Unusual WL Behavior

The GaAs/InAlAs(111)A TSQD samples exhibit three spectral features [***Figure 3.3***]. The 0 ML GaAs reference sample has a single InAlAs emission peak at 852 nm. For 0.5 ML GaAs deposition, a shoulder emerges on the long wavelength side of the InAlAs peak and resolves into a discrete peak at 2.5 ML, which we refer to as the 'primary' peak. As we raise the amount of GaAs from 0.5–4.5 ML, the primary peak wavelength

increases from 890–1000 nm. At 2.5 ML GaAs deposition, a third peak develops at yet longer wavelength, which we refer to as the 'secondary' peak. The emergence of this broader, secondary peak coincides with the appearance of TSQDs [***Figure 3.2(b)***]. As we raise the amount of GaAs from 2.5–4.5 ML, the secondary peak wavelength increases from 987–1160 nm.

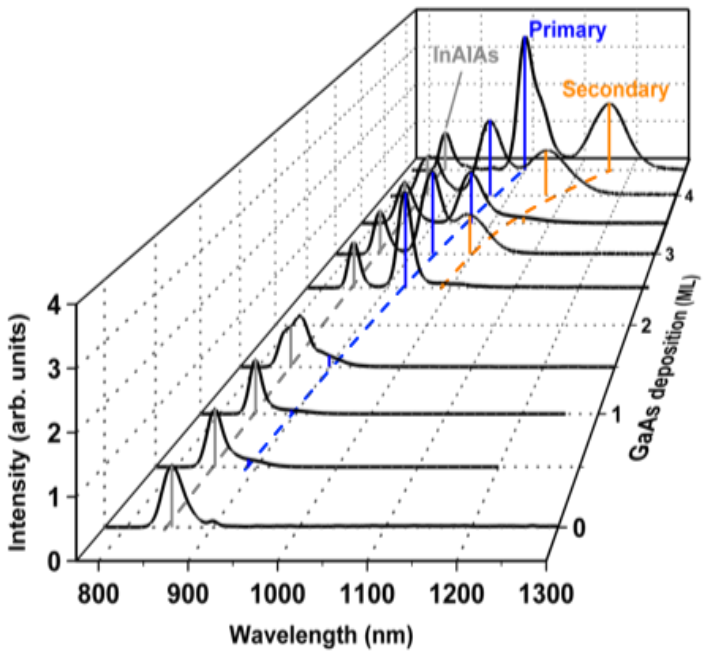

Figure 3.3: PL emission at 7 K from TSQD samples, showing spectral evolution with increasing GaAs deposition amount. Excitation density is 9.5 W/cm^2.

Due to the 3.7% tensile strain, both the primary and secondary GaAs-related PL peaks are longer in wavelength than band-to-band emission from bulk GaAs (816 nm at 7 K).[18], [22], [29] Guided by PL studies of conventional, compressively strained InAs QDs, we tentatively attribute the primary peak to the GaAs WL, and the secondary peak to the GaAs TSQDs [30]. The high intensity of the WL peak relative to the TSQD peak results from the low dot densities (10^8–10^9 cm^{-2}).

The secondary peak redshifts as we deposit more GaAs, consistent with

increasing TSQD volume producing quantum size effects. However, the primary peak also redshifts after TSQDs appear, which is completely unexpected. If the primary peak corresponds to WL emission as we conjecture, this wavelength increase supports the indications from AFM that the WL continues to grow beyond t_c. Such behavior is inconsistent with standard SK growth: emission wavelength is fixed for a WL whose thickness is pinned at t_c [31].

3.4.3 Confirmation of PL Peak Assignments

Given this unexpected result, we must exclude alternative explanations for the primary PL peak. Possible origins include TSQD excited-state emission [32], emission from phase-separated In-rich nanoclusters in the InAlAs [33], or emission from a family of smaller GaAs TSQDs due to a bimodal size distribution [17].

The primary peak persists even for PL excitation densities as low as 0.3 W/cm^2, which precludes excited state emission as the cause [***Figure 3.S2***] [21]. We rule out the other two alternative explanations for the primary peak using temperature-dependent PL [***Figure 3.4(a) inset***]. After Gaussian fitting, we plot integrated primary and secondary peak intensities, I, against inverse temperature, $1/T$ [***Figure 3.4(a)***]. For each curve we extract two activation energies, E_1 and E_2, using a biexponential model [33]:

$$I(T) = I_0/\left(1 + C_1 e^{-E_1/k_B T} + C_2 e^{-E_2/k_B T}\right), \quad (5)$$

where I_0 is the integrated intensity at $T = 0$ K, $C_{1,2}$ are constants, and k_B is the Boltzmann constant. The resulting fits agree well with the experimental data [***Figure 3.4(a)***]. For the secondary peak, we obtain $E_1 = 46\ meV$ and $E_2 = 13\ meV$. For the primary peak, values of $E_1 = 24\ meV$ and $E_2 = 9\ meV$ rule out In-rich InAlAs nanoclusters as the cause, since we have previously measured activation energies of $E_1 = 34\ meV$ and $E_2 =$

5 meV for these QD-like features [33].

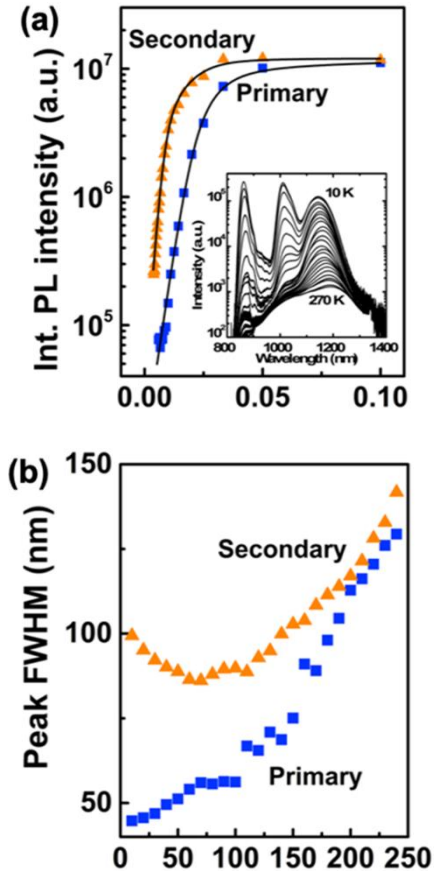

Figure 3.4: (a) Inset: Temperature-dependent PL from 4.5 ML GaAs TSQD sample. (a) Integrated intensities of primary and secondary PL peaks plotted against inverse temperature. Black lines are fits from Eq. 5. (b) FWHM of primary and secondary peaks in (a) as a function of temperature. Excitation density is 9.5 W/cm^2.

As we raise the temperature from 10–80 K, the secondary peak FWHM decreases from 100–85 nm, before increasing again at higher temperatures [***Figure 3.4(b)***]. PL from smaller TSQDs is quenched as weakly confined carriers thermalize into larger dots with lower energy ground states. This "u-shaped" temperature dependence of the FWHM is a characteristic feature of QD arrays, and confirms that TSQD emission produces the secondary peak [22], [34].

The pronounced primary peak at 80 K [***Figure 3.4(a) inset***] excludes bimodal TSQD sizes as its cause. A secondary population of smaller TSQDs would be depleted of

carriers by 80 K. In contrast with the secondary peak, the primary peak FWHM increases continuously with measurement temperature, consistent with thermal broadening of QW emission due to increased electron-phonon scattering and, therefore, confirming that this peak is not related to TSQD emission.

Having confirmed that the primary and secondary peaks originate in the WL and TSQDs respectively, we return to the unusual result that WL growth continues after the SK transition to TSQD formation.

3.4.4 XTEM: Anomalous SK Growth Confirmed

XTEM analysis of the 2.5 and 4.5 ML samples confirms a modified SK growth mode. Clearly resolving the WLs and TSQDs by STEM is difficult due to the low Z-contrast between GaAs and the InAlAs matrix. Imaging the WL in the 2.5 ML GaAs sample is additionally challenging due to its narrow width. However, we can observe the 4.5 ML GaAs TSQDs directly with bright-field TEM due to increased strain contrast [***Figure 3.S3***] [21]. The TSQDs are dislocation-free despite the high tensile strain.

Overlaying ADF images with EELS compositional maps shows that the GaAs WL in the 2.5 ML sample is 3–4 MLs thick, assuming some broadening of the Ga L edge signal [***Figure 3.5(a)***].

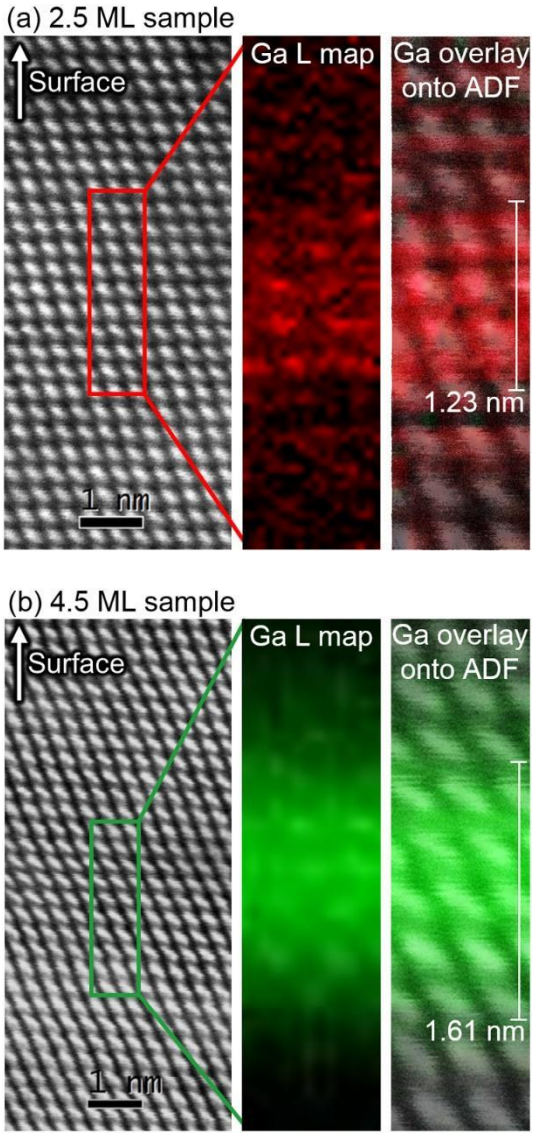

Figure 3.5: STEM ADF images of (a) 2.5 ML and (b) 4.5 ML GaAs TSQD samples, indicating the areas used for EELS compositional mapping of the Ga L signal (central panels). Right-hand panels show EELS maps overlaid on corresponding ADF images.

Taking the average FWHM of the Ga L edge signal from the map in ***Figure 3.5(a)*** and correcting for sample drift in the growth direction during mapping gives an average WL thickness of 1.23±0.11 nm. This corresponds to 3.81±0.34 ML GaAs fully strained in-plane to the InAlAs matrix. Similarly, for the 4.5 ML sample, ADF shows the GaAs WL to be 4–5 ML thick [***Figure 3.5(b)***], and the drift-corrected FWHM of the Ga L edge signal gives an average thickness of 1.61±0.08 nm, which corresponds to

4.98±0.24 ML GaAs.

That these measured WL thicknesses are greater than the nominal GaAs deposition amounts is likely due to a combination of sample drift, low Ga L signal, monolayer-scale thickness variation through the TEM sample, and out diffusion of Ga into the surrounding InAlAs matrix. However, even with these uncertainties, the STEM/EELS measurements [***Figure 3.5***] confirm that WL thickness increases from 2.5 ML GaAs (t_c) to 4.5 ML GaAs (as deposited), consistent with our AFM and PL results.

3.4.5 TSQD & WL Computational Model: Agreement with Experiment

Band structure modeling confirms our experimental conclusions of anomalous SK growth. We calculate WL QW and tetrahedral TSQD ground state energy levels using values for GaAs(111) of $b = -2\ eV$, and $a_v = -2.1\ eV$ [35]. For the WL QW we use $a_c = -7.4\ eV$.[36] For the TSQDs, our model assumes a constant average strained potential throughout a TSQD and does not account for band mixing. Because of these simplifications, we use a_c as a fitting parameter to couple strain to electronic structure. For the TSQDs, $a_c = -11.5\ eV$ gave the closest fit to our PL data [36].

Consistent with previous studies of QD-WL interactions, we adopt an effective TSQD height of $h_{QD} = h_{AFM} + h_{WL}$ (***Figure 3.S4***) [8], [21]. This treatment of the TSQD-WL system is similar to QDs formed due to monolayer-high fluctuations in the QW thickness [12], [37], [38]. Key differences here are that TSQDs are discrete nanostructures that self-assemble due to strain, and that TSQD height is controllable with GaAs deposition amount.

Calculated WL and TSQD transition energies as a function of GaAs deposition agree closely with experimental PL data [***Figure 3.6***]. Our model captures the redshift of

both the TSQD *and* WL peaks as they continuously grow thicker, even beyond t_c = 2.5 ML. We suspect the divergence between model and experiment at low GaAs coverage comes from deposition amount and AFM measurement errors, that are magnified for such small TSQDs. The model also ignores interdiffusion between the GaAs and InAlAs, which could modify the size and composition of WLs and TSQDs. Our model and PL data converge at higher coverage as these sources of error are minimized.

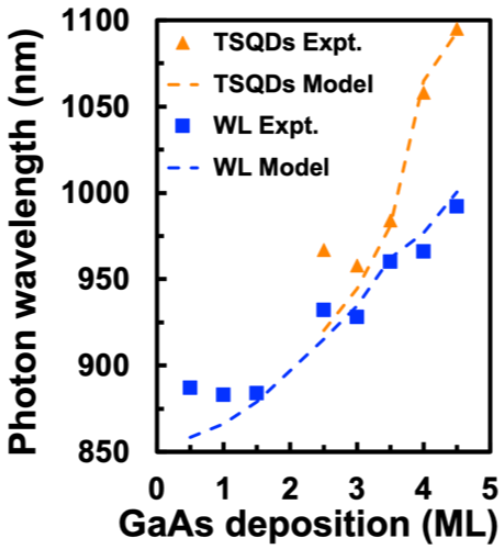

Figure 3.6: PL and model peak emission wavelengths with increasing GaAs deposition amount, for TSQDs and WL QWs. PL excitation density is 3000 W/cm^2.

Overall, the transition energies predicted by our model agree well with experiment for both WL and TSQDs, and confirm SK-like growth with unusual wetting layer behavior.

3.4.6 Anomalous SK Growth Mode Discussion

Although previous studies have hinted at potential anomalies in the SK-based self-assembly of TSQDs [17], [18], the results presented here give a concrete picture. The tensile-strained self-assembly of GaAs(111)A TSQDs allows us to combine highly

controllable SK growth with the additional benefit of a WL whose thickness is tunable. This modification to conventional SK growth is due to the unusual presence of tensile strain, as well as the relative TSQD and barrier surface energies for a (111)A orientation.

The growth mode we observe is perhaps best described as a hybrid of the SK_1 and SK_2 growth modes outlined by Barabási [7]. Adatoms deposited after t_c has been reached bind preferentially to the growing WL, suggesting TSQD formation provides only a subtle reduction in the free energy [7]. This is consistent with the small volume and low areal density of TSQDs, compared to QDs formed during conventional SK growth [2], [17], [28].

3.5 Conclusions

After investigating the structural and optical properties of GaAs/InAlAs(111)A TSQDs, we conclude that self-assembly occurs via a modified version of the well-known SK mechanism. In this anomalous SK growth mode, the WL continues to increase in thickness even after the TSQDs have begun to grow. The ability to control WL thickness as well as QD size during a single SK growth step provides a new avenue for future studies into WL-QD interactions. We anticipate the development of optoelectronic devices that could take advantage of this high degree of structural tunability.

Acknowledgements

This material is based on work supported by the National Science Foundation under NSF CAREER Grant No. 1555270. The authors also acknowledge the high-performance computing support of the R2 compute cluster (DOI: 10.18122/B2S41H) provided by Boise State University's Research Computing Department. CIC thanks COZCYT and CONACYT (Grant No. 337137) for support. Electron microscopy was performed at the

Center for Nanoscale Systems (CNS), a member of the National Nanotechnology Coordinated Infrastructure Network (NNCI), which is supported by the National Science Foundation under NSF award no. 1541959. CNS is part of Harvard University.

References

[1] J. A. Venables, G. D. T. Spiller, and M. Hanbucken, "Nucleation and growth of thin films," *Reports Prog. Phys.*, vol. 47, p. 399, 1984.

[2] B. A. Joyce and D. D. Vvedensky, "Self-organized growth on GaAs surfaces," *Mater. Sci. Eng. R*, vol. 46, pp. 127–176, 2004.

[3] D. Leonard, M. Krishnamurthy, C. M. Reaves, S. P. Denbaars, and P. M. Petroff, "Direct formation of quantum-sized dots from uniform coherent islands of InGaAs on GaAs surfaces," *Appl. Phys. Lett.*, vol. 63, no. 23, pp. 3203–3205, 1993.

[4] G. D. Scholes and G. Rumbles, "Excitons in nanoscale systems," *Nat. Mater.*, vol. 5, no. 11, pp. 920–920, 2006.

[5] D. J. Eaglesham and M. Cerullo, "Dislocation-free Stranski-Krastanow growth of Ge on Si (100)," *Physical Review Letters*, vol. 64, no. 16. pp. 1943–1946, 1990.

[6] F. Ratto and F. Rosei, "Order and disorder in the heteroepitaxy of semiconductor nanostructures," *Mater. Sci. Eng. R*, vol. 70, pp. 243–264, 2010.

[7] A.-L. Barabási, "Thermodynamic and kinetic mechanisms in self-assembled quantum dot formation," *Mater. Sci. Eng. B*, vol. B67, pp. 23–30, 1999.

[8] L. Wang *et al.*, "Self-assembled quantum dots with tunable thickness of the wetting layer: Role of vertical confinement on interlevel spacing," *Phys. Rev. B*, vol. 80, p. 085309, 2009.

[9] S. Sanguinetti *et al.*, "Modified droplet epitaxy GaAs/AlGaAs quantum dots grown on a variable thickness wetting layer," *J. Cryst. Growth*, vol. 253, pp. 71–76, 2003.

[10] M. Shahzadeh and M. Sabaeian, “The effects of wetting layer on electronic and optical properties of intersubband P-to-S transitions in strained dome-shaped InAs/GaAs quantum dots,” *AIP Adv.*, vol. 4, p. 067113, 2014.

[11] C. Sun, P. Lu, Z. Yu, H. Cao, and L. Zhang, “Wetting layers effect on InAs/GaAs quantum dots,” *Phys. B*, vol. 407, pp. 4440–4445, 2012.

[12] Y. Wang *et al.*, “Photoluminescence Study of the Interface Fluctuation Effect for InGaAs/InAlAs/InP Single Quantum Well with Different Thickness,” *Nanoscale Res. Lett.*, vol. 12, p. 229, 2017.

[13] M. Syperek *et al.*, “The issue of 0D-like ground state isolation in GaAs- and InP-based coupled quantum dots-quantum well systems,” *J. Phys. Conf. Ser.*, vol. 906, p. 012019, 2017.

[14] L. Seravalli, C. Bocchi, G. Trevisi, and P. Frigeri, “Properties of wetting layer states in low density InAs quantum dot nanostructures emitting at 1.3 um: Effects of InGaAs capping,” *J. Appl. Phys.*, vol. 108, p. 114313, 2010.

[15] D. Leonard, K. Pond, and P. M. Petroff, “Critical layer thickness for self-assembled InAs islands on GaAs,” *Phys. Rev. B*, vol. 50, no. 16, pp. 687–692, 1994.

[16] H. Zhang, Y. Chen, G. Zhou, C. Tang, and Z. Wang, “Wetting layer evolution and its temperature dependence during self-assembly of InAs/GaAs quantum dots,” *Nanoscale Res. Lett.*, vol. 7, p. 600, 2012.

[17] C. F. Schuck *et al.*, “Self-assembly of (111)-oriented tensile-strained quantum dots by molecular beam epitaxy,” *J. Vac. Sci. Technol. B*, vol. 36, p. 031803, 2018.

[18] C. D. Yerino *et al.*, “Strain-driven growth of GaAs(111) quantum dots with low fine structure splitting,” *Appl. Phys. Lett.*, vol. 105, p. 251901, 2014.

[19] P. J. Simmonds and M. L. Lee, “Tensile-strained growth on low-index GaAs,” *J. Appl. Phys.*, vol. 112, p. 054313, 2012.

[20] A. Y. Cho, “Growth of III-V semiconductors by molecular beam epitaxy and their properties,” *Thin Solid Films*, vol. 100, pp. 291–317, 1983.

[21] See Supplemental Material at [URL will be inserted by publisher]. .

[22] P. J. Simmonds *et al.*, “Tuning Quantum Dot Luminescence Below the Bulk Band gap Using Tensile Strain,” *ACS Nano*, vol. 7, no. 6, pp. 5017–5023, 2013.

[23] L. He, G. Bester, and A. Zunger, “Strain-induced interfacial hole localization in self-assembled quantum dots: Compressive InAs/GaAs versus tensile InAs/InSb,” *Phys. Rev. B*, vol. 70, no. 23, p. 235316, 2004.

[24] C. I. Cabrera, J. C. Rimada, J. P. Connolly, and L. Hernandez, “Modelling of GaAsP/InGaAs/GaAs strain-balanced multiple-quantum well solar cells,” *J. Appl. Phys.*, vol. 113, p. 024512, 2013.

[25] C. G. Van de Walle, “Band lineups and deformation potentials in the model-solid theory,” *Phys. Rev. B*, vol. 39, no. 3, p. 1871, Jan. 1989.

[26] M. Califano and P. Harrison, “Presentation and experimental validation of a single-band, constant-potential model for self-assembled InAs/GaAs quantum dots,” *Phys. Rev. B*, vol. 61, no. 16, pp. 10959–10965, 2000.

[27] P. Harrison and A. Valavanis, *Quantum Wells, Wires and Dots*, 4th ed. Chichester, UK: John Wiley & Sons, Ltd., 2016.

[28] K. Jacobi, “Atomic structure of InAs quantum dots on GaAs (review),” *Prog. Surf. Sci.*, vol. 71, pp. 185–215, 2003.

[29] C. D. Yerino *et al.*, “Tensile GaAs(111) quantum dashes with tunable luminescence below the bulk band gap,” *Appl. Phys. Lett.*, vol. 105, p. 071912, 2014.

[30] D. V. Forbes, C. Bailey, S. J. Polly, A. Podell, and S. M. Hubbard, “The effect of GaAs capping layer thickness on quantum dot solar cell performance,” *Conf. Rec. IEEE Photovolt. Spec. Conf.*, pp. 3203–3207, 2013.

[31] R. Leon and S. Fafard, “Structural and radiative evolution in quantum dots near the InxGa1/x As/GaAs Stranski-Krastanow transformation,” *Phys. Rev. B*, vol. 58, no. 4, pp. 1726–1729, 1998.

[32] M. Grundmann *et al.*, “Excited states in self-organized InAs/GaAs quantum dots: Theory and experiment,” *Appl. Phys. Lett.*, vol. 68, no. 7, pp. 979–981, 1996.

[33] S. Unsleber *et al.*, “Bulk AlInAs on InP(111) as a novel material system for pure single photon emission,” *Opt. Express*, vol. 24, no. 20, pp. 23198–23206, 2016.

[34] L. Su *et al.*, “The continuum state in photoluminescence of type-II In0.46Al0.54As/Al0.54Ga0.46As quantum dots,” *Appl. Phys. Lett.*, vol. 109, no. 18, p. 183103, 2016.

[35] E. H. Li, “Material parameters of InGaAsP and InAlGaAs systems for use in quantum well structures at low and room temperatures,” *Phys. E*, vol. 5, no. 4, pp. 215–273, 2000.

[36] I. Vurgaftman, J. R. Meyer, and L. R. Ram-Mohan, “Band parameters for III–V compound semiconductors and their alloys,” *J. Appl. Phys.*, vol. 89, no. 11, pp. 5815–5875, 2001.

[37] D. Gammon, E. S. Snow, B. V. Shanabrook, D. S. Katzer, and D. Park, “Fine structure splitting in the optical spectra of single GaAs quantum dots.,” *Phys. Rev. Lett.*, vol. 76, no. 16, pp. 3005–3008, 1996.

[38] J. W. Luo, G. Bester, and A. Zunger, “Atomistic pseudopotential calculations of thickness-fluctuation GaAs quantum dots,” *Phys. Rev. B*, vol. 79, no. 12, p. 125329, 2009.

3.S Chapter 3 Supplemental Material

3.S.1 Experimental Methods

We grow GaAs/InAlAs tensile-strained quantum dot (TSQD) samples on on-axis InP(111)A substrates using solid-source molecular beam epitaxy (MBE). We measure deposition amounts in monolayers (ML), and growth rates in ML/s from reflection high-energy electron diffraction (RHEED) intensity oscillations. We calibrate substrate temperature by comparing thermocouple and pyrometer readings against known changes in the surface reconstruction observed with RHEED. We calculate V/III beam equivalent pressure ratios using a beam flux monitor. All samples have the same structure [***Figure 3.S1 (a)***]: 40 nm $In_{0.53}Ga_{0.47}As$ smoothing buffer (172 nm/hr, 510 °C), 160 nm $In_{0.52}Al_{0.48}As$ bottom barrier, (169 nm/hr, 510 °C), 0 – 4.5 ML embedded GaAs TSQDs for optical analysis (0.075 ML/s, 535 °C, 75 As_4/Ga), 40 nm InAlAs top barrier (172 nm/hr: first 10 nm at 535 ºC, remaining 30 nm at 510 ºC), and 0 – 4.5 ML surface GaAs TSQDs for structural analysis (0.75 ML/s, 535 °C, 75 As_4/Ga).

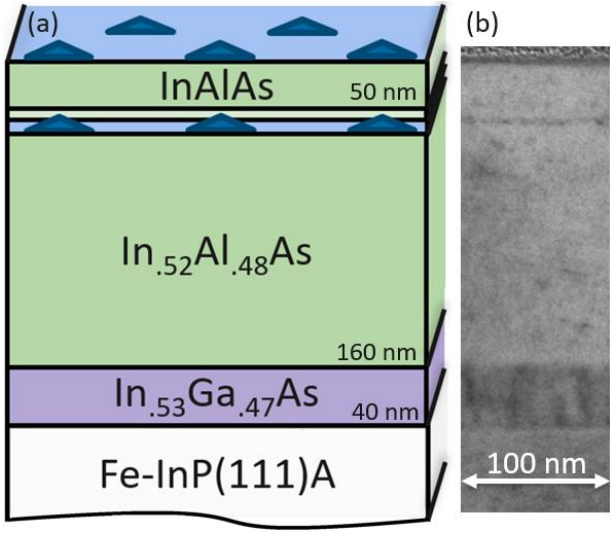

Figure 3.S1: (a) A schematic of the sample heterostructure containing GaAs(111)A TSQDs (blue triangles). (b) XTEM image for comparison showing the expected sample structure.

We image the samples using cross-sectional transmission electron microscopy (XTEM), confirming that they are free from threading dislocations and have good crystal quality [***Figure 3.S1 (b)***]. RHEED shows a streaky 2×2 surface reconstruction during all bulk and TSQD growth.[1]–[4] We confirm the InGaAs and InAlAs layers are lattice-matched to InP using x-ray diffraction. We use a valved arsenic cracker at 600 ºC to supply As_4, for consistency with previous studies of growth on (111)A surfaces.[4]–[7] The InAlAs barriers provide 3.7% tensile lattice-mismatch with the GaAs to drive TSQD self-assembly, while also offering carrier confinement within the TSQDs.[8], [9]

3.S.2 Results and Discussion – AFM: WL Growth Beyond the t_c

Using atomic force microscopy (AFM) data, we calculate the total volume of GaAs in the TSQDs per unit area by multiplying the average TSQD volume by their areal density. We find the total volume of material in the wetting layer (WL) per unit area by subtracting the volume of material in the TSQDs from the amount of GaAs deposited (assuming a Ga sticking coefficient of unity at 535 °C)[10]. For example, 2.5 ML GaAs

deposition corresponds to a volume of 423,613 nm^3 per μm^2, the total volume in the TSQDs is 284 $nm^3/\mu m^2$, and therefore the WL volume is 423,329 $nm^3/\mu m^2$. 4.5 ML GaAs corresponds to a volume of 762,503 $nm^3/\mu m^2$, the total volume in the TSQDs is 4,335 $nm^3/\mu m^2$, and therefore the WL volume is 758,167 $nm^3/\mu m^2$. This data suggests that at 2.5 ML and 4.5 ML GaAs deposition only 0.07% and 0.57% of the GaAs incorporates into the TSQDs, respectively, consistent with the increase in WL volume we measure with TEM [Section 3.4.4].

3.S.3 Results and Discussion – Confirmation of PL Peak Assignments

Excitation-density-dependent PL of our TSQD samples allows us to rule out excited state emission as the origin of the primary peak. As we raise the excitation density from 0.3–3000 W/cm^2, ***Figure 3.S2*** shows the resulting PL emission from the 4.5 ML GaAs TSQD sample.

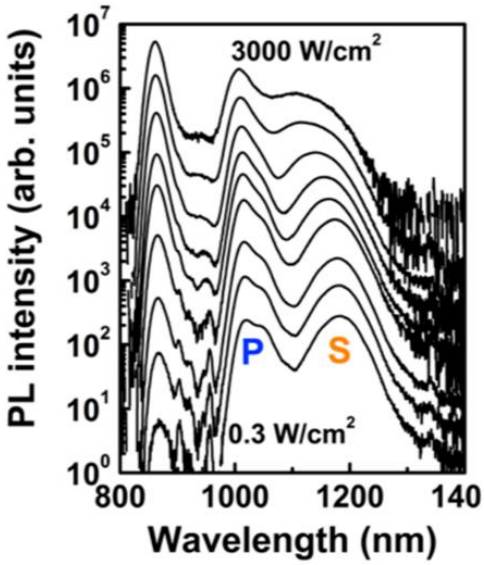

Figure 3.S2: Excitation-density-dependent PL of a 4.5 ML GaAs TSQD sample at 7 K. (a) Change in PL spectra as the excitation intensity is increased from 0.3–3000 W/cm^2. Labels indicate the primary (P) and secondary (S) GaAs peaks.

Note that we chose to use the 4.5 ML sample to illustrate our findings in the interest of clarity, since it has the largest primary-secondary peak separation [Main Text ***Figure 3.3***]. These results are, however, representative of the other TSQD samples. For a sample without WL emission, at low pump powers we would expect to see only a single PL peak corresponding to emission from the TSQD ground states. Increasing the pump power would eventually lead to a saturation of the TSQD ground states, and then appearance of a second peak at shorter wavelength corresponding to emission from the first excited state of the TSQDs. The fact that we see the shorter wavelength primary peak even for excitation densities as low as 0.3 W/cm^2, suggests that this is not emission from an excited state of the TSQDs.

3.S.4 Results and Discussion – XTEM

We produced XTEM samples using a focused ion beam (FIB) lift out method. We did XTEM imaging in a JEOL ARM 200F aberration-corrected microscope operated at an accelerating voltage of 200kV. In all cases, we aligned the samples to a [110] zone-axis.

In bright-field TEM we can directly see that the 4.5 ML GaAs TSQDs are dislocation-free despite the high tensile strain [***Figure 3.S3***].

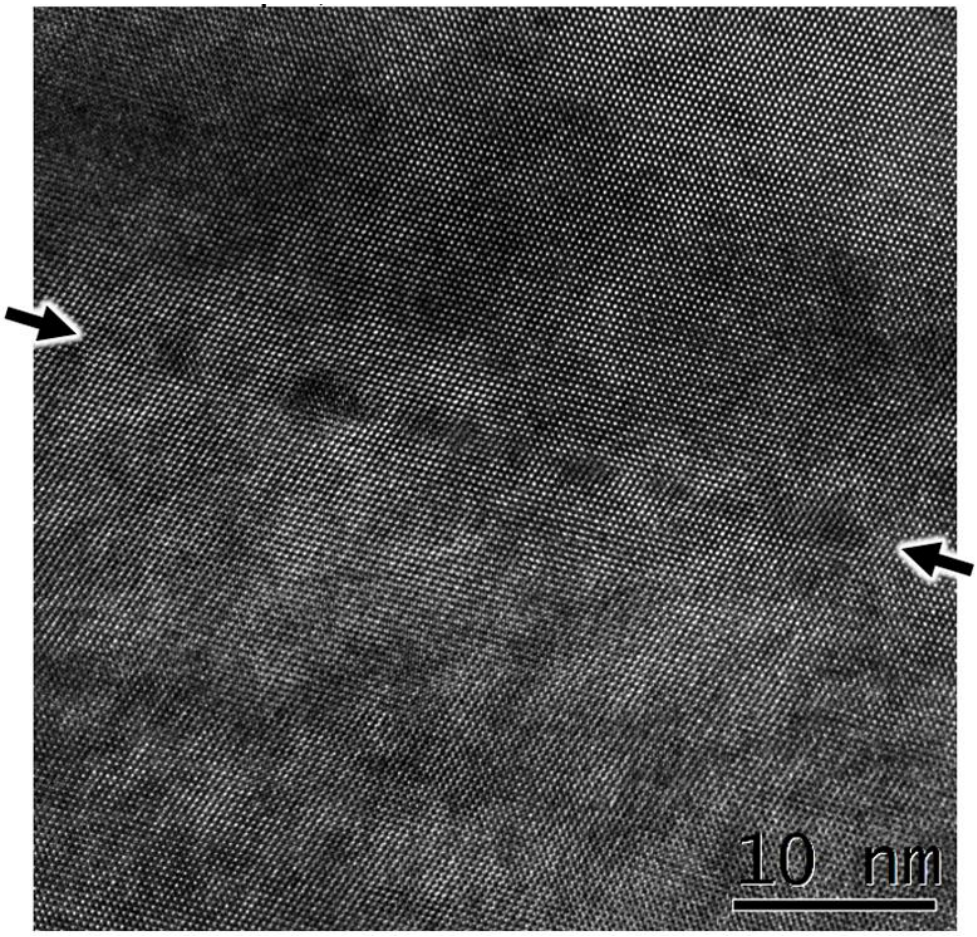

Figure 3.S3: A [110] zone-axis high resolution bright-field TEM image of a 4.5ML sample showing TSQDs visible due to strain contrast. Arrows indicate the layer containing the WL and TSQDs. No crystalline defects are visible in the barriers or TSQDs.

3.S.5 Results and Discussion – TSQD & WL Computational Model

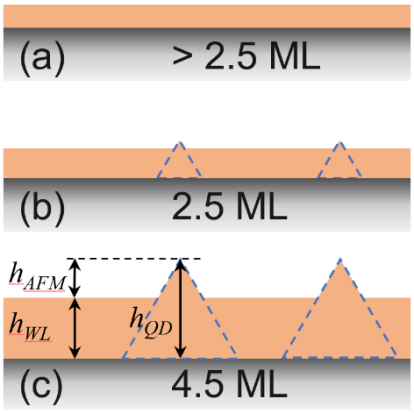

Figure 3.S4: Schematic diagram illustrating the effective TSQD height, as adopted from Wang [11]. For the modified SK growth mode suggested by our experimental and computational results, both h_{AFM} and h_{WL} are variables. (a) Growth begins with the initial formation of a 2D WL, (b) and then at t_c = 2.5 ML, transitions to the self-assembly of 3D TSQDs. (c) Further GaAs deposition leads to a thicker WL, and larger TSQDs.

References

[1] M. R. Fahy, K. Sato, and B. A. Joyce, "Reflection high-energy electron diffraction intensity oscillations during the growth by molecular beam epitaxy of GaAs (111)A," *Appl. Phys. Lett.*, vol. 64, no. 2, pp. 190–192, 1993.

[2] D. J. Chadi, "Atomic and electronic structures of (111), (211), and (311) surfaces of GaAs," *J. Vac. Sci. Technol. B*, vol. 3, no. 4, pp. 1167–1169, 1985.

[3] A. D. Katnani and D. J. Chadi, "Photoemission and theoretical studies of GaAs(111) and (-1-1-1) surfaces: Vacancy models," *Phys. Rev. B*, vol. 31, no. 4, pp. 2554–2556, 1985.

[4] C. F. Schuck *et al.*, "Self-assembly of (111)-oriented tensile-strained quantum dots by molecular beam epitaxy," *J. Vac. Sci. Technol. B*, vol. 36, 031803, 2018.

[5] A. Y. Cho, "Growth of III-V semiconductors by molecular beam epitaxy and their properties," *Thin Solid Films*, vol. 100, pp. 291–317, 1983.

[6] P. J. Simmonds and M. L. Lee, “Tensile-strained growth on low-index GaAs,” *J. Appl. Phys.*, vol. 112, 054313, 2012.

[7] C. D. Yerino *et al.*, “Strain-driven growth of GaAs(111) quantum dots with low fine structure splitting,” *Appl. Phys. Lett.*, vol. 105, 251901, 2014.

[8] C. D. Yerino *et al.*, “Tensile GaAs(111) quantum dashes with tunable luminescence below the bulk band gap,” *Appl. Phys. Lett.*, vol. 105, 071912, 2014.

[9] P. J. Simmonds *et al.*, “Tuning Quantum Dot Luminescence Below the Bulk Band gap Using Tensile Strain,” *ACS Nano*, vol. 7, no. 6, pp. 5017–5023, 2013.

[10] A. Kawaharazuka and Y. Horikoshi, “Behavior of Ga atoms deposited on GaAs (111)B and (111)A surfaces,” *J. Cryst. Growth*, vol. 477, pp. 25–29, 2017.

[11] L. Wang *et al.*, “Self-assembled quantum dots with tunable thickness of the wetting layer: Role of vertical confinement on interlevel spacing,” *Phys. Rev. B*, vol. 80, 085309, 2009.

CHAPTER FOUR: STRUCTURAL AND OPTICAL PROPERTIES OF GAAS(111)A TENSILE-STRAINED QUANTUM DOTS USING AS_2 AND AS_4

Christopher F. Schuck,[1]* Kevin D. Vallejo,[1] Trent Garrett,[2] Qing Yuan,[3] Ying Wang,[3] Baolai Liang,[3] and Paul J. Simmonds[1,2]†

[1] *Micron School of Materials Science & Engineering, Boise State University, Boise, Idaho 83725, USA*

[2] *Department of Physics, Boise State University, Boise, Idaho 83725, USA*

[3] *College of Physics Science & Technology, Hebei University, Baoding 071002, P.R. China*

* E-mail address: christopherschuck@boisestate.edu

† E-mail address: paulsimmonds@boisestate.edu

Pending submission for publication.

Abstract

Using As_2 or As_4 in the growth of GaAs(111)A tensile-strained quantum dots (TSQDs) results in different TSQD structure and photon emission behavior. Control over TSQD structural and optical properties with different arsenic species enhances our ability to tailor TSQD and reveal different nucleation and growth kinetics. At lower temperatures, GaAs(111)A TSQDs grown under As_2 have a triangular base, consistent with GaAs(111)A TSQDs grown under As_4. TSQDs grown with As_2 are also triangular, but with an inverted crystallographic orientation compared to As_4 TSQDs. At higher temperatures, GaAs(111)A TSQDs grown under As_2 have a hexagonal base. We attribute these TSQD morphologies to differences in step edge growth rates as a result of varying arsenic surface concentrations for different substrate temperature and arsenic species. For both the triangular and hexagonal TSQDs, growth under As_2 exhibits higher photon emission intensity compared to As_4-grown TSQDs. Higher emission intensity typically correlates with better crystal quality, which is a critical requirement for efficient optoelectronic devices (including robust photon entanglement). Additionally, the higher symmetry of the hexagonal TSQDs may correlate with lower fine-structure splitting, which may further improve entangled photon emission.

4.1 Introduction and Background

Self-assembled quantum dots (QDs) are widely grown by molecular beam epitaxy (MBE) from compressively strained materials on (100)-oriented surfaces. These QDs exhibit highly tunable structural and optoelectronic properties, high crystalline quality, formation via a single processing step, and easy integration into semiconductor device processing lines [1–4]. The desire to extend these beneficial properties to new research

fronts and device applications has spurred interest in extending the range of materials systems from which it is possible to synthesize QDs. Example materials systems include (111)-oriented QDs, which have a low fine structure splitting (FSS) for quantum information applications [5–7], and tensile-strained QDs (TSQDs), which offer band structure engineering capabilities for long wavelength optoelectronics and a potential route towards direct band gap Ge [8–12].

GaAs(111)A TSQDs are the first optically active materials system to combine the benefit of epitaxial self-assembly, (111)-orientation, and tensile strain [12]. They are structurally and optically tunable, dislocation-free, exhibit low FSS, and have a tunably reducible bandgap [11,13,14]. To outline the full capabilities of this promising new materials system, we recently presented a comprehensive study on the customization and optimization of GaAs(111)A TSQD properties via several MBE growth parameters (deposition amount in monolayers (MLs), substrate temperature (T_{SUB}), growth rate, and group V/III flux) [13]. However, all (111) TSQDs were grown using tetrameric arsenic (As_4) for consistency with previous (111) growths [11,12,14,15], since much of the original growth optimization on (111) surfaces was done before the advent of valved-cracker sources for arsenic. However, with the ready availability of arsenic cracker sources, As_2 is now used more widely than As_4. We therefore wanted to explore the impact of these two arsenic species on the growth and properties of GaAs/InAlAs(111)A TSQDs.

Researchers have shown that using As_2 instead of As_4 during the MBE growth of various (100)-oriented bulk materials improves room temperature PL emission intensity [16,17], can widen [18] or narrow [19] PL linewidth, reduces non-radiative interface

recombination [20] and the occurrence of deep electron traps [21], reduces auto-compensation of amphoteric dopants like Si [21,22], and can roughen [23] or smooth [24] surface morphology. With (110) bulk GaAs, As_2 provides a larger growth-parameter phase-space [24]. With (111)A bulk GaAs, the As_2 incorporation coefficient (S_{As2}) is low compared to (100), while S_{As4} is even lower, and under typical growth conditions, the incorporation coefficient of both arsenic species decreases significantly with increasing T_{SUB} [22]. These observations are consistent with the experimentally established requirements for a high V/III flux ratio on (111)A surfaces [11–14,22,25]. PL emission intensity from (100)-oriented QDs is also strongly influenced by choice of arsenic species. [18,26-, QDs that are more isotropic (compared to elongated QDs with As_4) [18,26,27], and varying sizes and areal densities [18,26,29].

Clearly therefore, the use of As_2 versus As_4 is an important and dynamic growth variable. Here we present the first use of As_2 to grow (111) TSQDs and compare its use to TSQDs grown with As_4. This simple adjustment results in different nucleation and growth kinetics, and as a result, a greater ability to tailor TSQD structure, improved PL emission, and the option to select between triangular and hexagonal TSQDs.

4.2 Experiments and Methods

We use solid source MBE to grow GaAs(111)A TSQDs inside $In_{0.52}Al_{0.48}As$ barriers grown atop an $In_{0.53}Ga_{0.47}As$ smoothing buffer on semi-insulating Fe-doped InP(111)A substrates. We have previously reported the optimal growth parameters for InAlAs and InGaAs on InP(111)A [13,25]. For the TSQDs, the GaAs deposition rate is 0.075 ML/sec, with a beam equivalent pressure (BEP) As:Ga ratio of 75. This research began with a preliminary As_2 GaAs growth at 3.0 ML deposition and 485 ºC T_{SUB}, which

suggested the benefits of using As_2 for TSQD growth. We followed up this experiment using growth conditions more favorable for producing high quality TSQDs [13]. We grew three pairs of 3.5 ML GaAs(111)A TSQD samples using As_2 versus As_4 at increasing T_{SUB} (535 ºC, 560C, and 570 ºC). Samples include a layer of GaAs TSQDs buried beneath an InAlAs top barrier for optical analysis via low-temperature PL (7 K, 80 W/cm^2), and a surface layer of TSQDs for structural analysis with tapping-mode atomic force microscopy (AFM).

4.3 Structural Analysis, Results and Discussion

Using AFM, we analyze the structural characteristics of the WL surface and TSQDs. Step edges and other morphological features of the epitaxial surface can act as adatom diffusion barriers and nucleation sites, potentially affecting QD areal density and causing anisotropy in QD shape and surface distribution [3,30]. Depending on the applications, these effects may or may not be desirable. For example, a low (111)A surface roughness would be preferable for growing TSQDs for entangled photon emission, both to maximize QD uniformity and symmetry, and to minimize areal density to simplify single QD analysis.

We use AFM to analyze TSQD average height, average diameter, areal density, and morphology. Regardless of the arsenic species used, all TSQDs exhibit a low average height (< 1.2 nm), wide diameter (> 60 nm), and low areal density ($< 5 \times 10^{-8}$ cm^{-2}) compared to conventional (100) QDs[***Figure 4.1***], consistent with previous research [13]. ***Figure 4.1 (a)*** shows that TSQDs grown under As_4 are triangular in shape, consistent with those seen in previous GaAs(111)A TSQD studies [12,13]. In contrast, TSQDs grown with As_2 are hexagonal in shape [***Figure 4.1 (c)***]. To better visualize these new

hexagonal nanostructures, we used AFM amplitude analysis, which provides higher contrast for changes in surface height, for example at step edges and QD facets [***Figure 4.1 (b,d)***].

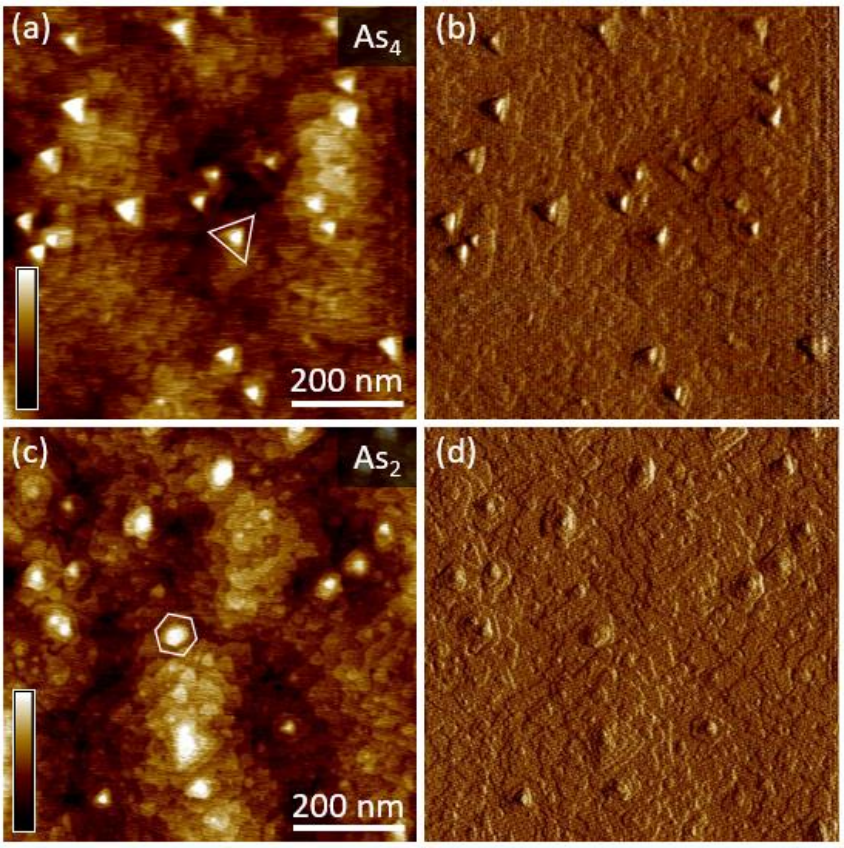

Figure 4.1: AFM images of GaAs (111)A TSQDs (25 μm^2, 2 nm height bar). (a, b) show 3 ML GaAs TSQDs deposited under As_4. (c, d) show 4.5 ML GaAs TSQDs deposited under As_2. All other growth conditions are the same (485 °C T_{SUB}, 0.075 ML/sec growth rate, 75 V/III). AFM height data (a, c) provides information on QD size, shape, and spacing. AFM amplitude (error) information (b, d) provides better visualization of QD edges. Using As_4 produces triangular TSQDs (a, b), while using As_2 produces hexagonal TSQDs (c, d).

Varying T_{SUB} from 535 ºC to 570 ºC does not significantly change average TSQD height for either the As_4 or As_2 samples [***Figure 4.2 (a)***]. For TSQDs grown with As_4, average diameter is essentially independent of T_{SUB}. However, the average diameter of

TSQDs grown with As_2 increases monotonically with T_{SUB} [***Figure 4.2 (b)***]. We measure diameter for both As_2 and As_4 TSQDs as twice the distance from center to vertex.

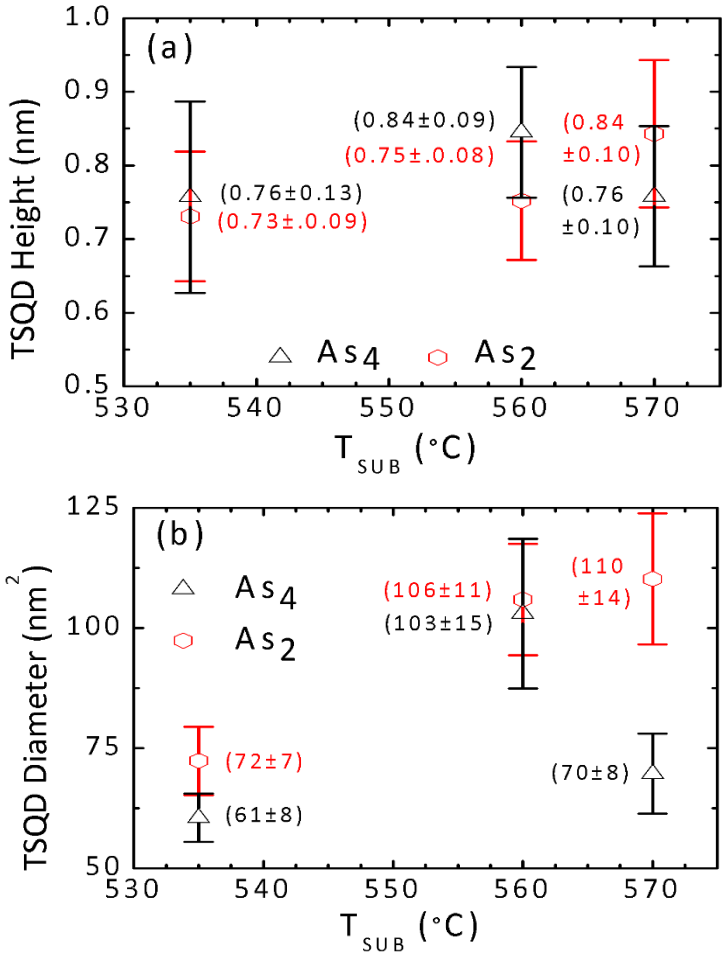

Figure 4.2: Scatter plots of the average (a) height and (b) diameter of TSQDs grown with As_4 (black) and As_2 (red), as a function of substrate temperature (error bars represent one standard deviations). The only statistically significant change is in As_2 TSQD diameter, which increases with increasing substrate temperature, such that the errors bars

That the average height and diameter, and therefore volume, of TSQDs grown with As_4 has no statistically significant variation with increasing T_{SUB} is consistent with previous studies where we postulated an equilibrium TSQD volume [13]. In contrast, As_2 TSQDs continuously increase in diameter with increasing T_{SUB}, such that the As_2 and As_4 diameter error bars no longer overlap by 570 °C. This increase in QD diameter with T_{SUB}

is consistent with conventional compressively strained QD self-assembly which are also grown with As_2 [1,31,32]. Increased T_{SUB} increases adatom mean diffusion length, promoting increased adatom attachment to existing islands rather than the nucleation of new QDs. The result is larger average QD size and lower areal density [33].

A possible explanation for this difference in TSQD self-assembly with As_4 and As_2 is found in the disparity between the incorporation coefficients of these two species. The GaAs(111)A surface has arsenic incorporation coefficients (S_{As}) that decrease with increased T_{SUB}. At low T_{SUB}, As_2 and As_4 have S_{As} of 1 and 0.5, respectively [17,22,34]. This is why a high As:Ga flux ratio is necessary for good surface quality at typical growth temperatures [22,25]. Increasing T_{SUB} on (111) surfaces reduces the arsenic surface population, which increases Ga adatom diffusion lengths and therefore should result in increased QD diameter. The combination of these factors is responsible for a T_{SUB} dependent reduction in roughness [see ***Figure 4.4***]. This arsenic incorporation related effect is more pronounced with As_4. On all low index GaAs surfaces, the dissociation kinetics of As_4 combined with the pairwise Ga attachment process result in desorption of excess arsenic [22,29,34,35]. Therefore, an increase in T_{SUB} results in a larger reduction of the incorporation coefficient of As_4 than of As_2 [***Table 4.1***] [22,34].

Table 4.1: (111)A surface arsenic incorporation coefficients for As_4 and As_2 at different substrate temperatures, per Tok et al. [22]. S_{As} decreases with increased substrate temperature for both species. The S_{As} of As_4 is roughly half that of As_2, regardless of temperature.

S_{As} of:	280 °C	470 °C	535 °C	560 °C	570 °C
As_4	0.5	2.4	0.11	0.09	0.08
As_2	1.0	5.0	0.25	0.19	0.18

It is a reasonable assumption that the higher incorporation of As_2 on the (111)A surface provides a high enough arsenic surface adatom population to facilitate the

established kinetic mechanisms that result in larger QD size (and lower areal density) with higher T_{SUB} [1,31,32]. In contrast, the lower incorporation of As_4 could more quickly result in a Ga-rich surface reconstruction. Certainly, previous reports show bulk As_4 GaAs(111)A transitioning to a Ga-rich surface when heated above 550 ºC [36]. The Ga-vacancy reconstruction has a negative chemical potential energy, $-\Delta\mu$, [37] and therefore results in a higher free energy of nucleation, $\Delta G(f)$. A sufficiently high $\Delta G(f)$ will completely inhibit QD formation [38]. Comparison studies in other materials systems have also reported As_2 leading to larger QD size than As_4 [18,27,28].

T_{SUB} has a non-linear effect on TSQD areal density for both arsenic species (***Figure 4.3***).

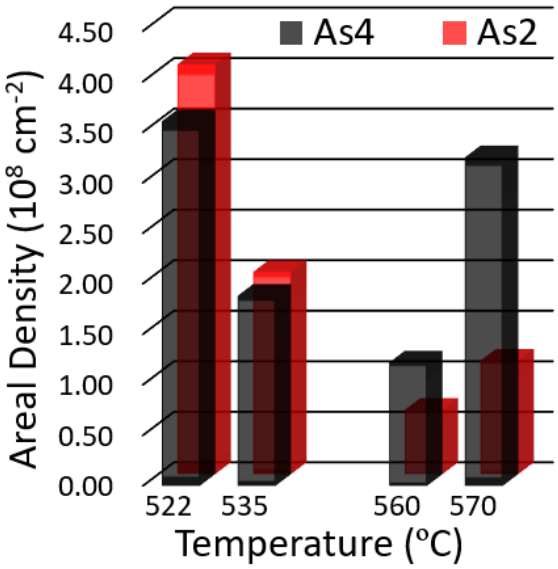

Figure 4.3: The areal density of GaAs(111)A TSQDs grown with As_4 (black) and As_2 GaAs (red) as a function of substrate temperature. For both arsenic species, TSQD areal density decreases as we increase T_{SUB} from 522 ºC to 560 ºC, but then increases for T_{SUB} = 570°C.

TSQD areal density decreases at a similar rate for both arsenic species as we raise T_{SUB} from 522 °C (***Figure 4.3***). However, at 570 ºC, we see a threefold *increase* in the

areal density of TSQDs grown with As_4, and twofold increase for TSQDs grown with As_2. Combining these areal density values with the data in ***Figure 4.2*** into a simple material conservation calculation (areal density times average TSQD volume) reveals an increase in total QD material with increasing T_{SUB}. Raising T_{SUB} from 535 ºC to 570 ºC, increases the total material in As_4 TSQDs from 1048 – 2588 $nm^3\mu m^{-2}$, and for As_2 GaAs TSQDs, from 1552 – 2415 $nm^3\mu m^{-2}$. Since we are depositing nominally the same amount of GaAs on all samples (3.5 ML), these results suggest that more of this material is able to incorporate into the TSQDs as we raise T_{SUB}, regardless of whether we use As_4 or As_2.

Most strain-driven QDs form by the Stranski-Krastanov (SK) growth mode, where the initial formation of a planar wetting layer (WL) transitions to QD self-assembly once some critical thickness is reached. Typically, the WL thickness becomes pinned at this critical thickness and all subsequent material deposited goes into the QDs [38–40]. Therefore, for these canonical QD systems, conservation of mass dictates the well-established fact that for the same deposition amount, all changes in average QD size and areal density are inversely proportional. We have shown previously however that GaAs(111)A TSQDs grow by an anomalous SK mode, whereby the WL continues to grow even after TSQDs formation begins [41]. This anomalous SK growth therefore has a WL that actively adsorbs and desorbs surface adatoms, effectively decoupling the established interdependence of QD size and areal density.

It is possible that the disparity we observe between GaAs(111) TSQD size and areal density variation with increased T_{SUB} could be due to a net loss of material due to low arsenic incorporation coefficients on this surface. This possibility would not however account for the spike in areal densities at 570 ºC. In addition, we see no evidence of an

excess of surface Ga, for example in the form of droplets that might be expected if a lack of arsenic led to the loss of stoichiometry. The more likely possibility is therefore the transfer of adatoms from the anomalous SK WL (Chapter 3) to the TSQDs at high T_{SUB}. Additional kinetic parameters may also play a role, such as differences in reactivity and surface mobility between arsenic species.

We also analyzed the GaAs WL surface using AFM. The As_2 GaAs surface is visibly rougher (***Figure 4.1***). We measure surface roughness on all samples by performing a root mean square surface roughness calculation on 25 μm^2 AFM images. We found that GaAs TSQDs samples grown with As_2 exhibit higher surface roughness than As_4 grown samples (***Figure 4.4***), consistent with research on the (111)B surface [23]. Increasing T_{SUB} decreases the surface roughness for both arsenic species, although it has more impact on As_2, such that surface roughness is comparable by 570 ºC (***Figure 4.4***).

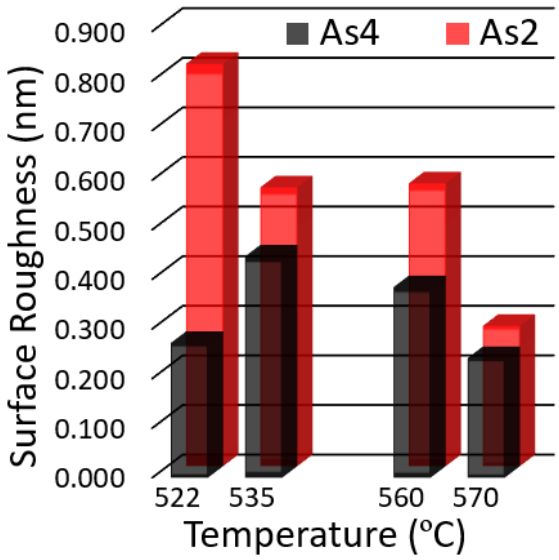

Figure 4.4: Surface roughness of the GaAs(111)A wetting layers grown under As_4 (black) and As_2 (red) at different substrate temperatures. For the entire T_{SUB} range studied, using As_2 results in higher surface roughness, although the difference decreases at high substrate temperature.

Smooth surfaces are typically attained during epitaxial growth by annealing or decreasing arrival rate (flux) of group III material [42,43]. Both mechanisms increase surface diffusion of adatoms and thereby allow preferential, low-energy binding along growing step edges, rather than higher-energy nucleation of new layers [38,42]. Likewise, the higher incorporation coefficient in As_2 than in As_4 results in a lower gallium diffusion rate, and thus promotes rougher surfaces [22,34].

4.4 Optical Analysis, Results and Discussion

All As_2 versus As_4 TSQD PL spectral profiles show significantly higher GaAs WL and TSQD emission intensity (***Figure 4.5***). We used a low laser excitation power of 80 W/cm^2 to provide distinction between the WL and TSQDs. Peak emission intensities occur at 941 nm – 975 nm for the WL, 1009-1040 nm for the TSQDs, and 856 nm for the InAlAs barrier (***Figure 4.5***). At 535 ºC, using As_2 compared to As_4 increases WL intensity 4× and TSQD intensity 8× (***Figure 4.5 (a)***). At 560 ºC, using As_2 increases WL intensity 3× and TSQD intensity 2× (***Figure 4.5 (b)***). At 570 ºC, using As_2 compared to As_4 increases WL intensity 4× but does not increase TSQD intensity (***Figure 4.5 (c)***).

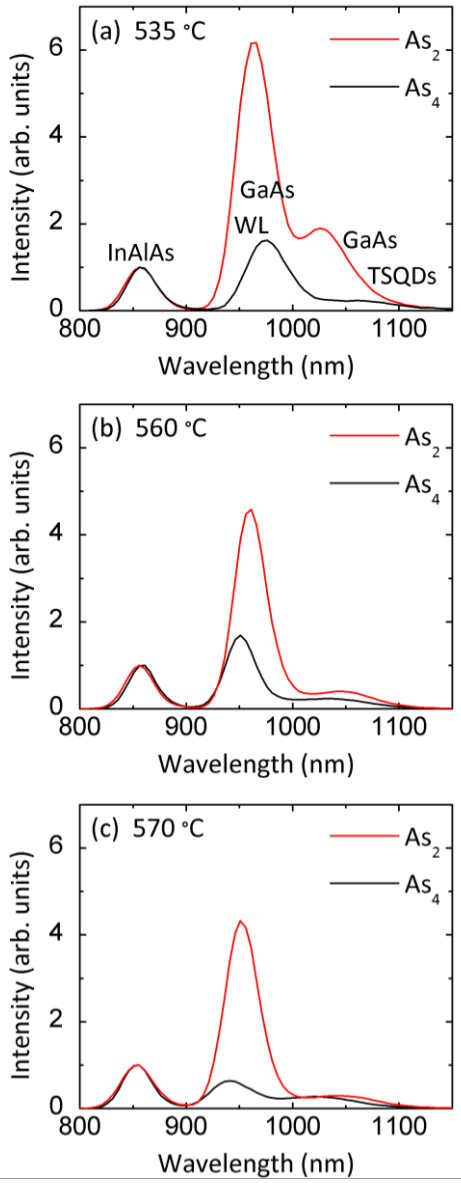

Figure 4.5: 7 K PL emission spectra of GaAs(111)A TSQDs samples growth with As_2 (red) and As_4 (black) at various substrate temperatures. At 535 °C (a), As_2 samples have much higher emission intensities. With increasing temperature (b, c), As_2 WL emission intensity remains higher than for As_4, though TSQD intensities become similar. The observed blue shift in both the As4 WL and TSQD peak is consistent with a lower As4 incorporation rate [Table 4.1] resulting in a smaller WL thickness and TSQD diameter [Figure 4.2] than with As_2. Excitation density is 80 W/cm$_2$. Spectral intensities are normalized the bulk InAlAs peak.

While the TSQD emission peaks for As_2 and As_4 are comparable above 560 ºC, the intensity of this peak is a function of TSQD areal density, which is much lower for

the As_2 TSQDs grown at high T_{SUB} [***Figure 4.3***]. Therefore to study TSQD quality, the emission efficiency (the integrated area of the TSQD PL peak, divided by the areal density) is a more useful parameter [13]. Both WL intensity and TSQD emission efficiency measurements demonstrate that the use of As_2 during TSQD growth significantly improves the optical quality of the GaAs. Specifically, the use of As_2 provides between 3–7× increase in WL emission intensity and 3–4× increase in TSQD emission efficiency (***Figure 4.6***).

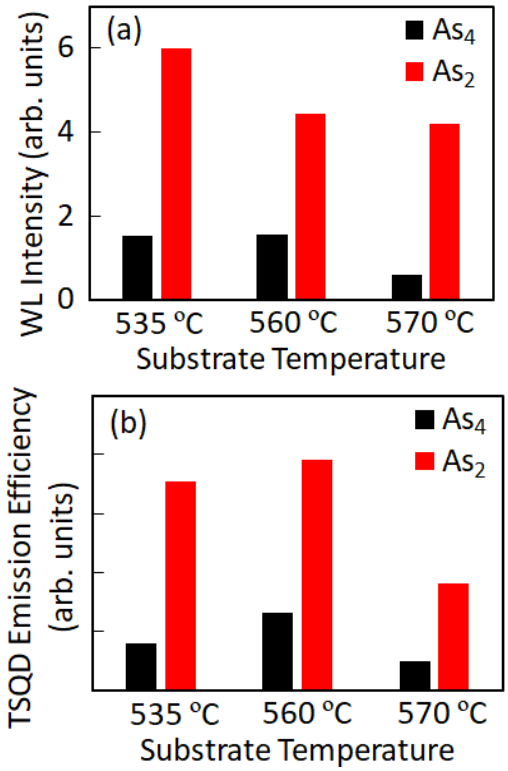

Figure 4.6: Plots of GaAs(111)A WL emission intensity (a) and TSQDs emission efficiency (b) with increasing substrate temperature. WL intensity and TSQD emission efficiency are higher consistently higher with As_2 than As_4.

Although all samples show decreased optical quality by T_{SUB} = 570 °C, the effect is more prominent for TSQDs grown with As_4. This effect may be due to the fact that increasing T_{SUB} and using As_4 both contribute to a reduction in the arsenic incorporation

coefficient [22,24]. If the surface population of arsenic adatoms is too low during growth, the quality of the epitaxial material will suffer [11–14,22,25].

The spectral linewidth, defined as the full-width at half-maximum (FWHM) of the PL peaks, is narrower for samples grown with As_2 at lower T_{SUB}, though wider by 570 ºC. The increase in emission FWHM of As_2 grown TSQDs is consistent with their increase in standard deviation of their average diameter [***Figure 4.2***, ***Figure 4.6***].

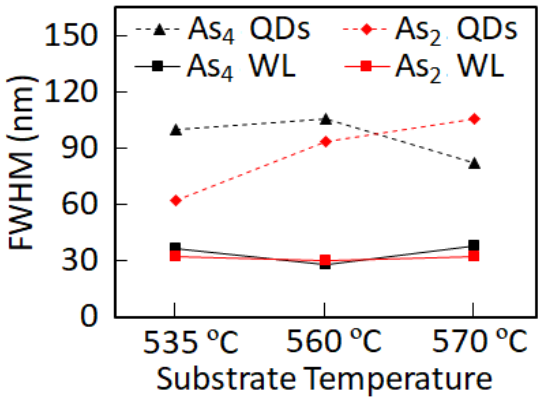

Figure 4.7: Plot of the spectral emission FWHM of the GaAs(111) TSQD WL and TSQDs with increasing substrate temperature. FHWM of As_2 TSQDs (red dashed line) compared to As_4 TSQDs (black dashed line) is lower at 535 ºC, then become higher with increased T_{SUB}. WL emission FWHM for both As_2 (red solid line) and As_4 (black solid line) do not vary.

4.5 GaAs TSQD Surface Orientation and Symmetry

While a broader distribution of QD sizes increases the spectral emission linewidth, higher asymmetry of individual QDs increases their FSS [5,6]. The high piezoelectric symmetry of the (111)A surface [5,6] has spurred renewed research into (111)-oriented QDs for quantum information applications [7,12,45,46]. Higher *structural* symmetry also reduces FSS [5,6,44,47], for example in triangular (111) TSQDs compared to elliptical (100) QDs [1,48].

Using As_2 at higher T_{SUB} results in GaAs(111)A TSQDs with a more symmetric hexagonal shape (***Figure 4.1***, ***Figure 4.8***), which we therefore anticipate should further reduce FSS. Using As_2 at lower T_{SUB} still results in triangular TSQDs, though with an inverted orientation compared to As_4 TSQDs (***Figure 4.8***).

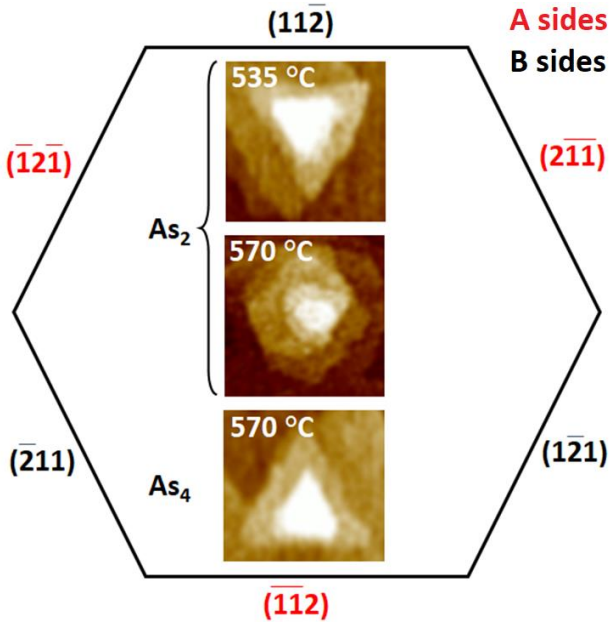

Figure 4.8: AFM images of the various GaAs(111)A TSQD morphologies with different substrate temperature and arsenic species combinations. Overlaid is a schematic of the $\{2\underline{11}\}$ planes relative to the possible TSQD step edge orientations.

As_4 GaAs TSQDs have "A steps" which are parallel to the (1$\underline{21}$), (2$\underline{11}$), and (1$\underline{12}$) planes. As_2 GaAs TSQDs have "B steps" which are parallel to the (1$\underline{12}$), (1$\underline{21}$), and (2$\underline{11}$) planes. Hexagonal TSQDs have sides along the entire family of $\{2\underline{11}\}$ planes. Similar nanostructure shape transitions have been observed with GaAs(111) QDs grown by droplet epitaxy (DE) and Pt/Pt(111) islands grown by MBE [49,50]. Jo *et al*. reported on a shape transition from hexagonal QDs to a B step triangular QD with increasing T_{SUB} [49]. Their B step QD morphology is due to the A step having a higher binding energy and lower adatom diffusion rate, due to its two dangling bonds compared the B step's one

dangling bond [49,50]. They attribute their hexagonal QDs to a DE specific mechanism, a diffusion-limited regime at low T_{SUB} in which Ga diffuses from the Ga droplet slower than the step edge incorporation rate.

With GaAs(111)A TSQDs, we also see increased A step growth (decreasing its length) with higher T_{SUB} (***Table 4.2***).

Table 4.2: TSQD step-edge orientations (A-sided, hexagonal, B-sided) as a function of arsenic species and substrate growth temperature. A-sided triangular TSQDs are favored at lower temperatures using As_2, which transition to hexagonal TSQDs at higher temperature As_2, then to B-sided triangular TSQDs a higher temperature As_4. We did not categorize TSQDs that were not clearly triangular or hexagonal, therefore the percentages below do not sum to 100%.

As-species and Growth Temperature	A-sided triangles (%)	Hexagons (%)	B-sided triangles (%)
As_2, 535 °C	52	28	0
As_2, 570 °C	8	69	0
As_4, 570 °C	0	14	68

However, if our hexagonal TSQDs are a temperature-dependent transition state towards B step TSQDs we cannot increase T_{SUB} to confirm this. At around 580 ºC, indium begins to desorb from the epitaxial surface, which would degrade our InAlAs barriers. However, Jo *et al*. observed the appearance of B step QDs by T_{SUB} 500 ºC. The growth process specific to DE makes their QD environment inherently Ga rich, and under Ga rich conditions the B step (110) microfacet has a lower surface energy than both the A step (100) microfacet and the (111)A surface [49,51]. In contrast, under the As rich conditions we use in traditional MBE, the A step (100) microfacet has the lowest surface energy [49,51]. With the exception of the high arsenic overpressure regime, these surface energies are a function of the chemical potential energy of the epilayer and, therefore, the amount of arsenic on the surface. The variable arsenic incorporation coefficient could hence be the mechanism that favors A step or B step growth during GaAs(111)A TSQD

self-assembly. With the already low arsenic incorporation (***Table 4.1***), the active adsorption of arsenic by growing TSQD surfaces could be sufficient to create a locally Ga rich environment. This mechanism would lead to TSQDs that have B steps if S_{As} is high and A steps if S_{As} is low. Indeed, our B step TSQDs that form under As_4 have the lowest S_{As} (0.08-0.11), our hexagonal TSQDs that form under As_2 at high T_{SUB} have intermediate S_{As} (0.18 and 0.19), and our A step TSQDs that form under As_2 at low T_{SUB} have highest S_{As} (0.25) [22]. Additionally, the A step islands seen in bulk GaAs(111)A growth [29] also have growth conditions (As_2, 480 ºC) that correspond to a high S_{As} (0.48). Therefore, the three different TSQD morphologies we observe are consistent with a simple model where changes in A and B step edge growth rates occur as a function of arsenic surface concentration (and therefore arsenic species and substrate temperature).

4.6 Conclusion

GaAs(111)A TSQDs grown using As_2 and As_4 exhibit different morphology, diameter, areal density, and optical emission quality. These parameters are explored by direct comparison between samples, and as sample series' with increasing substrate temperature.

Both As_4 and As_2 TSQDs have similar height, which does not change as we increase T_{SUB}. As_4 TSQDs have a constant diameter with increasing T_{SUB}, while As_2 TSQD diameter increases with increasing T_{SUB}. Areal density in both TSQD arsenic species decreases comparably with increasing T_{SUB} until 570 ºC, at which point areal density increases significantly in the As_4 TSQDs and only slightly in the As_2 TSQDs. The behavior of TSQDs grown with As_2 is consistent with typical QD growth kinetics, while the behavior of TSQDs grown with As_4 is attributed to the low arsenic incorporation of

As_4 at our growth temperatures. The increase in areal density at 570 ºC is likely due to the anomalous SK growth mode of GaAs(111)A TSQDs. The results of this structural analysis provide a greater ability to tailor TSQD and provide insight into the nucleation and growth kinetics of GaAs(111)A TSQDs grown with As_2 and As_4.

In all sample sets, As_2 provides better WL and TSQD optical quality, indicated by higher WL emission intensity and TSQD emission efficiency. Higher emission intensity typically correlates with better crystal quality, which is critical for efficient optoelectronic devices. Additionally, the higher symmetry of the hexagonal TSQDs may correlate with lower FSS, which may further improve entangled photon emission.

Finally, GaAs(111)A has three distinct morphologies. High symmetry hexagonal TSQDs and the A and B step triangular TSQDs occur on a spectrum of varying arsenic incorporation. The growth rates of A and B steps, which depends on their surface energies and, therefore, the arsenic surface population, are a potential mechanism for these different morphologies.

References

[1] B.A. Joyce, D.D. Vvedensky, Self-organized growth on GaAs surfaces, Mater. Sci. Eng. R. 46 (2004) 127–176. doi:10.1016/j.mser.2004.10.001.

[2] S. Franchi, G. Trevisi, L. Seravalli, P. Frigeri, Quantum dot nanostructures and molecular beam epitaxy, Prog. Cryst. Growth Charact. Mater. 47 (2003) 166–195. doi:10.1016/j.pcrysgrow.2005.01.002.

[3] F. Ratto, F. Rosei, Order and disorder in the heteroepitaxy of semiconductor nanostructures, Mater. Sci. Eng. R. 70 (2010) 243–264. doi:10.1016/j.mser.2010.06.011.

[4] A.P. Alivasatos, Semiconductor Crystals, Nanocrystals, and Quantum Dots, Science (80-.). 271 (1996) 933–937. http://dx.doi.org/10.1126/science.271.5251.933.

[5] A. Schliwa, M. Winkelnkemper, A. Lochmann, E. Stock, D. Bimberg, In(Ga)As/GaAs quantum dots grown on a (111) surface as ideal sources of entangled photon pairs, Phys. Rev. B. 80 (2009) 161307. doi:10.1103/PhysRevB.80.161307.

[6] S. Schulz, M.A. Caro, E.P. O'Reilly, O. Marquardt, Symmetry-adapted calculations of strain and polarization fields in (111)-oriented zinc-blende quantum dots, Phys. Rev. B. 84 (2011) 125312. doi:10.1103/PhysRevB.84.125312.

[7] G. Juska, E. Murray, V. Dimastrodonato, T.H. Chung, S. Moroni, A. Gocalinska, E. Pelucchi, Conditions for entangled photon emission from (111) B site-controlled pyramidal quantum dots, J. Appl. Phys. 117 (2015) 134302.

[8] G. Signorello, E. Lörtscher, P.A. Khomyakov, S. Karg, D.L. Dheeraj, B. Gotsmann, H. Weman, H. Riel, Inducing a direct-to-pseudodirect bandgap transition in wurtzite GaAs nanowires with uniaxial stress., Nat. Commun. 5 (2014) 3655. doi:10.1038/ncomms4655.

[9] M. El Kurdi, G. Fishman, Ś. Sauvage, P. Boucaud, Band structure and optical gain of tensile-strained germanium based on a 30 band kp formalism, J. Appl. Phys. 107 (2010) 013710. doi:10.1063/1.3279307.

[10] X. Li, K. Maute, M.L. Dunn, R. Yang, Strain effects on the thermal conductivity of nanostructures, Phys. Rev. B. 81 (2010) 245318. http://dx.doi.org/10.1103/PhysRevB.81.245318.

[11] P.J. Simmonds, M.L. Lee, Tensile-strained growth on low-index GaAs, J. Appl. Phys. 112 (2012) 054313. doi:10.1063/1.4749407.

[12] C.D. Yerino, P.J. Simmonds, B. Liang, D. Jung, C. Schneider, S. Unsleber, M. Vo, D.L. Huffaker, S. Höfling, M. Kamp, M.L. Lee, Strain-driven growth of

GaAs(111) quantum dots with low fine structure splitting, Appl. Phys. Lett. 105 (2014) 251901. doi:10.1063/1.4904944.

[13] C.F. Schuck, R.A. McCown, A. Hush, A. Mello, S. Roy, J.W. Spinuzzi, P.J. Simmonds, Self-assembly of (111)-oriented tensile-strained quantum dots by molecular beam epitaxy, J. Vac. Sci. Technol. B. 36 (2018) 031803. doi:10.1116/1.5018002.

[14] P.J. Simmonds, M.L. Lee, Self-assembly on (111)-oriented III-V surfaces, Appl. Phys. Lett. 99 (2011) 123111. doi:10.1063/1.3640501.

[15] A.Y. Cho, Growth of III-V semiconductors by molecular beam epitaxy and their properties, Thin Solid Films. 100 (1983) 291–317. doi:10.1016/0040-6090(83)90154-2.

[16] W.T. Tsang, J.A. Ditzenberger, N.A. Olsson, Improvement of photoluminescence of molecular beam epitaxially grown GaxAlyIn1-x-yAs by using an As2 molecular beam, IEEE Electron Device Lett. 4 (2008) 275–277. doi:10.1109/edl.1983.25731.

[17] Z.B. Hao, Z.Y. Ren, W.P. Guo, Y. Luo, Studies on incorporation of As2 and As4 in III-V compound semiconductors with two group V elements grown by molecular beam epitaxy, J. Cryst. Growth. 224 (2001) 224–229. doi:10.1016/S0022-0248(01)01019-3.

[18] B. Liang, Q. Yuan, L. Su, Y. Wang, Y. Guo, S. Wang, G. Fu, E. Marega, Y.I. Mazur, M.E. Ware, G. Salamo, Correlation between photoluminescence and morphology for single layer self-assembled InGaAs/GaAs quantum dots, Opt. Express. 26 (2018) 23107. doi:10.1364/oe.26.023107.

[19] C. Gilfert, E.M. Pavelescu, J.P. Reithmaier, Influence of the As2/As4 growth modes on the formation of quantum dot-like InAs islands grown on InAlGaAs/InP (100), Appl. Phys. Lett. 96 (2010) 5–8. doi:10.1063/1.3428956.

[20] G. Duggan, P. Dawson, C. Foxon, G.W. T Hooft, The effect of arsenic species on the minority carrier properties of (AlGa)As-GaAs double heterostructures grown

by MBE, J. Phys. Colloq. 43 (1982) C5-129-C5-134. doi:10.1051/jphyscol:1982516.

[21] H. Jung, H. Künzel, K. Ploog, Infuence of arsenic species on electrical and optical properties of MBE grown GaAs, J. Phys. Colloq. 43 (1982) C5-135-C5-143. doi:10.1051/jphyscol:1982517.

[22] E.S. Tok, T.S. Jones, J.H. Neave, J. Zhang, B.A. Joyce, Is the arsenic incorporation kinetics important when growing GaAs(001), (110), and (111)A films?, Appl. Phys. Lett. 71 (1997) 3278–3280. doi:10.1063/1.120312.

[23] T. Hayakawa, M. Nagai, M. Morishima, H. Horie, K. Matsumoto, Molecular beam epitaxial growth of AlxGa1-xAs (x=0.2-0.7) on (111)B-GaAs using As4 and As2, Appl. Phys. Lett. 59 (1991) 2287–2289. doi:10.1063/1.106045.

[24] D.M. Holmes, J.G. Belk, J.L. Sudijono, J.H. Neave, T.S. Jones, B.A. Joyce, Differences between As2 and As4 in the homoepitaxial growth of GaAs(110) by molecular beam epitaxy, Appl. Phys. Lett. 67 (1995) 2848. doi:10.1063/1.114805.

[25] C.D. Yerino, B. Liang, D.L. Huffaker, P.J. Simmonds, M.L. Lee, Review Article: Molecular beam epitaxy of lattice-matched InAlAs and InGaAs layers on InP(111)A, (111)B, and (110), J. Vac. Sci. Technol. B. 35 (2017) 010801. doi:10.1116/1.4972049.

[26] T. Sugaya, T. Amano, K. Komori, Improved optical properties of InAs quantum dots grown with an As2 source using molecular beam epitaxy, J. Appl. Phys. 100 (2006) 063107. doi:10.1063/1.2352809.

[27] S. Suraprapapich, S. Panyakeow, C.W. Tu, Effect of arsenic species on the formation of (Ga)InAs nanostructures after partial capping and regrowth, Appl. Phys. Lett. 90 (2007) 183112. doi:10.1063/1.2735676.

[28] T. Sugaya, S. Furue, T. Amano, K. Komori, InGaAs quantum dots grown with As4 and As2 sources using molecular beam epitaxy, J. Cryst. Growth. 301–302 (2007) 801–804. doi:10.1016/j.jcrysgro.2006.11.081.

[29] A. Avery, H. Dobbs, D. Holmes, B. Joyce, D. Vvedensky, Nucleation and Growth of Islands on GaAs Surfaces, Phys. Rev. Lett. 79 (1997) 3938–3941. doi:10.1103/PhysRevLett.79.3938.

[30] P.J. Simmonds, M.L. Lee, Tensile strained island growth at step-edges on GaAs(110), Appl. Phys. Lett. 97 (2010) 153101. doi:10.1063/1.3498676.

[31] V. Shchukin, E. Scholl, P. Kratzer, Thermodynamics and kinetics of quantum dot growth, in: D. Bimberg (Ed.), Semicond. Nanostructures, Springer, Berlin Heidelberg New York, 2008: pp. 1–39. http://link.springer.com/chapter/10.1007/978-3-540-77899-8_1.

[32] M. Meixner, R. Kunert, E. Scholl, Control of strain-mediated growth kinetics of self-assembled semiconductor quantum dots ¨, Phys. Rev. B. 67 (2003) 1–12. doi:10.1103/PhysRevB.67.195301.

[33] C. Lobo, R. Leon, InGaAs island shapes and adatom migration behavior on (100), (110), (111), and (311) GaAs surfaces, J. Appl. Phys. 83 (1998) 4168–4172. doi:10.1063/1.367170.

[34] T. Ogura, T. Nishinaga, Efficiency difference in Ga adatom incorporation in MBE growth of GaAs with As2 and As4 molecular beams, J. Cryst. Growth. 211 (2000) 416–420. doi:10.1016/S0022-0248(99)00804-0.

[35] E.S. Tok, J.H. Neave, J. Zhang, B.A. Joyce, T.S. Jones, Arsenic incorporation kinetics in GaAs(001) homoepitaxy revisited, Surf. Sci. 374 (1997) 397–405. doi:10.1016/S0039-6028(97)01241-7.

[36] M.R. Fahy, K. Sato, B.A. Joyce, Reflection high-energy electron diffraction intensity oscillations during the growth by molecular beam epitaxy of GaAs (111)A, Appl. Phys. Lett. 64 (1993) 190–192. doi:10.1063/1.111528.

[37] N. Moll, A. Kley, E. Pehlke, M. Scheffler, GaAs equilibrium crystal shape from first principles, Phys. Rev. B. 54 (1996) 8844–8855. doi:10.1103/PhysRevB.54.8844.

[38] J.A. Venables, G.D.T. Spiller, M. Hanbucken, Nucleation and growth of thin films, Reports Prog. Phys. 47 (1984) 399. doi:10.1007/978-1-4684-4343-1_16.

[39] D.J. Eaglesham, M. Cerullo, Dislocation-free Stranski-Krastanow growth of Ge on Si (100), Phys. Rev. Lett. 64 (1990) 1943–1946. doi:10.1103/PhysRevLett.64.1943.

[40] M. Ohring, The Materials Science of Thin Films, Academic Press, Hoboken, New Jersey, 1992.

[41] C.F. Schuck, S.K. Roy, T. Garrett, Q. Yuan, Y. Wang, C.I. Cabrera, K.A. Grossklaus, T.E. Vandervelde, B. Liang, P.J. Simmonds, Anomalous Stranski-Krastanov growth of (111)-oriented quantum dots with tunable wetting layer thickness, Submiss. (2019).

[42] J.R. Arthur, Molecular Beam Epitaxy, Surf. Sci. 500 (2002) 189–217. doi:10.3131/jvsj.16.91.

[43] I.O. Akhundov, D.M. Kazantsev, A.S. Kozhuhov, V.L. Alperovich, Optimization of conditions for thermal smoothing GaAs surfaces, in: J. Phys. Conf. Ser., 2018. doi:10.1088/1742-6596/993/1/012010.

[44] R. Singh, G. Bester, Nanowire quantum dots as an ideal source of entangled photon pairs, Phys. Rev. Lett. 103 (2009) 1–4. doi:10.1103/PhysRevLett.103.063601.

[45] A. Dousse, J. Suffczyński, A. Beveratos, O. Krebs, A. Lemaître, I. Sagnes, J. Bloch, P. Voisin, P. Senellart, Ultrabright source of entangled photon pairs, Nature. 466 (2010) 217–220. doi:10.1038/nature09148.

[46] J. Treu, C. Schneider, A. Huggenberger, T. Braun, S. Reitzenstein, S. Ho, Substrate orientation dependent fine structure splitting of symmetric In(Ga)As/GaAs quantum dots, Appl. Phys. Lett. 101 (2012) 022102. doi:10.1063/1.4733664.

[47] R. Seguin, A. Schliwa, S. Rodt, K. Pötschke, U.W. Pohl, D. Bimberg, Quantum-dot size dependence of exciton fine-structure splitting, Phys. E. 32 (2006) 101–103. doi:10.1016/j.physe.2005.12.019.

[48] K. Jacobi, Atomic structure of InAs quantum dots on GaAs (review), Prog. Surf. Sci. 71 (2003) 185–215. doi:10.1016/S0079-6816(03)00007-8.

[49] M. Jo, T. Mano, M. Abbarchi, T. Kuroda, Y. Sakuma, K. Sakoda, Self-limiting growth of hexagonal and triangular quantum dots on (111)A, Cryst. Growth Des. 12 (2012) 1411–1415. doi:10.1021/cg201513m.

[50] T. Michely, M. Hohage, M. Bott, G. Comsa, Inversion of Growth Speed Anisotropy in Two Dimensions, Phys. Rev. B. 70 (1993) 3943–3946. doi:10.1103/PhysRevLett.70.3943.

[51] N. Moll, A. Kely, E. Pehlke, M. Scheffler, GaAs equilibrium crystal shape from first principles, Phys. Rev. B. 54 (1996) 8844–8855. doi:10.1103/PhysRevB.54.8844.

CHAPTER FIVE: OPTIMIZED TSQD RESULTS AND FUTURE WORK

5.1 TSQD Tuning and Optimization for Future Entangled Photon Emission

The optimization of GaAs(111)A TSQDs for entangled photon emission involves several considerations. Epitaxial growth provides high crystal quality and straightforward device integration (Section 1.2.1). The QD structure provides a good system for maintaining coherence (Section 1.2.6). The (111)-surface provides the high symmetry that is essential for a low FSS between bright exciton states needed to produce entangled photon emission (which is further reduced by the TSQD low aspect ratio) (Section 1.2.6). Tensile strain provides a means to lower band gap in pursuit of IR emission wavelengths (Section 1.2.7). Beyond these various factors, optimizing TSQDs for entangled photon emission must also include QD structural and optical quality, constraints for detecting emission from single QDs, and future device specifications.

The optimization results presented below comes from an expansion of the work presented in Chapter 1. These additional growths began with a series exploring the effects of depositing GaAs over a wider range of thicknesses (1.5ML – 7 ML) at 535 ºC, a series of 3.5 ML TSQDs grown from 470 ºC – 580 ºC, and a series of 4.5 ML TSQD samples grown from 505 ºC – 535 ºC (growth rate and V/III fixed at 0.075 ML/sec and 75 As_4/Ga respectively). Using the characterization data from these growths, I developed a qualitative rulebook outlining the processing-structure-properties-performance (sp^3) of GaAs(111)A TSQDs (***Figure 5.1***) (quantitative data is available, but result will vary with different growth chamber layouts, effusion cells, and amount of source material).

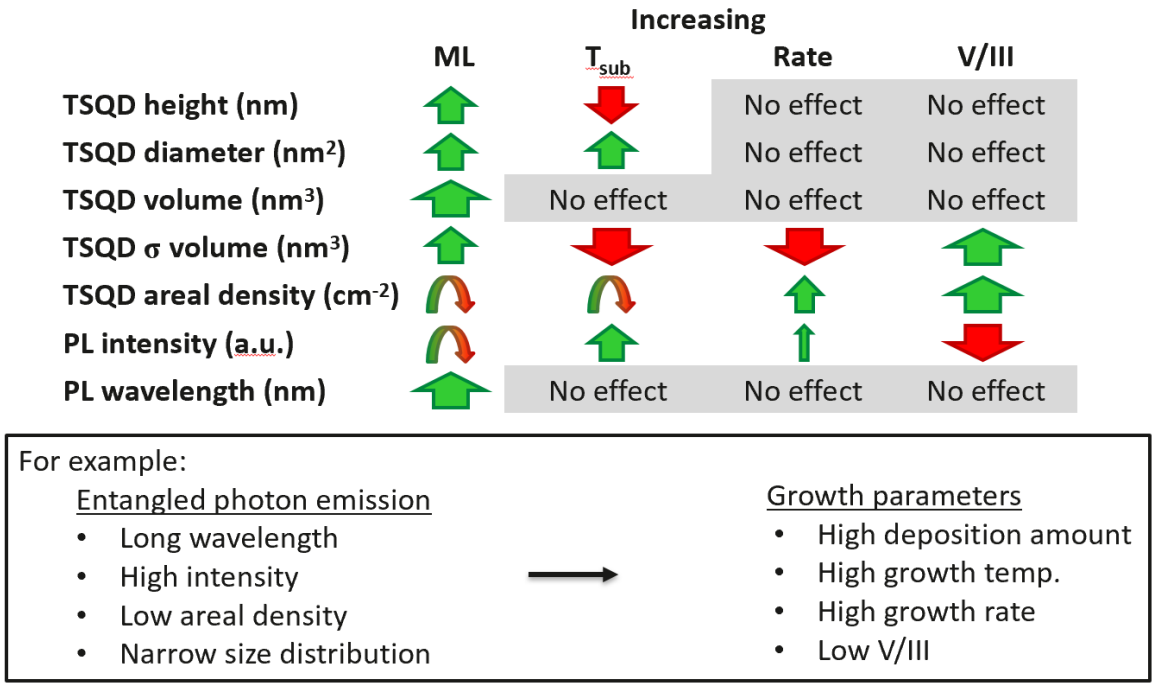

Figure 5.1: A qualitative rulebook for tuning and optimization of GaAs(111)A TSQDs. The TSQD structural and optical properties on the left can be varied by the growth parameters along the top. The arrows indicated the direction and strength of the event. For example, increasing ML deposition moderately increases TSQD height, greatly increases TSQD volume, and first increases then with continued deposition decreases TSQD areal density. In the box this rulebook, important characteristics for entangled photon emission and detection, and therefore the preferential growth parameter phase-spaces.

Three of these new growths were also repeated using As_2 instead of As_4, which informed my decision to use As_2 in all successive growths (Chapter 4). Finally, I employed a design-of-experiments matrix to determine the best growth rate and V/III (deposition amount and substrate temperature fixed at 3.5 ML and 570 ºC). Collectively, these additional growths filled out the remaining growth-parameter phase-space of GaAs(111)A TSQDs. I achieved a considerable range of GaAs(111)A TSQD tunablity:

- QD height (average): 0.39 nm – 1.33 nm
- QD diameter (average): 22.3 nm – 89.7 nm
- QD volume (average): 45 nm^3 – 1270 nm^3
- QD areal density: 1.0 x 10^8 to 1.4 x 10^9 cm^{-2}

- QD emission wavelength: 958 nm – 1116 nm
- WL emission wavelength: 888 nm – 1027 nm

Furthermore, we achieved a three-fold improvement in emission intensity and five-fold improvement in emission efficiency compared to our initial TSQD growths. Most of these additional growths exhibited room-temperature emission, a hallmark of good crystal quality.

The optimized growth parameters for future entangled photon emission are:

- Deposition amount: 4.5 ML for longer wavelength emission approaching the IR; 3.0 ML for micro-PL analysis of single QD emission (due to a 1000 nm cutoff of the available detector).
- Substrate temperature: 560 ºC for highest emission efficiency and narrow FWHM (570 ºC has similar quality, though wider FWHM).
- Growth rate: 0.175 ML/sec for highest emission efficiency and lowest areal density (low areal density is necessary for isolation of single QDs for micro-PL analysis) (0.125 ML/sec has similar quality, though higher areal density).
- V/III: 75 As_2/Ga for highest emission efficiency and improved structural symmetry.

5.2 Future Work

The next steps in this research are to

1) demonstrate single photon emission and low FSS in our optimized TSQDs;
2) use photon pair correlation and maximally entangled state fidelity to verify entangled photon emission;
3) design the material structure which will allow integration of TSQDs into a

device (a p-i-n doped structure in an optical cavity with a high-reflectivity Bragg mirror); and

4) build an on-demand electrically-triggered prototype TSQD LED as in ***Figure 1.1***.

Steps 1 and 2 are already underway on my optimized GaAs(111)A TSQDs.

Based on this work, the many promising device applications of (111)-oriented TSQDs, including robust and easily integrated entangled photon LED materials made in a single processing step, may soon be realized.